Karlsruher Institut für Technologie

Physikalisches Institut

Fakultät für Physik

Karlsruher Institut für Technologie

Spatially Resolved Investigation of NbN Superconducting Single Photon Detectors

Räumlich Aufgelöste Untersuchung Supraleitender NbN Einzelphotonendetektoren

Diplomarbeit

von

Philipp Jung

9. August 2010

Referent: **Prof. Dr. A.V. Ustinov**
Korreferent: Prof. Dr. M. Siegel

Contents

1. Introduction **1**

2. Fundamentals **3**
2.1. The superconducting nanowire single photon detector . . . 3
2.1.1. Why bother? . . . 3
2.1.2. Layout of the device . . . 4
2.1.3. The detection of a photon . . . 6
2.1.4. Dark counts . . . 10
2.1.5. More model improvements . . . 12
2.1.6. Electrothermal response . . . 13
2.1.7. The detection efficiency . . . 16
2.2. The laser scanning microscope . . . 17
2.2.1. Understanding the spatial resolution . . . 17
2.2.2. The point spread function . . . 19
2.2.3. Two operating regimes . . . 22

3. The experiment **27**
3.1. Idea and goal of the experiment . . . 27
3.2. Optics . . . 28
3.3. Cryogenics . . . 30
3.4. Electronics . . . 33
3.5. Software . . . 36
3.6. Technion equipment . . . 37

4. Results and conclusions **41**
4.1. Meander structures . . . 41
4.2. Long bridge structures . . . 50
4.3. Short constrictions . . . 51
4.4. The experiment at Technion . . . 53
4.5. Outlook . . . 57

A. Appendix **59**
A.1. Development of a fast pulse counter . . . 59
A.1.1. Requirements and feasibility . . . 59
A.1.2. Choice of hardware . . . 60
A.1.3. Design and road map . . . 61
A.1.4. Development stages . . . 63

A.1.5. Conclusion 65
A.2. Development of a scanning microscopy application 66
A.2.1. Requirements 66
A.2.2. Design and concept 67
A.2.3. Implementation 69

Summary **71**

Zusammenfassung **72**

Acknowledgements **75**

Bibliography **77**

1. Introduction

Around the end of the 19th century the concept of the particle nature of light finally gained some physical ground when Heinrich Hertz found the dependence of the energy of light on its wavelength rather than on its intensity during studies of the photoelectric effect. This concept, although in principle existent since the days of the ancient Greek philosophers, stood in sharp contrast to the predominant idea of light as a wave at that time. The resulting wave-particle duality, the development of quantum mechanics and the standard model of particle physics marked the onset of a new age not only in physics. This newly gained perspective gave rise to an enormous variety of inventions (of which optical communication is but one of many), which radically shaped our society throughout the 20th century and is continuing to do so today. Lately this process, fueled by the need for ever smaller and faster devices and means of communication, spawned a whole new scientific and industrial branch: What is commonly called "Nano-Technology" covers a wide spectrum of new applications founded on the knowledge acquired throughout the last century.

I am going to present and investigate one of these nano-electronic devices, the so-called *"Superconducting nanowire single photon detector" (SNSPD)*. Its benefits are almost self-explanatory: If one uses light as a means of communication as in telecommunication, imaging as in microscopy or simply photography or quantum-cryptography, the most obvious task to do is to develop a device which is able to detect the smallest possible quantity of light, a photon, with the highest possible temporal and spatial resolution and the lowest noise. Single photon detectors have already been realized on a semiconductor basis and with photomultiplier tubes but, as we will see later, these do not fulfill all the criteria to a satisfying degree.

As the name suggests, these detectors rely on superconductivity which itself was only discovered in the early twentieth century. The main principle of operation is to bring a structured superconducting thin-film so close to the phase transition from superconductivity to normal conductivity by biasing it with a current that even a disturbance with an energy as low as that of a single photon can trigger a local phase transition. As all processes involved in this detection are quite fast compared to other devices, these detectors are very promising especially in fields where fast count-rates are needed.

Superconducting devices in general have one obvious disadvantage which greatly limits their usability in many potential fields of application: They have to operate below their superconducting critical temperature and with the materials presently used to fabricate most superconducting nanoelectronical devices, temperatures below that of liquid N_2 are needed. While for current devices this means that their application is limited to scientific environments, future high-T_c materials and advanced electrical cooling techniques could make superconducting nanoelectronics interesting for broad commercial applications.

Most of the research that has already been conducted on superconducting single photon detectors describes their performance without focusing on the influence of their spatial properties on the overall performance. This, however, is a key to optimizing their yield since geometrical features and spatial inhomogeneities play an important role in the detection process. To complete the picture we have of them, my work was to map parameters like detection efficiency to the location of single incident photons.

The way we chose to tackle this task was to use a *"Laser Scanning Microscope (LSM)"*. This device has been used in many experiments involving light-induced resistive changes in various superconducting samples. For this experiment the setup had to be modified in order to map photon counts to the position of a laser beam.

To clarify some of the less evident aspects involved in this experiment, chapter two describes the fundamentals needed to understand the photon detection and the scanning process. Chapter three focuses on the experimental setup that was used to make the measurements. The results and conclusions of this work will then be presented in chapter four. Apart from the experimental setup and actual measurements, some of the time I spent on this task went into programming a suitable software and building a fast pulse counter. I will elaborate on those two subjects in the appendix.

2. Fundamentals

In this chapter I am going to introduce the reader to some fundamentals necessary to understand my experiment. This includes a description of the samples used as well as the principle of operation of the Laser Scanning Microscope.

2.1. The superconducting nanowire single photon detector

As the name suggests, the *Superconducting Nanowire Single Photon Detector (SNSPD)* is a nanoelectronical device designed to detect single photons. How exactly this is achieved and why we think that this is a promising device will be explained in this section.

2.1.1. Why bother?

As already mentioned in the introduction, single photon detectors already exist and have been on the market for some time. So why bother with a new development that needs low temperatures to operate when we already have access to technologies that work at room temperature? To understand this I will now introduce some key properties by which the performance of these devices is commonly judged. To keep this as general as possible I will use the terms *incoming event* for the kind of input we want the detector to trigger on[1] (i.e. in our case a photon from a laser source) and *count event* as the output of the detector that tells us that an input event has occurred (i.e. a voltage pulse).

- **Dead time or reset time** τ_r is the time from one incoming event which the detector takes to return to its initial state and be ready for the next incoming event.
- **Timing** is the internal delay between an incoming and a count event.
- **Detection efficiency (DE)** of a detector is the probability that it triggers on an incoming event and produces a count event.
- **Maximum count rate** is the highest number of count events per time a detector can produce. It is usually reached when the average time between two incoming events multiplied by the detection efficiency becomes comparable to the dead time.
- **Dark count rate** refers to the count rate of a detector without any input events.

[1] In contrast to other "triggering" events that are unwanted. See 2.1.4.

Most of these key properties are not only determined by the device itself but also by the chosen work-point. In case of the SNSPD one example for this is the bias current. Decreasing it further below the critical current will minimize the dark count rate, but it will also decrease the detection efficiency. The same is true for temperature work-point: While lowering the operating temperature will significantly reduce dark counts, the effort and cost connected to such conditions make it less attractive for most applications. This underlines that there is usually no perfect work-point for these detectors; it highly depends on the type of application they are being used in.

From Table 2.1 one can see, that especially in fields of application where high maximum count rates are needed the SNSPD shows some promise.

Name of device	DE	Dark count rate $[\frac{1}{s}]$	Max. count rate $[\frac{1}{s}]$
Avalanche Photo-diodes[2]	65%	1500	$25 \cdot 10^6$
Photomultiplier tubes[3]	10%	< 300	$25 \cdot 10^6$
SNSPD (without cavity)[4][27]	$< 2.5\%$	$< 10^5$	$70 \cdot 10^6$

Table 2.1.: Comparison of some SPD devices based on different technologies.

[2] Perkin Elmer SPCM-AQRH-10
[3] Hamamatsu R6358-10
[4] Typical performance data in optical ^{4}He cryostats. Optical cavities will significantly improve the detection efficiency. See for example [18]

2.1.2. Layout of the device

At first glance, the SNSPD is a very simple device, as it is nothing more than a narrow strip of a thin-film superconductor on some substrate. Since my work has been on NbN samples on sapphire substrate I will focus on these materials, although other combinations exist and work. The NbN film thickness is usually a few nanometers, the width close to 100nm while the length of the strip depends on the desired size of the detector. To cover a certain area most of the detectors are not just one straight strip, but a meander which usually covers a square area whose sides are a few microns long as can be seen in Fig. 2.1 and Fig. 2.2. As we will see later in this section, the geometry of the strip is the key to its ability to detect photons. As the thickness of the film is less than the coherence length of the superconducting wave function, the strip can, in terms of superconductivity, be regarded as a 2D object.

Before we go too far into the details of the detection we should note some geometrical features, which have a profound impact on the performance of the detectors. First of all, the small thickness of the film means that it is almost transparent. Calculations [24] have shown that the absorption probability of typical films is limited to a few percent. This immediately explains the poor DE compared to its competitors in table 2.1 and the need for optical cavities as a compensation. A second noteworthy fact is the meander geometry being used: the parallel lines imply that the detector will have a strong polarization-dependence, as the electrical field of light couples more strongly when oriented parallel to the lines. Light polarized perpendicularly to the meander lines will thus be detected with a lower efficiency [16].

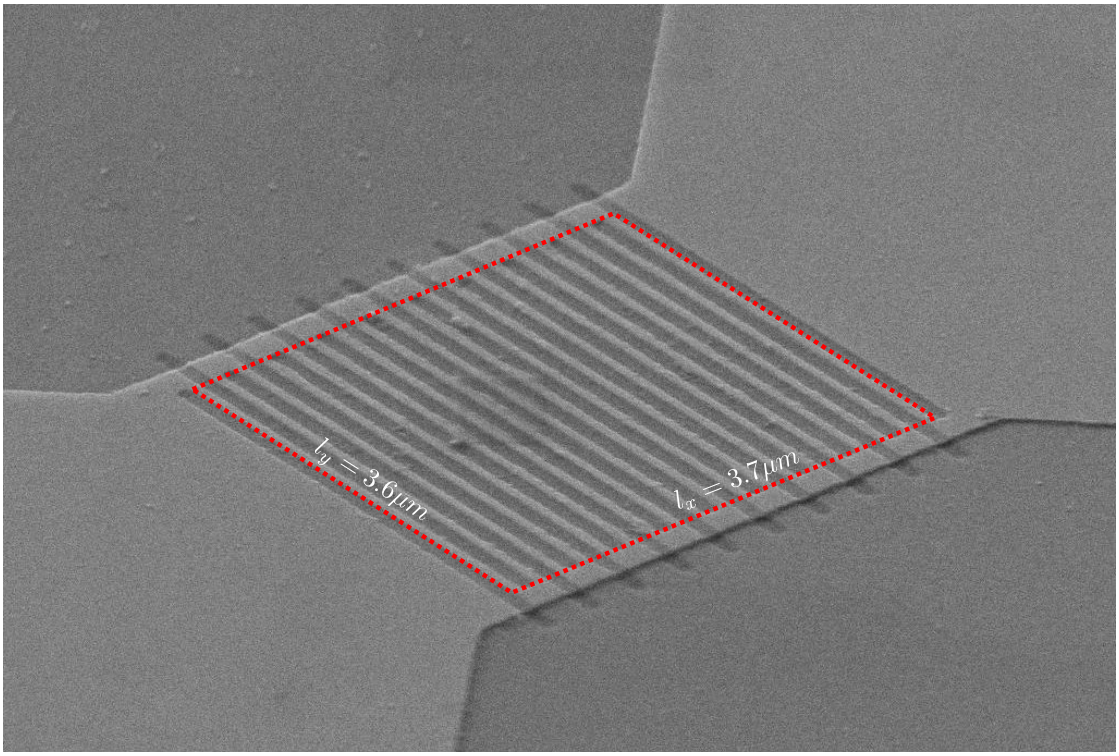

Figure 2.1.: *Scanning Electron Microscope (SEM)* image of a detector. The highlighted region is what we expect to be the active area for photon detection. The image was supplied by K. Ilin from the *Institut für Mikro- und Nanoelektronische Systeme*

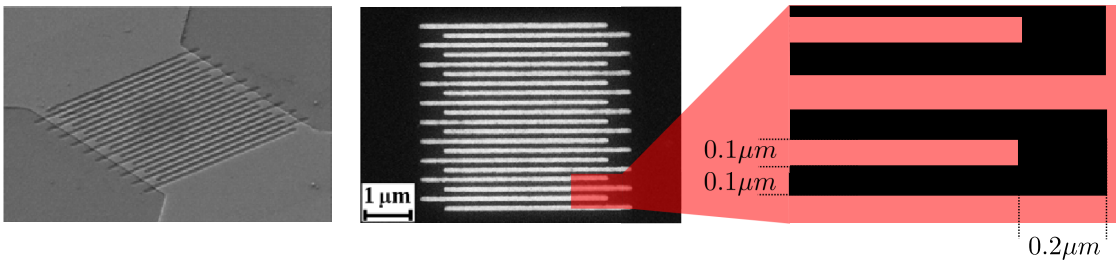

Figure 2.2.: From left to right: SEM image of a detector. *Transmission Electron Microscope (TEM)* image of the meander pattern. Sketch of a section of the meander to show dimensions. The first two pictures were taken from [24]

2.1.3. The detection of a photon

To operate the device it has to be cooled down below its superconducting transition temperature $T < T_c$ (typically $10K < T_c < 15K$ for NbN films). Due to the finite number of Cooper pairs in this state the strip will then be able to carry a maximum supercurrent of $I_c(T)$ and is current-biased at I_b somewhere below but close to this critical current, typically in the range $0.75 \cdot I_c < I_b < 0.95 \cdot I_c$.

A simplified picture

The simplest approach one can use to explain the reaction of such a system to an incident photon is commonly referred to as the *Hot-Spot Model* [22]. The argumentation works as follows:

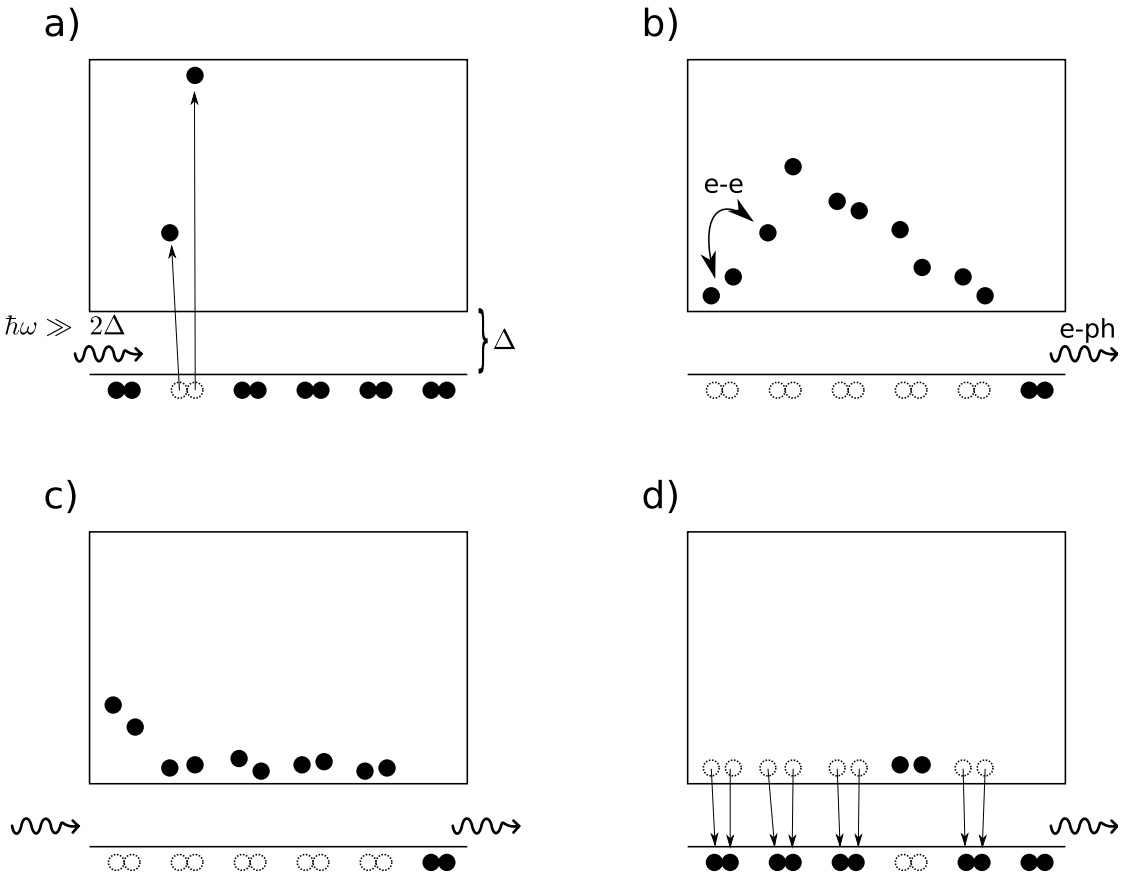

Figure 2.3.: The Hot-Spot model I: a) A single photon breaks a cooper pair and creates a highly excited quasiparticle b) Electron-electron and electron-phonon processes cascade and create more quasiparticles c) The excitations relax down to the level of the energy gap d) Quasiparticles recombine into Cooper-pairs and phonons escape to the substrate

1. Initially the bias current $I_b < I_c$ is distributed evenly over the cross-section of the strip and the number of cooper pairs for this temperature is in equilibrium (Fig. 2.4a).

2. A photon of the energy $E_p = \hbar\omega$ breaks a single Cooper pair and creates two high energy excitations with an energy several orders of magnitude higher than the superconducting energy gap (Fig. 2.3a & 2.4b).

3. In an avalanche of electron-electron as well as electron-phonon processes this initial excitation transfers its energy, thereby creating a large number of secondary quasi-particles with an energy just above the gap. If the initial photon energy is high enough this process will effectively destroy superconductivity in a small volume around the incident spot. As this implies a change in the wave-function, the diameter of this initial hot-spot has to have a diameter D at least of the order of $D = 2 \cdot \xi$ (Fig. 2.3b & c).

4. Since the width of the bridge is larger than the hot-spot, the bias current which is still flowing will be redirected to bypass the hot-spot thereby increasing the current density in this particular cross-section.

5. If this current density to the sides of the hot-spot then exceeds the critical current density of the bridge at that temperature, the whole cross-section will become normal. (Fig. 2.4c & d) The voltage associated with this normal region will trigger another process which will be described in 2.1.6 and essentially leads to a rapid expansion of the normal domain and a decrease of the current running through the bridge.

6. Once the current is lower than a certain return current I_r or if the number of broken Cooper-pairs were insufficient to create a hot-spot and make a whole cross-section normal, the Cooper-pairs will recombine and the normal domain will disappear (Fig. 2.3d).

Some refinement

Although the aforementioned picture provides a very simple and comprehensive approach to understanding the detection mechanism, which is most probably not entirely wrong, there is a more elegant way to address the question. This refined model [5] also enables us to get a quantitative grip on the problem where the simple model could only provide a qualitative explanation and it solves some problems associated with the minimum size of a hot-spot. So let us look at the situation of the current-biased nanobridge again: Let us define $n_s(T)$ as the cooper-pair density and $j_b(I_b)$ the bias current density in the sample. Assuming that the bias current is completely carried by the cooper pairs, we can define a current-dependent average cooper-pair velocity v_s :

$$j_b(I_b) = \frac{I_b}{w \cdot h} = 2 \cdot e \cdot n_s(T) \cdot v_s$$

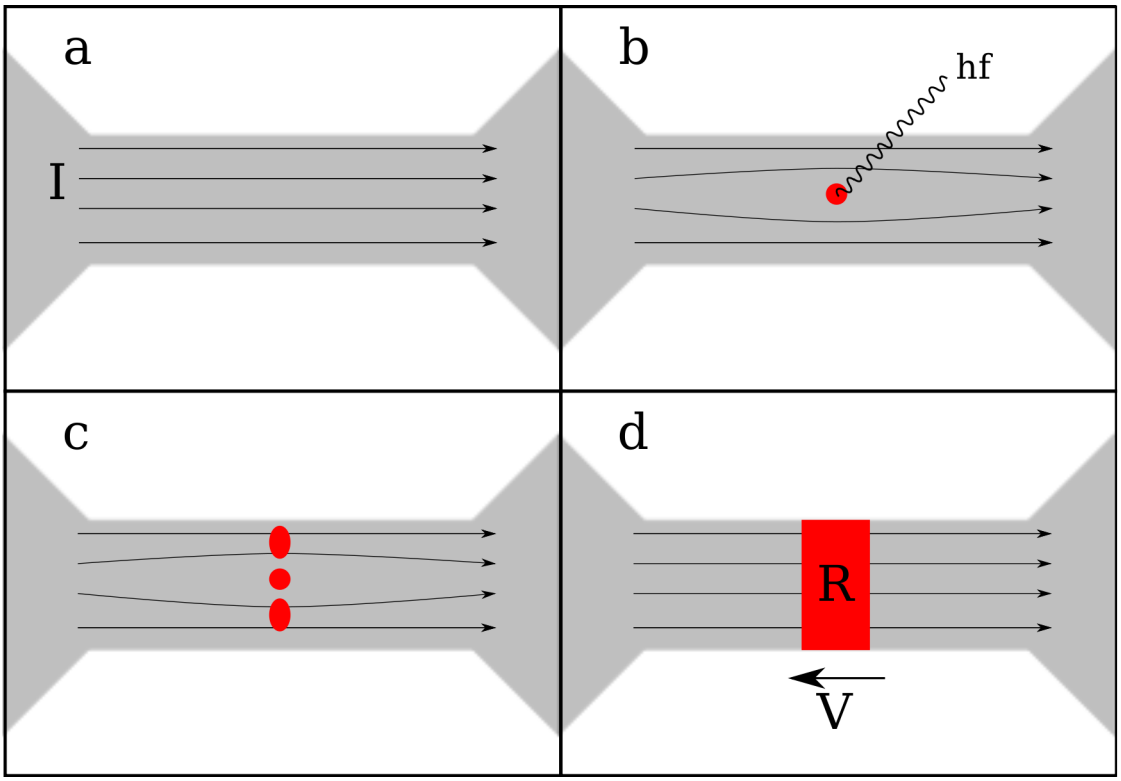

Figure 2.4.: The Hot-Spot model II: a) Bias current flowing homogeneously through the bridge b) A photon creates a small hot-spot forcing the bias to flow around it c) Bias current exceeds critical current to the sides of the hot-spot d) A normal region forms across the bridge

$$v_s(I_b, T) = \frac{I_b}{2 \cdot w \cdot h \cdot e \cdot n_s(T)}$$

Where w is the width and h the height of the bridge. This also automatically defines a critical velocity of $v_c(T) = v_s(I_c, T)$ which can be understood as the maximum velocity at which a coherent supercurrent can be maintained. We now put our focus on the small volume enclosing the cross-section, commonly known as the ξ-slab[2] with the volume of $V_\xi = w \cdot h \cdot \xi$, in which the photon is to be absorbed. This volume is highly relevant to our analysis because it is the smallest candidate for a normal cross-section that can exist without just being tunelled through by the Cooper-pairs. Following the first steps of the standard hot-spot model, an incident photon will break a number of cooper pairs[3]

[2]From here on ξ will be used as the Ginzburg-Landau coherence length.

[3]In general, a photon will not use all its energy to break Cooper-pairs. I will therefore use $E_p \leq \hbar\omega$ for the energy used to break pairs.

so that the new cooper pair density

$$n_s'(T, E_p) = n_s(T) - \frac{E_p}{2\Delta(T)}$$

in the slab is lower than the equilibrium value of n_s. This leaves the bias current which passes through this volume to be carried by the remaining Cooper pairs thereby increasing their mean velocity to $v_s'(I_b, T, E_p)$. If now

$$v_s'(I_b, T, E_p) = \frac{I_b}{2 \cdot w \cdot h \cdot e \cdot n_s'(T, E_p)} > v_c(T) = v_s(I_c, T), \tag{2.1}$$

the mean Cooper pair velocity would have to exceed its critical value in order to maintain the supercurrent which, of course, it cannot. One can also put this into a more intuitive form by defining the number of cooper pairs $\delta N^*(I_b, T)$ that need to be broken in order to fulfill equation 2.1:

$$\delta N^*(I_b, T) = n_s(T) V_\xi \left(1 - \frac{I_b}{I_c}\right). \tag{2.2}$$

As the energy required to break a single Cooper-pair is $2\Delta(T)$ we can define a critical photon energy

$$E_c(I_b, T) = \delta N^*(I_b, T) \cdot 2\Delta(T) = 2n_s(T)\Delta(T)V_\xi \left(1 - \frac{I_b}{I_c}\right), \tag{2.3}$$

which is required to break enough pairs for detection. Here we arrive at the same qualitative conclusion as with the simpler model: Once the criterion

$$\hbar\omega \geq E_p \geq E_c(I_b, T) = 2n_s(T)\Delta(T)V_\xi \left(1 - \frac{I_b}{I_c}\right) \tag{2.4}$$

is met, a cross-section of the sample will no longer be able to maintain superconductivity. Note, however, that the refined approach does not require a real hot-spot to exist for this result. This fact has some direct consequences for the detection, one of which is that by tuning the bias current close enough to the critical current one could make this detector sensitive to extremely low energy photons albeit at the same time making it more sensitive to fluctuations.

Limitations of this model

One of the features of these models is a cutoff in the detection efficiency. If the energy of the incoming photon is not sufficient to break enough Cooper pairs to satisfy Eq.2.4, the detector will (in the absence of fluctuations) stay superconducting and will not generate any measurable response. This can either be formulated as a current- or spectral cutoff as the criterion for detection (eq. 2.4) contains both these variables. The implication of this is simple: if the photon energy is smaller than the critical energy, the detection efficiency should drop dramatically. Although a cut-off can indeed be seen experimentally it is

much less pronounced than the model suggests as the DE only drops rather slowly [23]. Geometrical variations in the strip and the fact that $E_p \leq \hbar\omega$ can give some explanation why the DE decreases even above the cutoff. But so far we have no explanation why we still see noteworthy count rates below the cutoff.

I will now address the matter of dark counts before I pick up this subject again in section 2.1.5 in the hope that this will provide a better understanding of the matter.

2.1.4. Dark counts

It is a well-known dilemma for most sensitive detectors that they are supposed to react only on particular, low energetic events when slight changes in the operation conditions (i.e. temperature, current) can cause changes of the same scale. In our case, where the detector output is quantifiable in time, unwanted trigger events lead to a kind of shot noise commonly called *dark counts*. In this subsection I will briefly name and discuss the most important sources of those events.

Photons from undesirable sources

Perhaps the most obvious (although usually not the most important) source of unwanted count events for a photon counter are unwanted photons. In experiments like ours, one usually uses a light source with a well-defined output power or even a single photon source. Then the number of output pulses is compared to the expected number of photons originating from the source over a certain time span. In reality though, there are two additional photon sources present in most experimental setups: One of those are stray photons from ambient light (i.e. daylight). In a completely closed setup this can easily be minimized to a negligible degree, whereas in open setups like ours, there are a number of places where ambient light can couple into the system and reach the detector. In this case the problem can only be addressed by vigorous optical shielding. The other source of unwanted photons is the surrounding of the detector which, having a non-zero temperature, will emit photons according to the black-body radiation law. In our case most of the surfaces facing the detector have a temperature of about 70K[4] with the exception of the optical window which faces room-temperature components outside the cryostat. Approximations for the contribution of those photons to the overall dark count rate have been carried out in [5]. The authors come to the conclusion that, in their setup, this contribution is negligible compared to other sources. From results in our setup, however, we have reason to believe that this contribution is clearly visible (see Fig. 4.6).

Operation conditions

Another category of sources of possible dark counts are changes in the operation conditions. A typical but hard to exclude example of this is current noise. Especially when the SNSPD is biased close to its critical current, a slight variation in the bias current can

[4] An explanation for this can be found in Sec. 3.3

trigger a pulse directly or relax the detection criterion far enough for one of the other dark count sources to bring about the same effect. Using low-pass-filters and current dividers together with low-noise battery-powered current sources is a way to minimize current noise. One of the causes of after-pulsing[5] (which can be seen as a form of dark counts) can, at least partly, be explained by variation in the temperature caused by the energy dissipation associated with a pulse. If the effective cooling power is too low to transport all the heat away from the sample before the bias current is redistributed through it (see 2.1.6 for the explanation of this current redistribution), an after-pulse will be triggered once the current through the sample exceeds its (lowered) critical current.

Fluctuations of the order parameter

Just as external influences can change the number of Cooper pairs, there is also always a temperature-dependent fluctuation of the order parameter, the energy gap. There is a probability that within a certain volume of the sample the energy of the fluctuation exceeds the critical energy necessary for a normal cross-section to appear. Calculations in [5] have shown that the contribution of fluctuations to the total dark count rate is especially high for I_b very close to I_c.

Vortex entry and Vortex- Antivortex-depairing

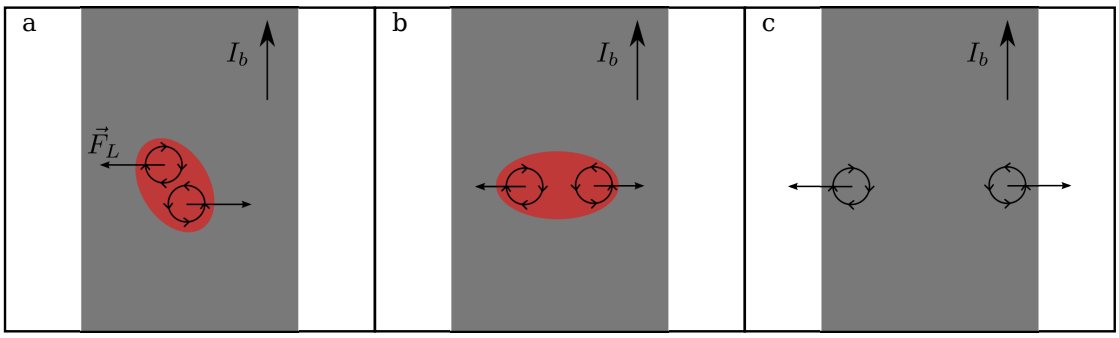

Figure 2.5.: *Vortex-Antivortex-Pairs (VAP)*: The gray area is one section of the bridge in which one VAP in their common pair-potential (red) exists. $\vec{F}_L$ Vectors show the direction of the Lorentz force. a) The current exerts a torque on unoriented VAPs b) When oriented, VAPs move away from their equilibrium distance thereby decreasing their binding energy c) Binding is broken (directly or thermally) and vortices travel in opposite directions.

It seems that one major contribution to the dark count rate (as well as to the detection rate of photons with sub-critical energy) could result from the movement of magnetic

[5] A phenomenon sometimes observed in these detectors depending on the experimental setup where several pulses are emitted shortly after an initial pulse

vortices inside the strip. Different authors [3, 10, 12] have evaluated possibilities of magnetic vortices overcoming the edge barrier of the film by thermal activation or of the depairing of so-called *Vortex-Antivortex-Pairs (VAP)*. According to [14], Abrikosov-vortices can exist in a strip with the given dimensions and are paired in VAPs which are present in two-dimensional superconductors below the transition temperature at zero magnetic field (See. [6] p.325). Since they are paired, they do not carry any net flux. In this bound state the Lorentz force does not exert any translational force on the pair which is why they do not move and why there is no dissipation in the bound state. They will, however, be aligned perpendicularly to the current, their energetically most favorable state (see figure 2.5). In this situation, thermal activation can lead to the depairing of the vortices. Each of them will then travel to the side of the strip separately which causes energy dissipation and thus local heating, which in turn may drive the superconducting region into the normal state.

Comparisons in [3] were not able to decide wether the single vortices overcoming the barrier or depairing of VAPs were the more probable mechanism because their quantitative temperature and current dependences are very similar and both seem to fit the data. For reasons of simplicity I will from now on refer to the VAP scenario rather than to single vortices. Most of the arguments I am going to give apply for both theories.

2.1.5. More model improvements

I will now come back to the question we left unanswered in 2.1.3: Why are count rates for sub-cutoff photons seen experimentally although the model predicts a rather sharp cutoff? The answer lies in the last section, as we have to take into account all processes mentioned there. There are several possible scenarios in which a photon with sub-critical energy can still be detected, all of which rely on the secondary processes that also cause dark counts. After the photon-absorption one section of the detector is out of equilibrium so that the effects causing dark counts are greatly enhanced. Imagine an "almost-critical" photon with the energy $\hbar\omega \geq E_p$ breaking almost enough Cooper pairs to make the ξ-slab normal. Any of the dark count sources could now provide the last push of $E_{\text{rest}} = E_c - E_p$ to tip the scale and make that ξ-slab normal.

Fluctuations of the order parameter A fluctuation of the energy gap $\Delta - \delta\Delta$. This makes a photon with $E_p < E_c$ countable if:

$$\delta\Delta \geq \Delta(T) - \frac{E_p}{2n_s(T)V_\xi\left(1 - \frac{I_b}{I_c(T)}\right)}. \tag{2.5}$$

VAP depairing Since the binding energy U of VAPs depends on the energy gap Δ as

$$U \propto \Delta\, tanh\left(\frac{\Delta}{2k_B T}\right), \tag{2.6}$$

the probability of VAP depairing is increased at the absorption site.

Current noise The introduction of a slight change in the bias current of δI in equation 2.4 would change it to

$$E_p \geq 2n_s(T)\Delta(T)V_\xi \left(1 - \frac{I_b + \delta I}{I_c}\right) \tag{2.7}$$

which means that even if $E_p < E_c$ the incoming photon will be counted if:

$$\delta I \geq I_c \left(1 - \frac{E_p}{2n_s(T)\Delta(T)V_\xi}\right) - I_b \tag{2.8}$$

Second photon A second photon (i.e. a thermal one from the surrounding walls) with an energy of $E \geq E_{\text{rest}}$ arriving in the same area during the avalanche process.

2.1.6. Electrothermal response

Up to this point of the analysis, we have explained why a small cross-section of the strip will change from the superconducting to the normal state when hit by a photon. Since all the processes involved work on a picosecond timescale, the model does not yet explain the existence of a pulse of several nanoseconds. Another unanswered question is: What happens to the normal domain? To answer these questions we will use an *electrothermal model* [28] which links the evolution of the normal domain to the electrical embedding of the sample.

Electrical equivalent

Let us start by defining an electrical equivalent model to describe our sample. The first thing we have to note here is that a sample of the given dimensions will have an inductance which is formally

$$L_{\text{sample}} = L_G + L_K \approx L_K$$

the sum of its geometric (L_G) and kinetic(L_K) inductance. Since we know from simulations, that L_K is about three orders of magnitude higher than L_G, we will ignore L_G from now on. We will assume the resistance of the sample to be zero in the superconducting state. When a normal domain appears due to the absorption of a photon, it will change to a finite value of

$$R(t) = R_s \frac{l_n(t)}{w}$$

where R_s is the *sheet-resistance* of the film, $l_n(t)$ the length of the normal zone, and w the width of the strip. Note that we assume the length of the normal domain to be time-dependent during the pulse generation, which is a key feature of the model that is to come. The external part of the system consists of a shunting resistor R_0 parallel to the sample, a bias-tee used to separate the dc-bias current from the RF-pulse, and a current source, which supplies the bias current, all of which can be seen in figure 2.6.

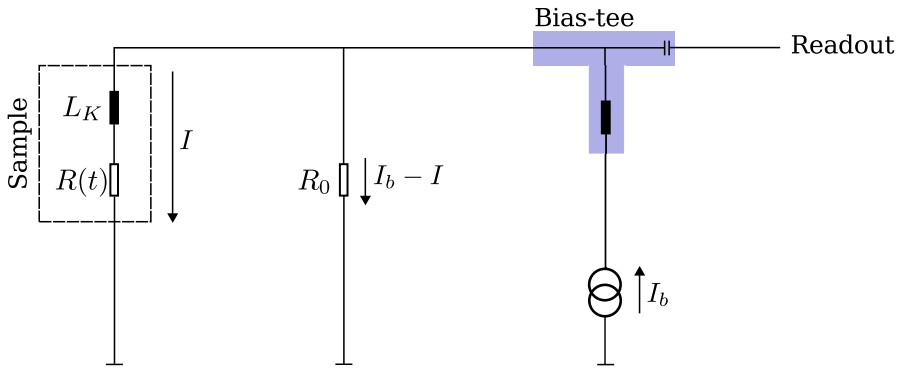

Figure 2.6.: Electrical equivalent of the sample.

In the general case, one part (we will simply call it I) of I_b will flow through the sample, while the rest $I_b - I$ will flow through the shunting resistor R_0. Using *Kirchhoff's loop law*[6] we can state that:

$$L_K \frac{d}{dt} I(t) + R(t)I(t) - R_0 \left(I_b - I(t)\right) = 0. \tag{2.9}$$

This differential equation describes the time-dependence of the current-distribution inside the circuit. From this information and the known shape of a pulse alone, one can estimate the approximate shape of $R(t)$ during the detection. A quick analysis of this shows that

$$R(t) = R_\xi \Theta(t - t_0)\Theta(t_0 + \tau - t)$$

($R_\xi = R_s \frac{\xi}{w}$ is the normal state resistance of the ξ-slab, τ the duration of the existence of the normal domain) does not solve the problem. To do so in the approximation of a pulse-like $R(t)$, the peak value of $R(t)$ would have to be much larger than R_ξ. This leads to the assumption that the final length of the normal domain in the bridge $l_{\max}$ must be much larger than ξ which is why we have to take a look at the behavior of the superconductor/normal-conductor domain walls in the presence of current induced heating.

Thermal behavior

We will now investigate behavior of the normal domain, which has a length $l_n \geq \xi$. Assuming that a current is being pushed through the sample, there will be *ohmic losses* depending on the length of the domain and the strength of the current:

$$P_{\text{loss}} = R_s \frac{l_n}{w} I^2.$$

[6] In a closed electrical circuit the directed sum of the potential differences has to be zero.

In [8] the authors explain this situation by a current-dependent velocity of the super-

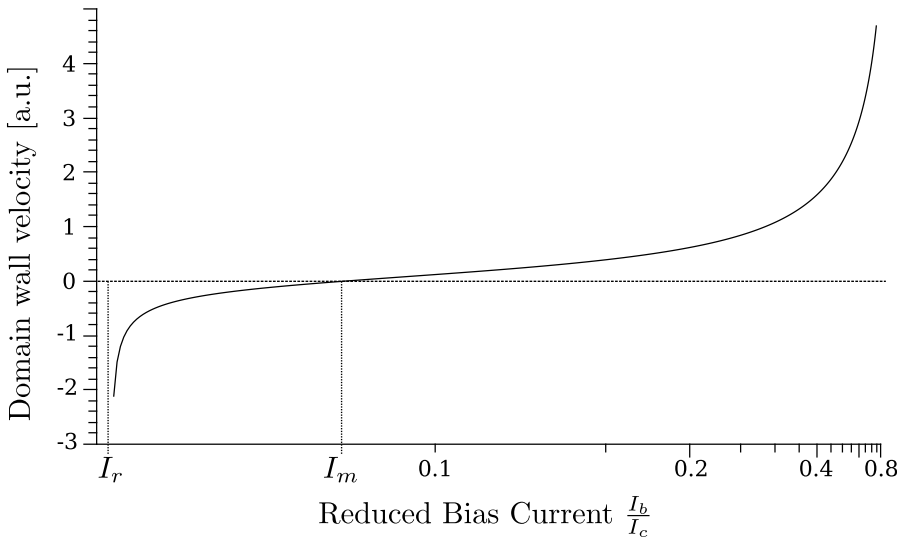

Figure 2.7.: Domain-wall velocity in dependence of reduced bias current.

conductor / normal-conductor domain walls $v_i(I)$. As shown in figure 2.7, there is a current I_m at which the domain walls are stable. For larger currents, the domain expands (positive $v_i(I)$) as an effect of the high local heating, while for smaller currents the domain shrinks (negative $v_i(I)$) as the heat at the edges of the domain is transported away more efficiently then generated. If the current reaches below I_r, the normal domain will collapse and become superconducting. Using the definition for the resistance of the normal domain:

$$R(l_n) = R_s \frac{l_n}{w} \tag{2.10}$$

and knowing that the domain wall velocity is nothing else but the time derivative of the domain length $v_i(I) = \frac{d}{dt} l_n$, we find the current dependent change of the resistance to be

$$\frac{dR}{dt} = \frac{v_i(I) R_s}{w}. \tag{2.11}$$

Synthesis

With equations 2.9 and 2.11 we have found the differential equations that govern the evolution of our system:

$$\begin{aligned} \frac{dI(t)}{dt} &= \frac{1}{L_K} \left(I_b R_0 - I(t) \left(R(t) + R_0 \right) \right); \\ \frac{dR(t)}{dt} &= \frac{R_s}{w} v_i(I(t)). \end{aligned} \tag{2.12}$$

Given the correct initial conditions

$$I(0) = I_b; \qquad R(0) = R_\xi = R_s \frac{\xi}{w}, \tag{2.13}$$

one can use numerical simulation to calculate the solution. This has been done in [28] and the results were passed through a *SPICE* simulator to compare them to the real output. This showed a remarkable agreement with their experimental data.

Qualitatively, the results can be interpreted as follows: After the absorption of a photon the normal domain is formed. At this point the current through the sample $I = I_b$. The domain will grow rapidly thereby increasing the resistance of the sample. Because of the inductance of the sample, the current cannot switch to the shunt directly but decreases exponentially with a time constant of

$$\tau_1 \approx \frac{L_K}{\langle R(t) \rangle_{\tau_1} + R_0}, \tag{2.14}$$

where $\langle R(t) \rangle_{\tau_1}$ is the time-average of $R(t)$ over τ_1. During this time I will pass I_m where the domain has its largest extent, then drop until the domain vanishes at the return current $I(t) = I_r$. At this point the current through the shunt is at its maximum of $I_b - I_r$. Since the sample is now completely superconducting again, the current will once more start to flow through the sample instead of the shunt. Again, due to the inductance, this happens with a time constant of:

$$\tau_2 = \frac{L_K}{R_0}. \tag{2.15}$$

The pulse that we see is the voltage over the circuit which can be written as:

$$U(t) = R_0 \left(I_b - I(t) \right). \tag{2.16}$$

Assuming that $\langle R(t) \rangle_{\tau_1} \gg R_0$, this is a pulse with a steep left slope and a smoother right slope.

2.1.7. The detection efficiency

In the following we will sometimes have the need for a quantity describing the overall probability of detection rather than referring to the different underlying mechanisms. I will therefore introduce the local detection efficiency $\mathrm{DE}(\vec{r})$ at fixed operating conditions (I_b, T, λ, ...) which is related to the total detection efficiency by

$$\mathrm{DE} = \frac{1}{A_D} \int_{A_D} \mathrm{DE}(\vec{r}) dA, \tag{2.17}$$

where A_D is the area of the detector. Although the local detection efficiency by itself does not carry any physical meaning, it summarizes the absorption probability of the material and all the effects that influence the critical energy mentioned in Eq. 2.3.

2.2. The laser scanning microscope

The *Laser Scanning Microscope* (LSM) is a very versatile tool used in different scientific areas ranging from 3D-fluorescence microscopy of macroscopic objects like leaves or embryos to the investigation of meta-materials or, in our case, nanoelectronical devices. The basic operation principle is always to focus a laser beam on the sample plane[7] and scan the focal spot across the sample. For each position, a corresponding signal is recorded. The signal, however, can have different origins: Most of the LSMs today operate as confocal microscopes using the intensity of the reflected light as signal [29] source while we are more interested in the electrical response of our samples.

The first part of this section will be about the spatial resolution achievable by this kind of microscope. Afterwards I will go into the details of the measurement scheme used in my experiments beginning with two regimes we distinguish: The single photon regime, in which the photon flux is so low that we can correlate the output signal to the absorption of single photons in the devices mentioned in 2.1 and the high-power regime in which the major part of the signal originates from resistive changes caused by local heating.

2.2.1. Understanding the spatial resolution

There are several factors which limit the spatial resolution of this type of microscope. Some of them are for instance the precision of the mirrors which control the position of of the laser spot, the drift and vibration of all mechanical parts and so on. The main limiting factor, however, as with most scanning microscopes, is the size and shape of the probe i.e. the laser spot. As I am going to explain in the next sections, the area from which the response in both regimes originates is intrinsically linked to the shape of the laser spot. To specify this a bit, I will introduce a highly simplified model which describes the output of a scan with infinitely small step size in the absence of any *real* limitations[8] other than the spot shape. The other factors, and the problems they introduce, will be addressed later in this section. If we assume

$$\mathrm{PSF}(\vec{r}-\vec{r}_0) \qquad \text{with} \qquad \int \mathrm{PSF}(\vec{r}-\vec{r}_0)d\vec{r} = 1$$

to be the normalized *Point Spread Function (PSF)* of the laser spot when positioned at $\vec{r}_0$ on the sample plane. And let us define a hypothetical function $f_i(\vec{r})$ as the *real*[9] response of the sample. Then the output $f_o(\vec{r})$ can be understood as a convolution of these two functions:

$$f_o(\vec{r}) = (\mathrm{PSF} * f_i)(\vec{r}) = \int \mathrm{PSF}(\vec{r}\,' - \vec{r}) \cdot f_i(\vec{r}\,')d\vec{r}\,'.$$

[7] In case of 3D-microscopy the focus is used to scan different slices of the sample which can then be reassembled to form a 3D picture

[8] In the high laser power regime this would also imply a modulation frequency $f_{\mathrm{mod}} \to \infty$

[9] This would be equivalent to the output of a scan in which the $\mathrm{PSF}(\vec{r}-\vec{r}_0) = \delta(\vec{r}-\vec{r}_0)$

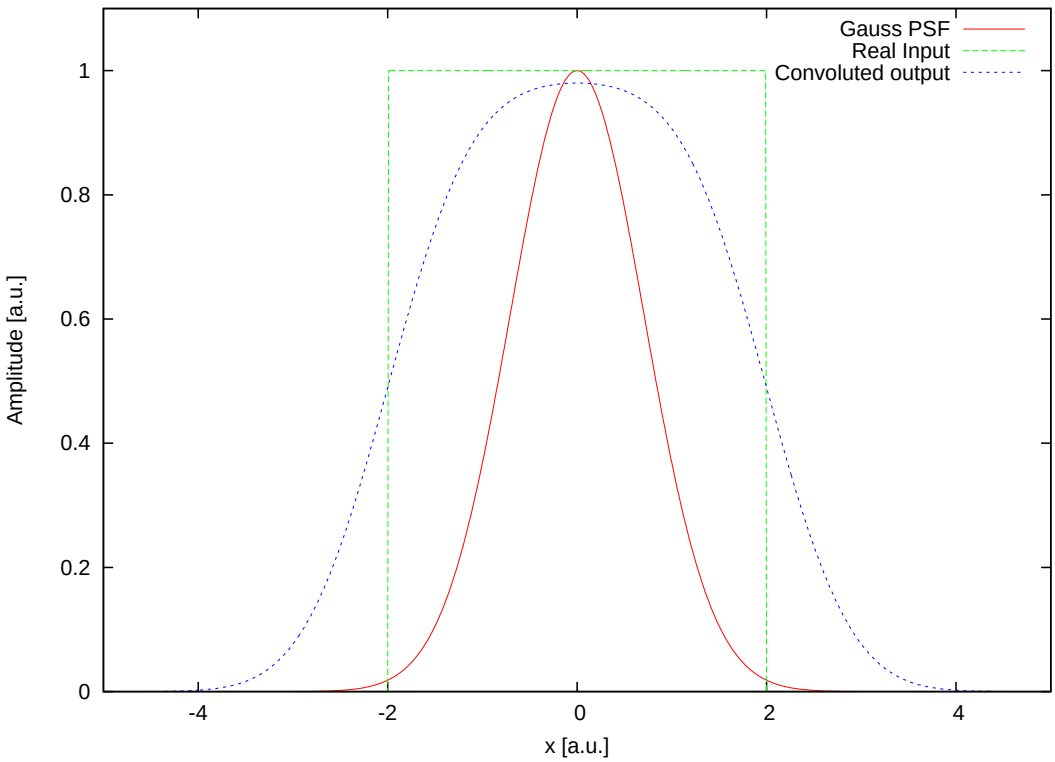

Figure 2.8.: 1D convolution of a Gauss peak and a rectangular step.

This reveals that in principle every point of the output contains information about the whole sample while in reality we can neglect the influence of the laser on the sample in a reasonable distance from the illuminated spot. If this was all there is to it, and $f_o(\vec{r})$ as well as $\mathrm{PSF}(\vec{r}-\vec{r}_0)$ were perfectly well known, we could easily reconstruct $f_i(\vec{r})$ from the data by performing a simple deconvolution. Unfortunately, things are not that simple. The first problem is that we will never have access to $f_o(\vec{r})$ and $\mathrm{PSF}(\vec{r}-\vec{r}_0)$ and we can only measure them with a finite precision[10]. Therefore the deconvolution would have to be a discrete process, while the convolution is a continuous one. The second problem is that by only scanning over a finite area we lose the information stored in the outer regions. On top of that there are all the aforementioned "real-world" influences like noise which contribute to the output:

$$f_o(\vec{r}) = (\mathrm{PSF} * f_i)(\vec{r}) + \epsilon.$$

Where ϵ can be a voltage noise in the high laser power regime or a dark count noise in the single photon counting regime. In the latter case one also has to take into account that the process of the detection is discrete and that the PSF only provides a probability-

[10]The number of pixels in the resulting picture

rather than an intensity-distribution. Although this can be improved by taking a larger statistic (i.e. by increasing the time for each data point) it is an intrinsic factor which obscures $f_o(\vec{r})$.

There are a number of discrete deconvolution algorithms [15] which are even designed to work with additional noise contributions. For my experiment, however, these did not bring much of an enhancement because the feature size of the lines on the samples is a lot smaller than the spot size.

There is one important, yet obvious, criterion that can be used to quickly get a feeling for the actual border-position of a structure when one only knows the approximate size and not the particular shape of the PSF. Assuming that the amplitude of the PSF is negligibly small in a distance r_p from its center and assuming one scans this PSF over a step which is approximately constant in all directions for at least $2r_p$. If one now takes the 1-D central cross-section of the convolution along the scanning direction, the point where the amplitude of this line is exactly half of the maximum minus the minimum value is the position of the original step. As this is of some practical use, I will refer to it later as the *half amplitude criterion.*

2.2.2. The point spread function

In the previous section I have referred to the $\mathrm{PSF}(\vec{r}-\vec{r}_0)$ as the spatial intensity distribution in the sample plane. To maintain generality its actual shape and size were not included in the discussion but shall be discussed now. The focus will entirely be on geometric optics neglecting any kind of nonlinear effects and real-world influences[11]. The main limit which we are confronted with when using light as a probe is of course the diffraction limit of classical optics. It limits the spatial resolution to about $\frac{\lambda}{2}$ and cannot be overcome so easily. There is, however, a lot of additional information in the shape and size of the PSF which I am now going to describe in the case of an objective lens focusing monochromatic, coherent light with a wavelength λ onto the sample plane. It is apparent that the key to finding the PSF is to know the type of light that enters the lens and the transformation which it undergoes passing through the lens.

The first important restriction that we can make while still encompassing most optical systems is that the PSF should have a radial symmetry:

$$\mathrm{PSF}(\vec{r}-\vec{r}_0) \equiv \mathrm{PSF}(|\vec{r}-\vec{r}_0|) = \mathrm{PSF}(r).$$

Assuming that the lens itself is radially symmetric and does not have any preferred axis (i.e. due to crystalline structure) we can conclude that the input to the lens will have to be radially symmetric too. There is an infinite amount of solutions meeting this requirement. I will focus on two of them that are partially present in the LSM: A *plane wave* front and a *Gaussian beam* shown in Fig 2.9. These are classical situation which can be found in many text-books like [17]. For both of those cases the PSFs *Full Width Half Maximum (FWHM)*[12] value, which is commonly used to characterize peaks, can be

[11] i.e. non-ideal behavior of optical components

[12] Diameter of the central area of the spot in which $\mathrm{PSF}(r) > \frac{1}{2}\left(\mathrm{MAX}\left(\mathrm{PSF}(r)\right) - \mathrm{MIN}\left(\mathrm{PSF}(r)\right)\right)$

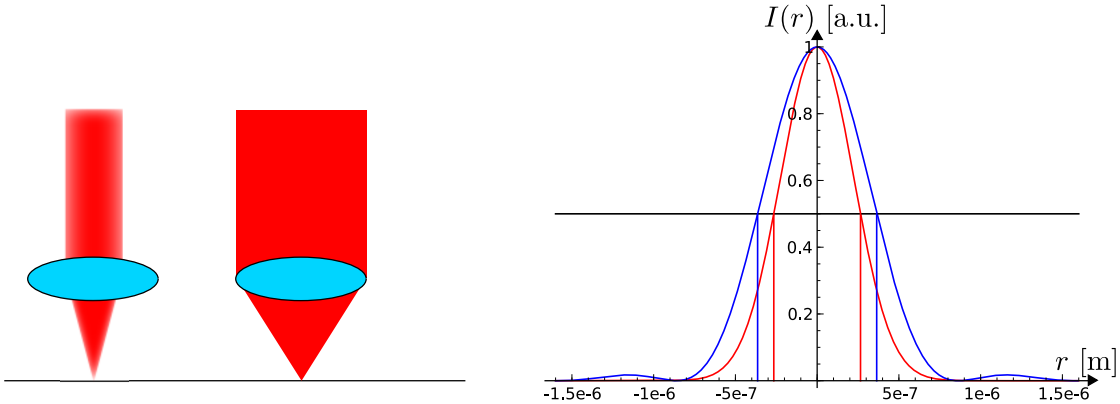

Figure 2.9.: Left: a Gaussian beam and a plane wave being focused. Right: Intensity distributions $I(r) = \mathrm{PSF}(r)$ of the focused Gaussian (red) beam and the plane wave (blue) in the focal plane. The respectively colored lines show the FWHM.

found in Fig. 2.9.

The plane wave front is the case in which the whole objective lens is illuminated evenly by a beam of light, of which the diameter D_b is equal to or larger than the lens diameter D_l. The PSF to be expected in this case is

$$\mathrm{PSF}(r) \propto \left(\frac{J_1(\alpha r)}{\alpha r}\right)^2,$$

where $J_1(r)$ is the Bessel function of the first kind and α is a scaling factor. Qualitatively this can be described as a central large peak surrounded by smaller periodic interference-circles caused by diffraction at the edges of the lens. The area around the origin inside surrounded by the first minimum ring is called the *Airy-Disc* and has a diameter of

$$d_{\mathrm{airy}} = \frac{1.22\lambda}{\tan\left(\arcsin\left(\frac{\mathrm{NA}}{n}\right)\right)}, \tag{2.18}$$

where NA is the *Numerical Aperture* of the objective lens and n the diffraction index of the surrounding medium.

The Gaussian beam is a very convenient solution, in which the radial intensity distribution[13] is a Gauss distribution of the form

[13] Assuming cylindrical coordinates with z as the propagation direction of the beam, r as its radial and ϕ as its angular component

$$I(r,z) = \frac{P_{\text{tot}}}{2\pi w^2(z)} e^{-\frac{r^2}{w^2(z)}}, \tag{2.19}$$

where P_{tot} is the total power of the beam and $w(z)$ is the radius at which the beam intensity has dropped to $\frac{1}{e^2}$ of its peak value . At the focal distance z_f of the beam, the width becomes $w(z) = w_0$ the so-called beam waist. The reason why this situation is so convenient is that by passing through optical lenses, a Gaussian beam is always transformed into another Gaussian beam if the lens diameter D is significantly larger than w. In this case, the lens just transforms the incoming beam, which typically comes from the laser diode and has a rather large beam waist and *depth of field (DOF)*[14], into one with a small w_0 and DOF that we use to scan (see Fig. 2.10).

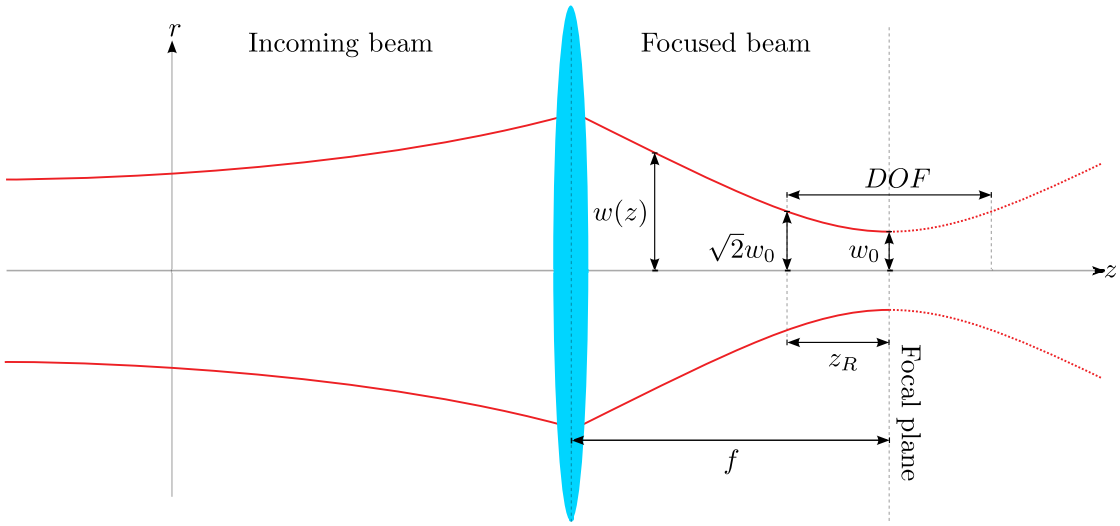

Figure 2.10.: A Gaussian beam with a small divergence propagating in positive z direction being focused by a thin lens with the focal distance f. The right-hand side is also a Gaussian beam reaching its narrowest point with a width w_0 in the focal plane of the lens.

From the w-value of the incoming beam at the lens and the known characteristics of the lens we can easily calculate the new w_0, the key parameter of the outgoing beam that characterizes the intensity distribution (and therefore our PSF) in the focal plane of the lens:

$$w_0 = \frac{\lambda}{\pi \tan\left(\arcsin\left(\frac{NA}{n}\right)\right)}. \tag{2.20}$$

[14] I will from now on use the definition that the DOF $= 2z_R$ is the distance between the two points where $w(z) = \sqrt{2} * w_0$. z_R is called the Rayleigh-range.

The question remains in how far any of the two situations matches a real setup; but this will be discussed in section 3.2.

2.2.3. Two operating regimes

As I have already pointed out in the introduction to this section, the LSM is quite a versatile tool in terms of different measurement schemes. Although the source is always laser light, the reactions and corresponding signal types are as divers as the samples being used. In my measurements I have been using two slightly different setups working in two different regimes which I will describe in this chapter: The *high-power regime* and the *single photon regime*. But before we delve too deeply into the details of each of them it must first be pointed out why they are indeed different and have to be treated differently and what exactly makes up this difference.

As one may have guessed from their names, these two regimes represent two different levels of optical power, the single photon regime being the low-power end of the scale while the high-power regime describes the high-power limit. The obvious question is why these two cases have to be treated differently. The answer to this lies in the quantum nature of light and in the reaction of the samples to single photons. Let us assume that the sample shows a measurable reaction to a single photon and takes a time τ_r (see Sec. 2.1.1) to return to its initial state. If we now compare this time to the average time between two photons coming from a laser source $\tau_p = \frac{\hbar\omega}{P_{\text{laser}}}$ we can distinguish the following extreme cases :

$\tau_r \ll \tau_p$ The average time between two events is much longer than the time it takes the detector to reset. This means almost every photon will reach the detector in its equilibrium state where it can trigger a response. In this case we can count the number of responses per time and it should be linearly proportional to the power as long as the criterion is fulfilled. Consequently, we call this situation the single photon regime.

$\tau_r \gg \tau_p$ The average time between two pulses is much shorter than the reset time. This means that we can no longer attribute the response to the absorption of single photons. Apart from the fact that this situation is not sufficiently well described by our model (Sec. 2.1.6), the high local dissipation usually leads to an increased local temperature. This situation is called the high-power regime, since we usually measure resistance changes depending on local temperature changes.

In between the two regimes there obviously has to be some kind of crossover which is not well described by either model.

The high-power regime

The technique used to measure the resistive response using high laser power levels

$$\tau_r \gg \tau_p \tag{2.21}$$

is very well developed and has been successfully used in numerous experiments [2, 31, 32]. Its benefit is primarily to provide a signal proportional to the local critical current density at the laser spot position. The basic scheme is to measure the voltage drop across a current-biased sample in the presence of laser illumination. In this subsection I am going to briefly summarize the effects of this local excitation on the global resistance of the sample. We also modulate the laser in order to minimize the area of the thermal spot contributing to the signal as will be shown later in this subsection. But let us first take a look at what happens to the electrical properties of a typical sample under illumination.

The processes happening for each photon are the same as described in the hot-spot model in Sec. 2.1.3: Quasiparticle excitation, relaxation down to excitations of $E \approx \Delta$, phonon escape and so on. The only difference is that due to the rate of incoming photons a steady influx of energy leads to a local increase in temperature. The resulting change in the Cooper-pair density in turn leads to changes in the critical current density, kinetic inductance, etc.

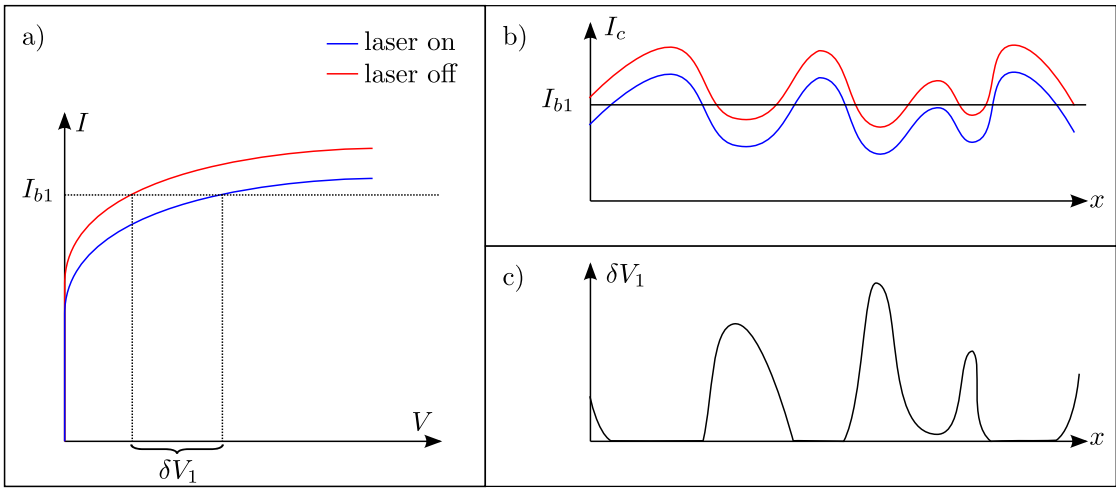

Figure 2.11.: a) Change in the I-V curve of a quasi-1D wire due to illumination. b) Critical current along the scanning direction x c) δV for the above example as a function of the illuminated position.

We can now take a look at a quasi-1D wire being much larger in x-direction than ξ and λ and smaller in y- and z-direction biased below the critical[15] current. Illuminating the wire at one point would change its I-V characteristic similar to what is shown in Fig. 2.11a. Biasing the wire at a constant current I_B, we can see a change in the voltage drop over the sample δV. Figure 2.11b shows an example of the local critical currents along the x axis with and without illumination. Scanning the light along x, only illuminating a small section of the bridge at a time, we can create a graph of

[15]The current would actually have to be smaller than the retrapping-current to prevent quenching.

$\delta V(x)$ as is illustrated in Fig. 2.11c. From this information it becomes evident that in general a higher photo-response signal δV corresponds to a lower critical current I_c of the illuminated cross-section.

There is one technical aspect of the measurement scheme used with this regime that deserves a closer look in this section. The fact that we modulate the laser beam intensity with a frequency f_{mod} and use a lock-in amplifier to measure δV may at first glance seem like a technical detail only used to improve the signal to noise ratio. Although this is certainly one positive effect, there is another reason why the modulation improves the result significantly which has to do with heat diffusion inside the sample. Illuminating and thus heating one spot of the sample, the heat generated there will not remain inside the illuminated but spread into the surrounding area and create a thermal spot which can be much larger than the actually illuminated spot. As our measurements are based on temperature-induced changes in the superconducting properties, this means that our photo-response is caused by the thermal spot instead of the illuminated one. This would have a dramatically negative impact on the spatial resolution of this technique. Since the heat diffusion does not take place instantaneously but over a time τ_D we can exploit this fact by modulating it with a frequency $f_{\mathrm{mod}} \gg \frac{1}{\tau_D}$ [7]. The effect of this is that the response can be split in two components: $\delta V = \delta V_{mod} + \delta V_{avg}$ where δV_{mod} is the response from the area under illumination and its close surrounding in which the temperature change happens with the modulation frequency. δV_{avg} is the contribution of the rest of the thermal spot. Because the temperature changes under the spot happen so rapidly, the regions further away will only see an average heat flow and therefore add a time-independent contribution to the overall signal. The lock-in amplifier does the rest of the work by selecting only the modulated part of the signal so that the effective area contributing to the signal is the illuminated spot and the area with a distance of approximately

$$\Lambda_{mod} = \frac{\Lambda}{\sqrt{\omega_{mod}\tau_D}} \tag{2.22}$$

around it (Λ is the thermal healing length). Figure 2.12 shows a sketch of this process. This means that by choosing a sufficiently large modulation frequency we can neglect the influence of the thermal spot and return to the description sketched in Sec. 2.2.1 in which the spatial resolution is mainly limited by the PSF of the laser spot.

The single photon regime

Whenever we use the LSM to investigate devices that show a response to single photons like those mentioned in Sec. 2.1, we can choose to map the detection probability instead of the resistive response. In this case we have to attenuate the light intensity[16] to a level that satisfies the criterion detailed earlier:

$$\tau_r \ll \tau_p \tag{2.23}$$

[16] In this regime another approach would be to use a single photon source

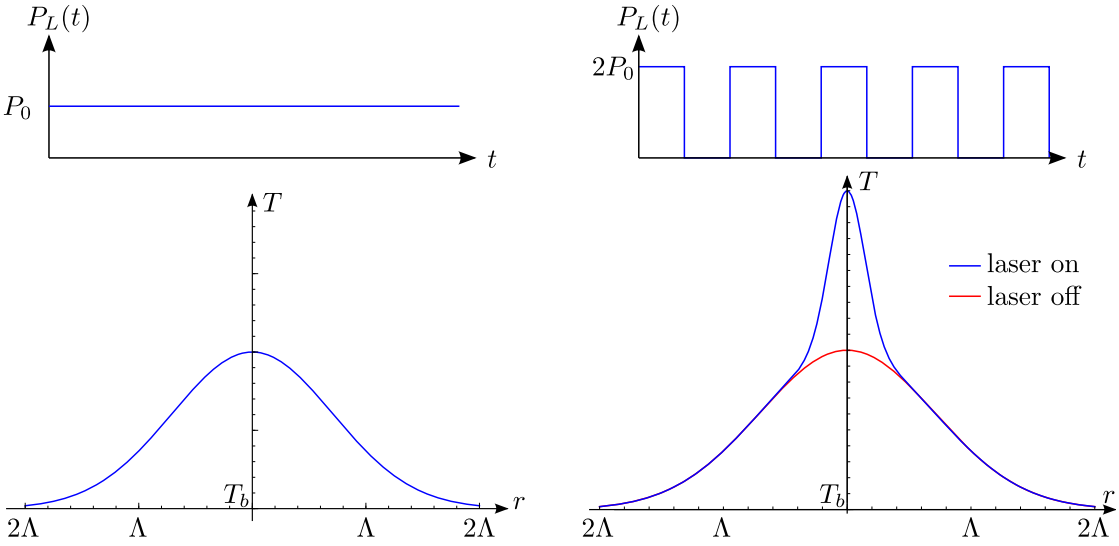

Figure 2.12.: Schematic distribution of the local temperature increase above the bath temperature T_b for an infinitely sharp laser spot at $r = 0$ in the case of constant wave illumination (left) and modulated illumination (right) with $f_{\text{mod}} \gg \frac{1}{\tau_D}$ and the corresponding laser power L_p. For the modulation, only the area very close to the excitation changes its temperature with the frequency f.

The result we expect from such an experiment is rather simple: We characterize the detector by a spatial detection efficiency function $\text{DE}(\vec{r})$ as introduced for an SNSPD in Sec. 2.1.7. Although the DE is here somehow linked to the critical current of the cross-section enclosing the location of absorption, the result should not follow this value directly. Moreover, the detector should, if biased correctly, show a homogeneous DE even for slight variations in I_c.

3. The experiment

3.1. Idea and goal of the experiment

The idea of the work done during my diploma thesis was to provide experimental means to conduct spatially resolved experiments on SNSPDs which provide information beyond what was already known from resistive measurements. For this reason we chose to operate the detectors in the regime they are made to work in by using low optical power levels and counting single photons. By combining this approach with the existing laser scanning technique we were able to provide information about the spatial homogeneity of the detectors that was formerly unavailable. The three steps devised to achieve this were:

1. **Modify the existing LSM setup** in order to be able to spatially map single photon count-rates. Apart from the installation and setup of new equipment this also meant the design and realization of new hard- and software which will be described in this chapter. With this new setup the plan was to move on and

2. **Measure spatially resolved photon detection rates** on existing SNSPDs and see if their overall detection efficiencies are limited by parasitic effects like constrictions or not. The results from these experiments will be presented in Sec. 4.1.

3. Use the newly gained knowledge to **devise a new sample layout** for studies of whatever seems promising from the first results. This will be discussed in Sec. 4.2 and Sec. 4.5.

Since the first main goal was to set up an experiment for single photon mapping, this step absorbed a major part of the time scheduled for the experiment. Fortunately most of the optical and cryogenic components had to be only minimally modified to work in this setup. The description of these I am going to give in this chapter is consequently more a summary of the work of others[1]. The electronics required some more attention as the voltage pulses which were to be counted are both quite short and low in amplitude. This meant designing a new sample holder together with a 50 Ω matched coplanar waveguide to the sample to reduce mismatching effects. Moreover new microwave components had to be installed inside and outside the cryostat. Finally, the counter itself had to be fast enough to reliably count all the pulses. Since the counter we had to our disposal proved to be too slow for some of our samples, we decided on building a fast counter ourselves.

[1] The optical part was mainly built by Dr. Alexander Zhuravel and the cryostat by Dr. Sasha Lukashenko

The final piece of setup needed for the experiment was a suitable measurement software because the existing one only allowed analog voltage response signals whereas we wanted to use the actual number of counts over a timespan.

3.2. Optics

The optical system as depicted in Fig. 3.1 is the key part of the laser scanning microscope. A red laser[2] beam[3] coming from a laser diode[4] is focused into an optical fiber. In the focusing stage there is also a slot for optical filters which I use to attenuate the laser power by inserting neutral density filters. The optical fiber leads to the top part of the microscope where it is connected to the mirror box. The beam leaves the fiber and gets parallelized again. It is then reflected by the two scanning mirrors used to change the x/y spot position in the focal plane. The beam propagates downwards where it passes a two lens system after which it reaches a beam splitter cube. One half of the light is diverted to the left where it reaches a laser power meter. The other half travels on downwards and finally reaches the objective lens through which it is focused onto the sample. Light reflected by the sample traveling the opposite way will be in part reflected to the right by the beam splitter cube. This light is then again split between a photometer and a CMOS camera. A white light source is also attached from the right side which is used to illuminate the sample during the positioning process. The whole device is mounted at the edge of a vibration- and shock-dampening optical table. The positioning and focusing is done via three positioning screws at the side and back of the device which can be replaced by positioning motors if large areas are to be scanned.

One of the simplifications usually made in laser optics is the Gaussian beam approximation. In reality, however, we have to concede that the PSF we observe is neither purely Gaussian nor does it, in terms of spread, come close to the optimum we would expect from the theoretical treatment of Sec. 2.2.2. The reasons for this could be manifold, and a thorough treatment of the matter would surely exceed the scope of this work. But there are of course some standard problems. Maybe the main reason for non-Gaussian results is the limited size of the optical components. The assumption that the optical transformation of the Gaussian beam is still approximately a Gaussian beam only holds true if the optical components are much larger in diameter than the beam waist. This is definitely not the case for our setup, since some of the parts are only a little larger than the visible beam. The mirrors for instance may cut off a part of the beam, and diffraction at the edges of the objective lens can lead to fringes. Another source of errors are simply a non-ideal behavior of the optical parts and unclean surfaces. To find out what the actual laser spot looks like, there are two approaches:

Use the reflected image from the camera. This is a straight-forward approach to get an idea of the spot diameter and shape. The camera itself though is not a calibrated

[2] typically $\lambda = 655$ nm or $\lambda = 635$ nm

[3] When speaking of a beam, I always refer to an ideal Gaussian beam as introduced in Sec. 2.2.2

[4] Two different models are available: A 655nm and a 635nm model. In my measurements I used the 635nm one.

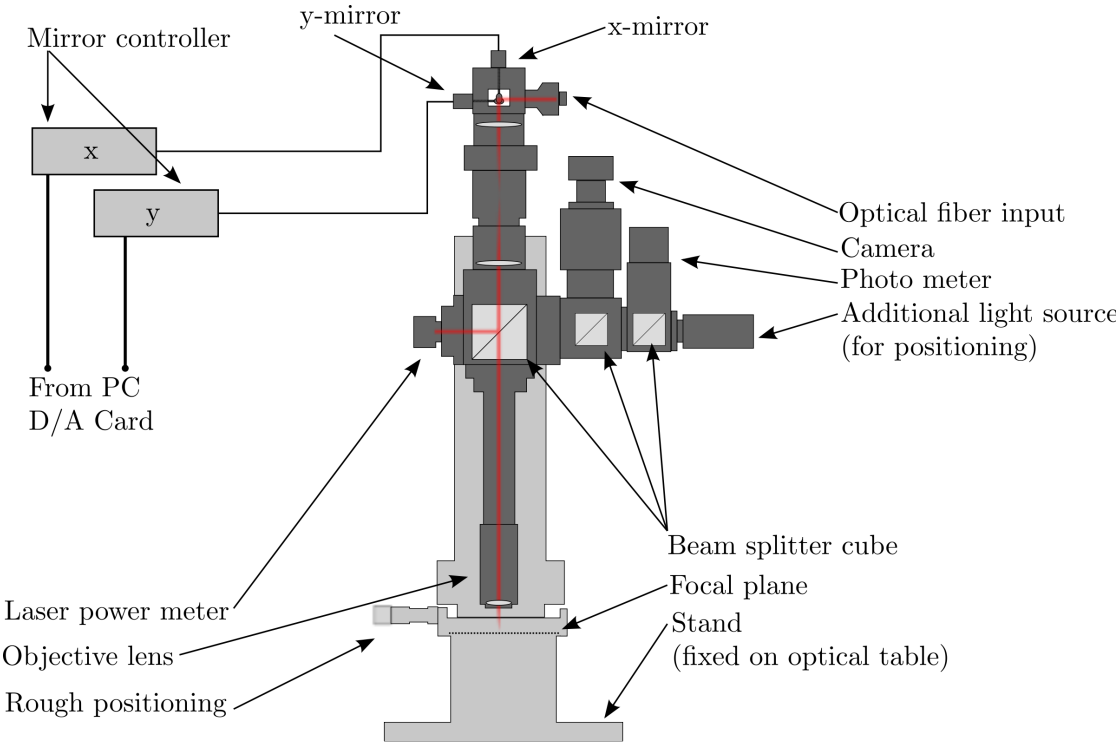

Figure 3.1.: Schematic view of the Laser Scanning Microscope.The red parts show the laser light if no reflected light travels back through the system.

scientific instrument and the brightness-information it supplies does not necessarily have to have a linear correspondence to the actual intensity. One more problem is the additional optical path the returning light has to pass which will make the camera image look more blurred than the actual one.

Use the electrical signal while scanning a known structure (i.e. a single step). Although this is certainly the better technique in terms of accuracy, it creates another problem: The output is again a convolution of both the PSF and the known structure which means that the PSF first has to be extracted from the results. In order to get the electrical signal one has to have a special sample and cool it down which makes this technique unsuitable for a quick check.

In Fig. 3.2 the result of the first approach is shown. The picture on the left was taken next to a grid, so the resolution of 257 $\frac{nm}{px}$ could be extracted. Although none of the fit curves match the data perfectly, we can see that the "Airy-type" one provides a better approximation. Its most prominent feature, namely the zero-crossing at the edge of the Airy-disc, can also be seen in the data. Although we know that this result is to be treated carefully (due to the limitations mentioned above) we found the experimental

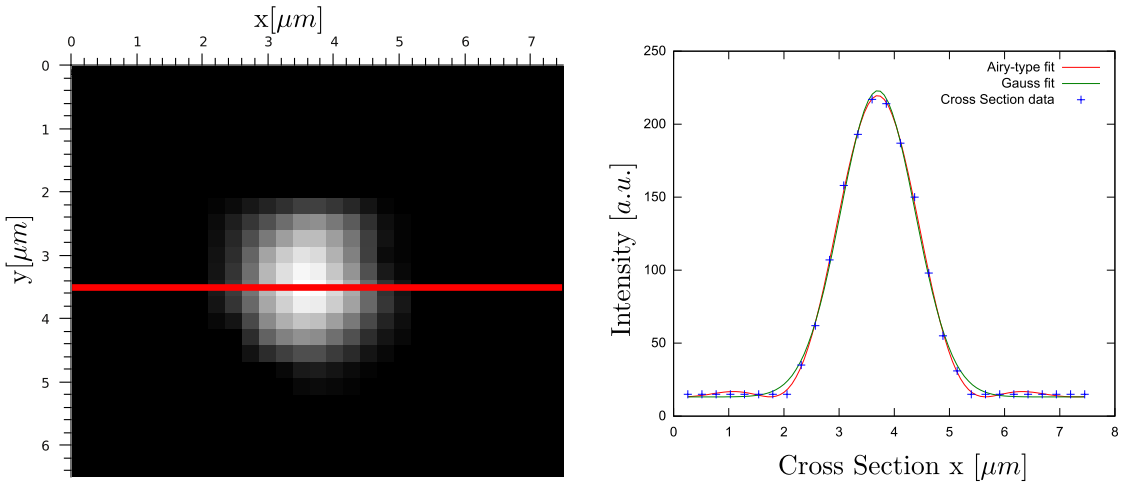

Figure 3.2.: Left: Camera image of the laser spot. The red line marks the cross-section used for the right side. Right: Cross-section data from the image on the left. Fit curves of Gaussian- and "Airy-type"-profile (see Sec. 2.2.2).

results to show a remarkable agreement with simulated data using the PSF extracted from the camera image as can be seen in figure 3.3.

Here we see the comparison between a real photon map and a simulation using the PSF from Fig. 3.2. It is clearly visible that the detector area on the measured image looks smaller than in the simulation. There are several possible explanations for this:

1. The active area of the detector was taken to be $4 \times 4\mu m^2$ in the simulated picture. From ealier considerations (see Fig. 2.1 for reference) we expect the actual active area to be smaller than that.

2. The PSF from Fig. 3.2 is indeed not a perfect image of the actual one as we proposed earlier. From all we know this seems to be a plausible assumption considering the fact that despite the smaller width of the signal area, the top plateau seems to be a bit larger than in the simulation.

3. The x- and y- coordinates are not exact. Although the system was calibrated before the measurements there is some margin for error.

3.3. Cryogenics

The detectors used for this study work in the superconducting state and so they have to be cooled below their critical temperature. For this reason, one of the goals of superconducting nanoelectronical devices is always to increase their T_C in order to minimize the effort needed to operate them. For NbN-detectors, the transition temperature $T_C \approx 10K - 15K$ which means that they can be operated at $4.2K$ using liquid helium

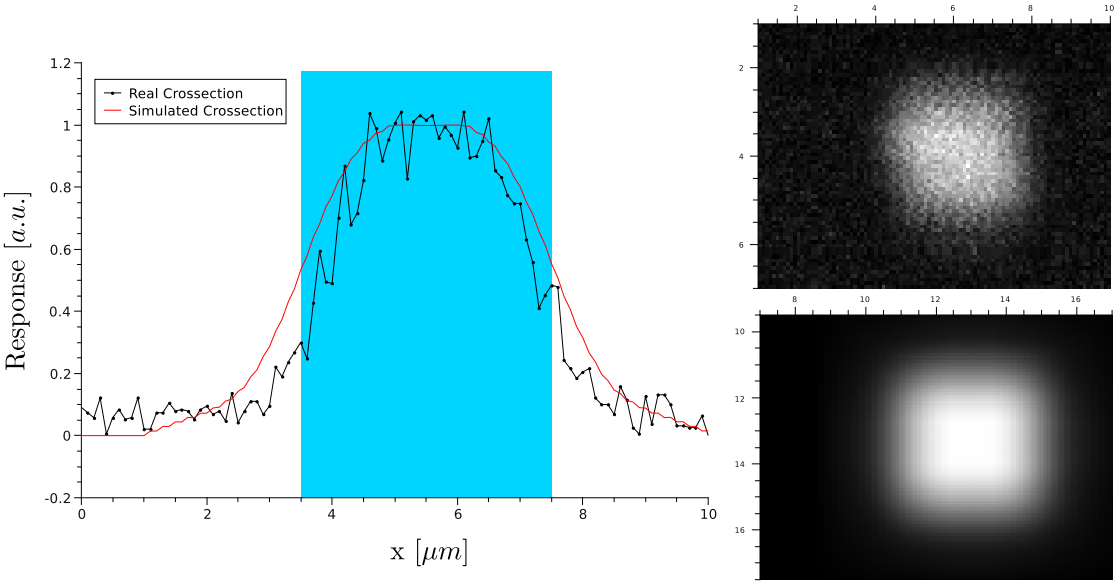

Figure 3.3.: Left: Comparison between the central horizontal cross-sections of the two right-hand images. The colored area indicates the approximate detector position. Right: A real photon-map (top) and a noiseless simulated one (bottom) using the camera PSF.

cooling. Although this is still more complicated than high-T_C samples that can be cooled by liquid N_2 it is still a lot better than most known superconductors which require even lower temperatures and therefore more complicated techniques[5].

Remembering the three ways of heat transfer every Dewar(-flask) prevents by minimizing

- Radiation
- Convection
- Conduction

one can realize that there is one paradox in this experiment: On the one hand we need to cool the sample to keep it at a constantly low temperature while on the other hand we have to leave some window in the cryostat which inevitably undermines our effort to minimize heat transfer by radiation. This means that there has to be a compromise in the design of any optical cryostat. I will now shortly describe the optical (flow) cryostat designed and built by Dr. Alexander Lukashenko which was used for most of my experiments.

The design parameters for this cryostat were matched to the requirements of the LSM which were mainly to create a device which

[5] i.e. 1K-pot or dilution cryostats

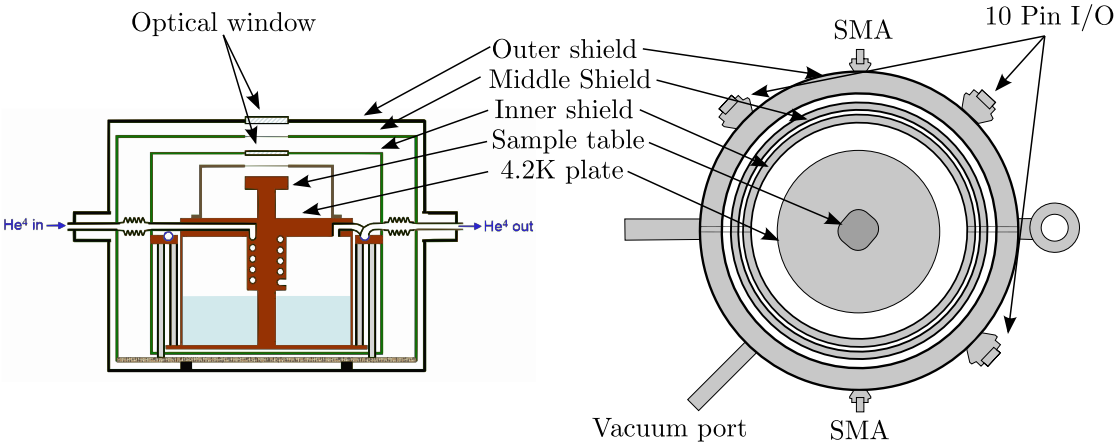

Figure 3.4.: Schematic side- (left) and top-view (right) of the optical cryostat

- Provides optical access for the laser outside of the cryostat to the sample placed on the inside without losing too much cooling power through the window.
- Holds enough liquid ^{4}He to last for several hours of continuous measurement while at the same time allow for a quick exchange of the samples by keeping the cooling-cycle time low enough to run one experiment per day.
- Does not require liquid nitrogen.
- Is compact and nicely fits the dimensions of the rest of the LSM.

The result of this effort can be seen schematically in Fig. 3.4. The sample sits on a table which is screwed into the 4.2K plate. A heater and a socket for a thermometer are part of the table and are used to stabilize the temperature via an external feedback temperature controller. The 4.2K plate itself is the topmost part of the ^{4}He-bath. It is surrounded by two polished shields, the inner one, which is cooled by the outgoing He-vapor, being at a temperature about 70K, and the outer one floating between the inner and outer temperature. The inner shield has a glass window which, being at the same temperature as the metal parts, absorbs some of the heat radiation coming from outside. All of this is enclosed in the outer hull which has a second glass window in its lid. A top-view of the cryostat with the different shield-lids attached can be seen in Fig. 3.5.

Before filling the helium bath, the inside of the cryostat is evacuated which minimizes heat transfer by convection. Using materials with low thermal conductivity like stainless steel between parts at different temperatures helps reducing heat conduction while the polished surfaces inside the cryostat dampen heat transfer by radiation. There are three 10-pin DC- and two RF-lines going into the cryostat. The DC-lines are made from constantan and the RF-lines from copper-beryllium which both have a rather low thermal conductivity. They also have to pass every temperature stage before being

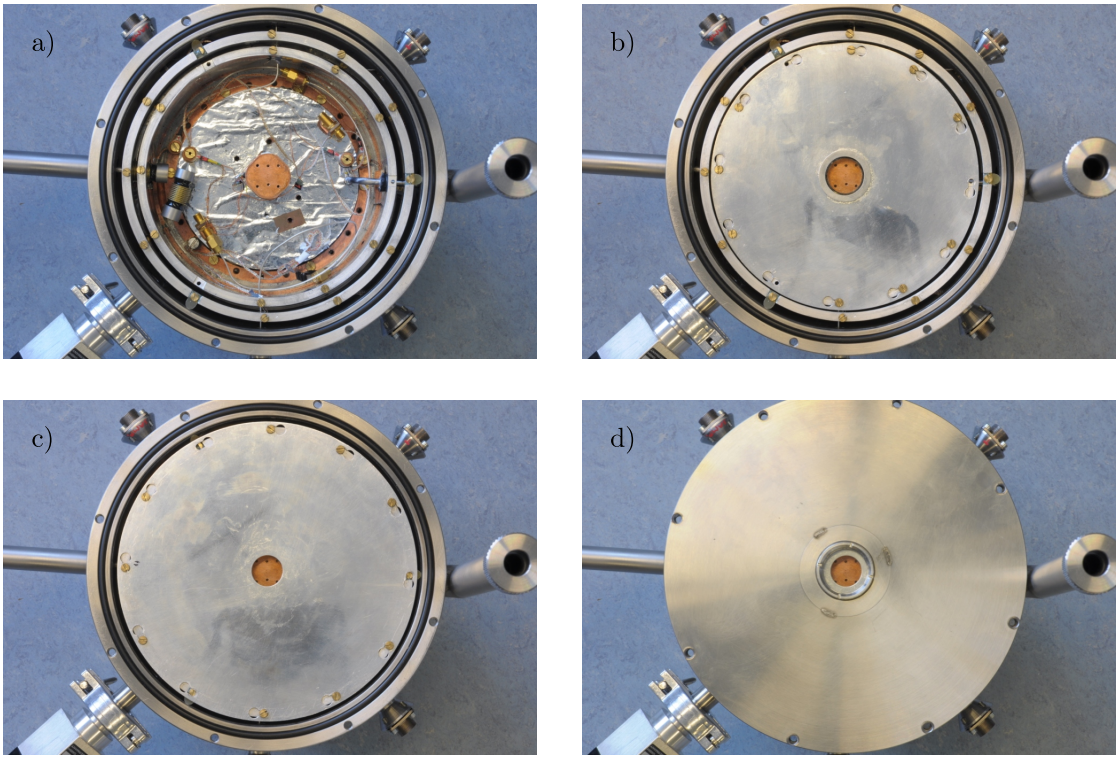

Figure 3.5.: The optical cryostat a) without any top shields b) with the inner shield c) with the radiation shield d) with the outer shield

connected to the sample or other devices mounted on the 4.2K plate. This technique greatly reduces an unwanted heating of the samples and devices.

In summary, the cryostat can be assembled, evacuated, filled and cooled with ^{4}He in less than two hours. The amount of helium usually lasts for another three hours. If more measurement time is needed, the cryostat can be refilled at this stage in only a few minutes. The easy-to-use layout allows for a quick change of experiments while offering enough space to accommodate additional devices like amplifiers or couplers. When used in conjunction with the rest of the LSM the setup is sometimes referred to as a *Low Temperature Laser Scanning Microscope (LTLSM)*

3.4. Electronics

In the following I am going to briefly summarize the electronics used for the single-photon-type measurements. One of the tasks of this experiment was to devise a method to correctly bias the sample and extract the outgoing signal. The current-biasing part was quite easy to solve since this technique is used in many other experiments and all the necessary equipment was already available. A battery-powered, computer-controllable

current source provides the bias current. The DC lines of the cryostat then carry the current to the inside where they are connected to the DC-path of a commercial[6] bias-tee.

This device is necessary since the detectors only have one port which serves as a current input and voltage output at the same time. The bias-tee separates these two components by combining a (low-pass) DC-port with a (high-pass) RF-port into a combined AC+RF port. In the simplest models this can be achieved by using a capacitance C in the RF- and an inductance L in the DC-path. Wide-band commercial models usually use a more complex design but the basic idea is the same. One positive side-effect of using such a device to bias the sample is that by entering through the DC-port, most of the high frequency AC current-noise (like components of radio signals or $2.4GHz$ devices) gets filtered. So there is no need to install additional filters.

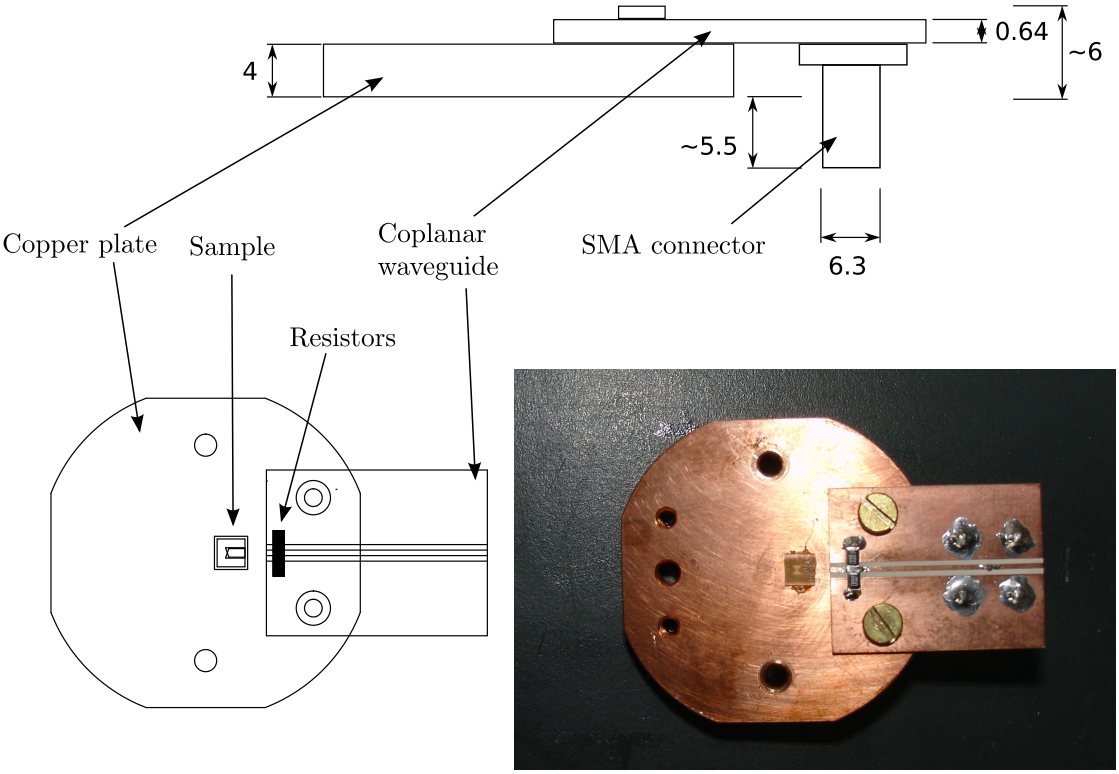

Figure 3.6.: Sample holder and readout line. Top: Schematic side view (length numbers in mm). Bottom: Schematic top view and top view image.

The RF+DC port of the bias-tee is connected via a short, flexible, 50Ω coaxial cable to a 50Ω grounded coplanar waveguide (CPW) which is mounted on top of the sample holder plate. The whole design can be seen in Fig. 3.6. For the CPW we chose a material[7] with a low thermal coefficient of the dielectric constant. On top of the CPW there are

[6] Minicircuits ZX85-12G+ 200kHz-18GHz
[7] Rogers TMM10i

two parallel 100Ω shunt resistors connected from the central strip to the ground plane. From both the I-V characteristics at higher currents and the temperature dependence of the resistance above the transition we know that at 4.2K the resistance of these shunts is approximately 134Ω each. The end of CPW is connected to the sample by Al+1%Si wire-bonds.

The RF-port of the bias-tee is connected to one of the coaxial lines leading out of the cryostat. Alternatively we have the possibility of installing an additional cryogenic amplifier directly after the bias-tee which is particularly interesting if a lower noise-temperature is required. For simple pulse counting, however, we realized that room-temperature amplifiers are sufficient and have the advantage of not putting any unnecessary additional heat load on the cryostat. For this purpose we connect two commercial $+20dB$ amplifiers[8] in series outside the cryostat.

The last step is to have a suitable device to count the pulses over a duration of time. There are a few different possibilities of how to realize this of which we have experimentally tried out the following ones:

Oscilloscope traces. Modern memory scopes have the possibility of storing time traces of a signal in their memory which can be analyzed to find peaks. On the positive side one can say that they are usually very sensitive, fast[9] and readily available in almost any lab. Unfortunately there are some drawbacks: Firstly, the memory usually limits the maximum time for one trace at a fixed sampling rate. This means that at rates needed for experiments like this one, the traces can usually only be a few milliseconds long. Of course one can solve this by taking many measurements and average over them, but this makes the whole process rather slow. The second problem is the data analysis. As none of the scopes available at our lab had the possibility of counting the peaks in the scope and only transfer the result, the only way to proceed was to transfer the entire trace to the computer and do the analysis there. Not only does the transfer itself take a noteworthy amount of time (since the traces are quite large in memory), but also the processing is another factor which makes the data acquisition quite slow[10].

Commercial pulse counter (in our case: Stanford Research SR620). These devices can count the number of pulses exceeding a definable threshold over a timespan set by the user. This is, in principle, the best solution, since the final result (the number of pulses during the measurement) is available to be read out by the computer directly after the measurement period ends as no additional processing is needed. This is particularly important because for high-resolution imaging a lot of data points are required. In the case of our device, there is one very important drawback: The internal electronics of these devices limit them to an operation of about $250MHz$. While this may not be dramatic for the detection of pulses that are comparatively

[8] Mini-Circuits ZX60-3018G+

[9] A $1GHz$ scope is usually enough to see almost any pulse even for samples with a very low inductance

[10] As a comparison: In the experiment in Israel we were able to measure, read out, and analyze $50ms$ traces in about $1s$. A typical image of 70x100 pixels, which takes about 8 minutes using a pulse counter, would take around 2 hours with this method.

long, it effectively makes the device unusable if the pulse duration becomes less than the clock durations of the electronics. Obviously, this limitation is purely technological and can be solved by simply buying a better device.

Dedicated counting electronics. Although this is by far the most complicated way one can choose to reach the declared goal, we decided to build a pulse counter ourselves. The main reason for this was that we have samples which generate pulses too short to be counted with the existing commercial counter and we did not want to spend money on a faster, expensive device. Apart from the effort and time this project consumes, it has some clear advantages: It is made to fit the requirements of the experiment so that, once in operation, there should be no major drawbacks compared to any of the other solutions. The hardware needed to build a suitable device is actually quite inexpensive; the final version of our device will most probably consist of hardware worth less than a few hundred euros. While of course the development itself consumes far more than that. Since the development of this device took up a significant fraction of my work time, it will be outlined in detail in the Appendix.

The last step in the data acquisition chain is then to read out the data from the counting device. As noted above the method used for this task depends on the counting device itself.

For the resistive measurements the setup also depends on the modulation frequency of the laser. If it is close to or higher than the lower frequency limit of the bias-tee AC-path, one can use the same setup as described above and just replace the room-temperature amplifiers by a lock-in amplifier. Although this is quite convenient if one wants to use both schemes during one cool-down, the modulation frequency is usually chosen to be lower than that[11] and then the sample has to be connected using a four-point probe scheme by the DC-wires.

3.5. Software

The last missing piece in the experimental setup is the software that creates an image by coordinating the input and output of the microscope and displaying it in a suitable fashion. For the resistive measurements a complete software solution already existed[12] at the start of this project. This labview application encompasses all the functionality needed for this type of measurement.

Since the modification of this software to fit the requirements of the new experiment was not easily realizable at the time, we arrived at the decision to develop a new application which could cover both measurement schemes in one application while avoiding some of the problems the other program has due to its labview heritage. As with the

[11] The reason is that the laser diode we are using would be out of its specification.

[12] Written and maintained by A. Glukhov from the Institute of Low Temperature Physics, Kharkov, Ukraine

dedicated counting electronics, the developement of this software will be explained in detail in the Appendix.

3.6. Technion equipment

In this section I will give a short summary of the experimental setup used for the experiments at Technion university. As the equipment used here was quite different to the one we use, their setup provided the chance to verify our results and focus on other parameters like optical power which are not easily adjustable in our setup.

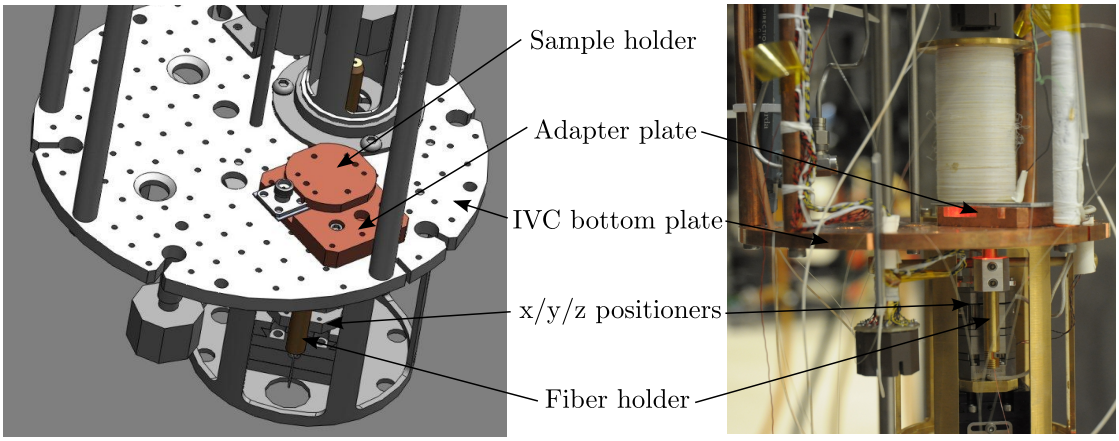

Figure 3.7.: Picture and 3D-model of the central part of the IVC. The 3D-model and adapter plate were made by Gil Bachar and Oleg Shtempluck.

One of the main differences in comparison to our setup is that all measurements at Technion were carried out inside a dilution cryostat. Although this adds some complexity to the measurement process, it also offers the opportunity to cover a much wider temperature range from the transition down to the milli-Kelvin range. The central part of the *inner vacuum chamber (IVC)* where the sample was mounted can be seen in Fig. 3.7. To place our sample there, we chose to build an adapter and mount our sample holder together with the RF-connection (as seen in Fig. 3.6) instead of re-gluing and re-bonding everything to a different sample holder. This way, the sample is positioned face-down above a hole in the bottom plate through which an optical fiber is fed.

As this cryostat has no window to illuminate the sample, light is transferred to the inside using optical fibers. An immediate advantage of this technique over our setup is that all the surfaces facing the sample are at low temperatures and we do not expect to see any dark count contribution from thermal radiation. However, this also means that all the focusing and positioning has to be done inside the cryostat which again increases complexity.

To get a focal spot suitable for scanning purposes from an optical fiber, a lens is made by connecting a short section of *graded index fiber (GIF)* to the end of the single-

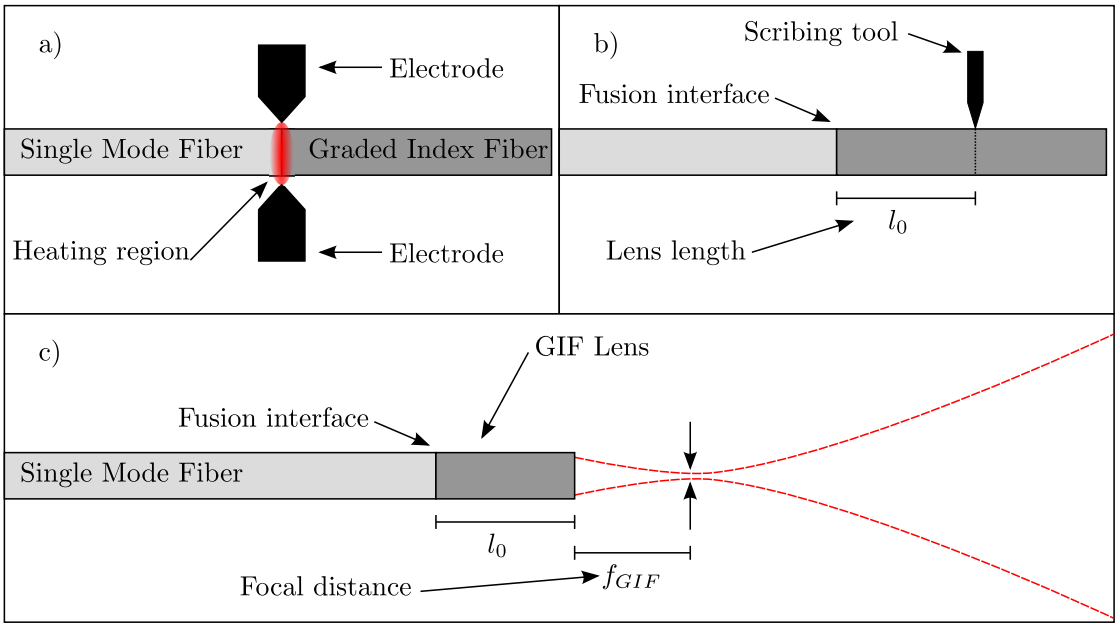

Figure 3.8.: Making a fiber lens. a) A piece of graded index fiber is spliced onto the single-mode fiber. b) A scriber is used to cut the GIF-section to the designated length. c) The finished lens focuses a Gaussian beam.

mode optical fiber [4] leading into the cryostat. Figure 3.8 shows the process starting with *fusion splicing* in which an arc discharge is used to melt the two fibers together. In terms of mechanical stability and optical losses these splices are the best choice to connect fibers. According to the experience of the Technion group, typical losses in their splices are around $-0.1dB$ and focal spots $1\mu m$ in diameter can be reached when using $1550nm$ infrared light.

To position and focus the lens, the fiber is inserted into a holder connected to three linear piezo-positioners[13]. Through a controller outside the cryostat these can be operated in a closed loop. In x- and y-direction, the piezos have a scanning range in which they expand linearly with the applied voltage V_p of about $0.8\mu m$ at 4.2K ($5\mu m$ at 300K). Since this is obviously not enough to cover larger areas, the controller sends a saw-tooth-like signal to the piezos which are only connected to the moving part by a friction contact. The resulting stick-slip motion gives them a total travel range of about $3mm$. To use these positioners for scanning purposes, there are three approaches:

- If the structure to be scanned fits within the scanning range of the positioners, the best choice is to scan by applying a dc-voltage V_p to the piezos. I will call this method **smooth scan** from now on.

[13] Attocube ANPx51/z51

- If the scanning range is too small to cover the area of the sample, one can also just supply the controller with the x- and y-coordinates of a desired position to which it will then move. The controller will move as close to the position as it can using the stick-slip principle and then fine-position by applying a dc-voltage. Although this is very easy to implement, it is also very slow. To this method I will refer as the **absolute scan** later.

- As a compromise between speed and precision in cases when the smooth scan cannot be used, there is also the possibility of applying a number of voltage pulses between every pixel of the scan resulting in an equal step size. This **step-scan**, however, is more suited for 1D scans since the steps are not only different from one positioner to the other but also for forward and backward motion.

After every significant temperature change there is the need to refocus the fiber lens. This is done by coupling a high-power light source into the optical fiber and measuring the intensity of the reflected signal while slowly approaching it towards the sample. The returned power rises slowly as the fiber approaches the sample until the focal distance of the GIF-lens[14] is reached. Approaching even further will lead to a sharp decrease in the intensity of the reflected signal.

All the fibers in the system are single-mode for $\lambda = 1550nm$ light and for all the measurements we used a $4mW$ wide-band ($\lambda = 1550 \pm 50nm$) light source. This was connected to a computer-controllable optical attenuator (0dB to -100dB) which allows for easy power-dependent measurements.

Most of the electrical connections are similar to our setup. The bias-tee[15] and amplifier[16] used in this experiment are both at cryogenic temperatures. The higher band of the amplifier explains the undershoot observed in these measurements. The software is written in MATLAB and uses the *instrument toolbox* to communicate with the instruments.

[14] Typically $f_{\mathrm{GIF}} \approx 40\mu m$
[15] Pasternack PE1607 100kHz-18GHz
[16] MITEQ AFS3-01000800 1 GHz- 8GHz

4. Results and conclusions

In Sec. 3.1 I stated the goals of this experiment and now I will elaborate on the topic in how far they have been reached. The first goal was to set up the experiment by modifying the LSM in order to be able to image single photon counts. All the necessary steps were taken to realize this as explained in the previous chapter.

The next step was to test the setup using existing SNSPDs. This proved that the setup was functioning and it showed that the detector under investigation was indeed behaving as it was supposed to: The limited detection efficiency cannot be attributed to any kind of constriction effect. In fact, the detector showed a homogeneous distribution of the detection efficiency within the limits of our microscope. It became apparent, however, that due to the limited spatial resolution and the tightly packed meander lines we would not be able to extract much more physical information from these results.

In addition to the meander detectors, we also used the setup to measure the single photon response of short constrictions. Unfortunately the pulses emitted by these samples were not detectable by our commercial pulse counter which is why we started developing a dedicated one. We also started an experiment in Prof. Eyal Buks' group at the Technion university in Haifa, Israel. The primary goal was to reproduce the results achieved here in Karlsruhe with a different setup. But, as these experiments are done in a dilution refrigerator, we also started experiments at lower temperatures.

The last step in the original agenda was to decide from the results up to this point what aspect deserved more attention and design a new sample correspondingly. Since we did not find any weak links or similar defects in the existing detectors, we decided to focus our attention on the correlation between the local critical current of the wire and the detection efficiency at that point. As this could not be realized with the existing sample due to the tight packing of the lines, we decided to produce a sample which was an "unwound" version of the detector we had been using before. Then the idea was to combine the information from measurements in the single-photon- and the high-power regime and see if the results match the predictions from the theory outlined in Sec. 2.1.

4.1. Meander structures

The results presented in this section are from the sample NbN412/5 produced by the "Institut für Mikro- und Nanoelektronische Systeme". It is one of their standard meander structures with an NbN film thickness of $5nm$. The lines are $100nm$ in width and span an area of $4 \times 4\mu m^2$ with a filling factor of 50%.

We started out by measuring two of the most frequently quoted characteristics in this field: The temperature dependence of the resistance and the current-voltage (I-V)

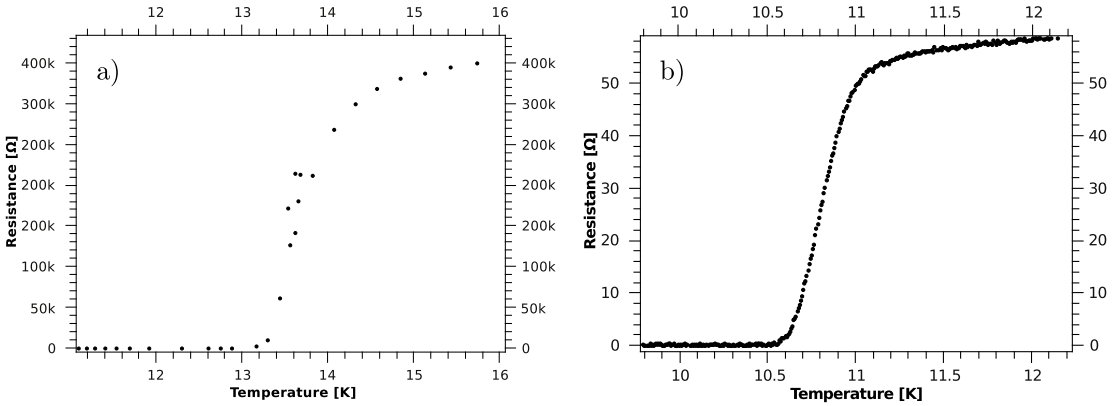

Figure 4.1.: $R(T)$ dependence of: a) The sample in a 4-point probe setup in liquid ^{4}He measured by the IMS. b) Shunted and in our cryogenic setup. One can see the different transition temperatures.

characteristics. The $R(T)$ dependence can be seen in Fig. 4.1a. Since the sample is shunted in our measurement, the curve seen in Fig. 4.1b is the temperature dependence of the system which represents the resistance of the shunt resistor above the critical temperature while the resistor gets "shunted" by the superconductor below this point. The different transition temperatures seen in Fig. 4.1 can probably at least partly be explained by different cooling mechanisms used in the two measurements.

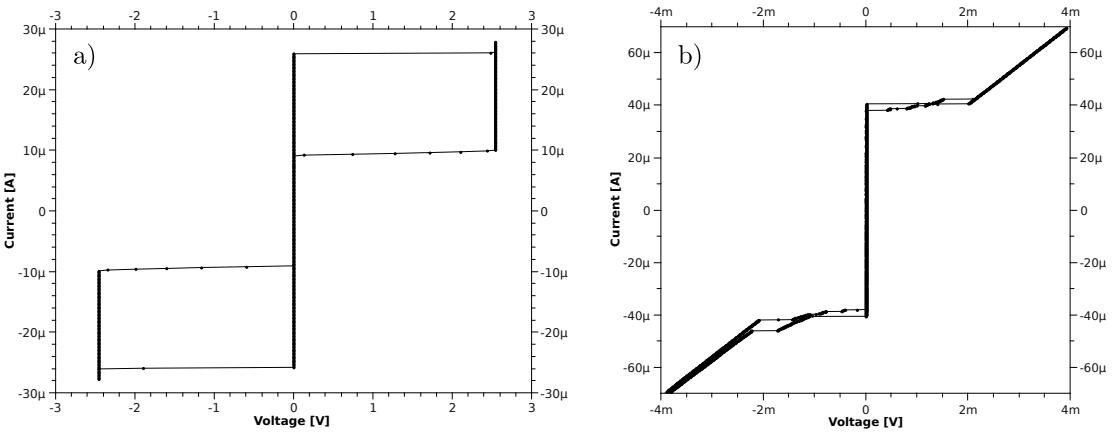

Figure 4.2.: Current-voltage characteristics. a) of the unshunted sample in liquid ^{4}He using a 4-point probe measurement scheme at the IMS. b) of the shunted detector embedded in our system measured with 4 probes behind the dc-path of the bias-tee. Switching states can be seen here.

The shunting also introduces some noteworthy effects within the current voltage char-

acteristics of the system which can be seen in Fig. 4.2b as compared to the resistance of the sample which is shown in Fig. 4.2a. The sample by itself will quickly overheat due to its large normal state resistance and the associated heat production when biased above the critical current. The large thermal hysteresis seen in Fig. 4.2a is a manifestation of this phenomenon since the temperature of the sample is increased so far by the ohmic losses, that the critical current is significantly lowered. One of the obvious things the shunt resistor does to the I-V characteristics of the system is to reduce this hysteresis. Once a normal domain develops inside the superconducting wire and the resistance of this normal section of the meander becomes comparable to or larger than the resistance of the shunt, one part[1] of the bias current will be redistributed to the shunt. This has a number of immediate effects:

1. The maximum total resistance of the system that the current sees $R_{\text{system}} = \frac{R_{\text{shunt}} \cdot R_{\text{sample}}}{R_{\text{shunt}} + R_{\text{sample}}}$ is always smaller than in the unshunted case. In comparison to the unshunted situation this means that in a current-biased situation the dissipated power due to ohmic losses $P_{\text{loss}} = R_{\text{system}} \times I_b^2$ is greatly reduced. This of course is not strictly true in our situation because it does not account for the dynamics introduced by the non-negligible inductances also present in the system.

2. The fraction of the power that gets dissipated on the resistor heats the resistor which is at some distance from the detector and therefore heats the sample less.

3. The electrothermal response of the system (see Sec. 2.1.6), which is responsible for the pulse development, also explains the relaxation oscillations present at bias currents above the critical current. If the current through the sample exceeds its overall critical current (the critical current of the weakest link in the bridge), a "pulse" will be triggered just as with the photon absorption. The processes described earlier will take place, the current through the sample will drop and rise again and eventually reach the critical current of the detector again which is when the whole process starts anew. As there are several sections with different critical currents in the detector, they each have their own switching state. If they are close together in terms of critical current they cannot be told apart but for some significantly different critical currents switching states can be distinguished. To model this we made a simplified SPICE simulation of which the output can be seen in Fig. 4.3.

The difference in the critical current seen in Fig. 4.2 cannot easily be explained by a higher temperature in our system since that would lead to a lower critical current. Measurements with our current source in liquid ^{4}He have also shown a different I_c than the IMS data which leads to the assumption that the difference could be caused by the setup. In any case, all measurements use the relative instead of the absolute bias current, which should eliminate that problem entirely.

At bias currents below I_c we now took traces of individual pulses two of which can be seen in Fig. 4.5. Since both amplifiers compared here showed a pulse rise time of about

[1] $I_{\text{shunt}} = \frac{R_{\text{sample}}}{R_{\text{shunt}} + R_{\text{sample}}} I_b$

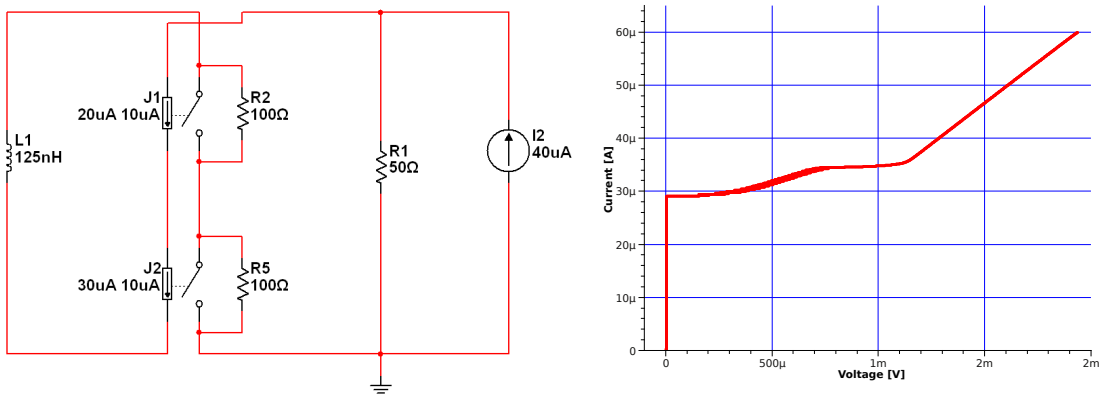

Figure 4.3.: A simplified SPICE model which reproduces the relaxation oscillations. Left: The circuit shows two thermally hysteretical domains of 100Ω each with a different critical current embedded in the model of the system. Right: The time-averaged voltage output when sweeping the current up. One can see the two transitions and a "stable" line in between which is actually the time-average of the first switching state.

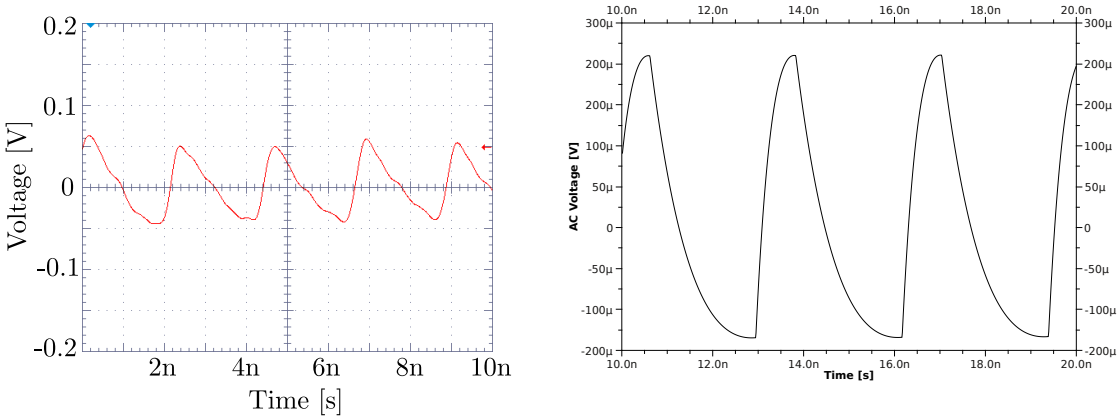

Figure 4.4.: Relaxation oscillations. Left: Real scope trace taken just above I_c. Right: AC-output of the simulation shown in 4.3

400ps (and the IMS amp has a much higher upper band) we concluded that the pulse rise time is not limited by the commercial amplifier. In these measurements, however, one can see a significant undershoot in the falling slope of the pulse measured with the faster IMS amplifier. Although we do not have exact data for the kinetic inductance of our sample we can estimate from the time constant of the falling slope $\tau_2 \approx 2.1ns$ and the value of the shunt resistance $R_0 \approx 68\Omega$ at 4.2K that it must be approximately

$L_K \approx 142nH$ which is comparable to the results from [28]. Furthermore reconstructing the original pulse amplitude to be $V_p \geq 700\mu V$. From that we can say that the current through the shunt at the peak of the original pulse was $I_{\text{shunt}} = \frac{V_p}{R_0} \geq 10\mu A$.

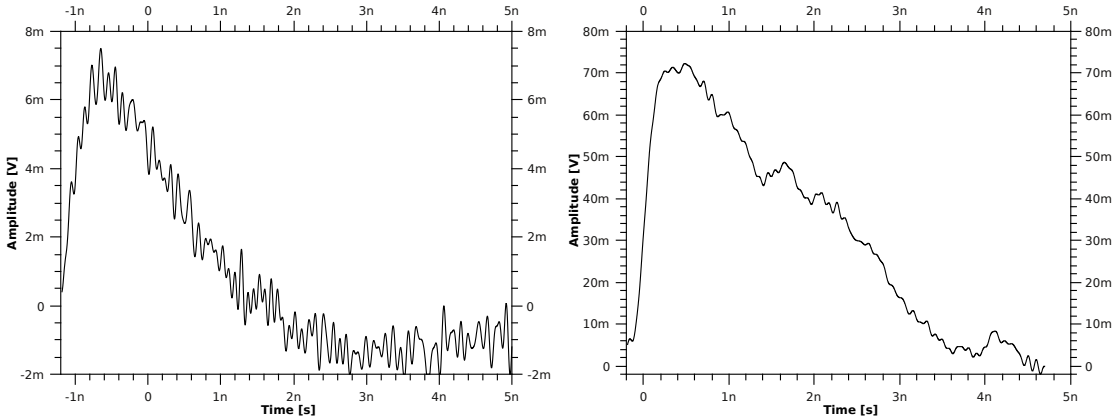

Figure 4.5.: Scope traces of pulses with room-temperature amplifiers. Left: Using a +22dB amplifier made by the IMS. Right: Using two cascaded +20dB 20MHz-3GHz commercial amplifiers with a combined gain of +40dB. Note that the amplitude of the original pulse must have been around $V = 700\mu V$. Note also that the "higher" noise level on the left is due to the different y-scale and the higher band of the IMS amp.

In the next step we moved on to counting pulses. Before presenting the data I have to mention that the data in this section is not completely correct since we recently found out that the pulse-counter used for this part of the experiment did not count all pulses correctly. We have proof to believe that especially for high repetition rates, short pulse-durations and low pulse amplitudes the measured number of pulses may vary significantly from the actual value. Unfortunately it is very hard to specify this any further since the magnitude of the error depends strongly on those factors. This does not matter so much for the images taken since in that case the the relative increase in the count rate is more important than the absolute number, but it certainly puts a question-mark behind all the data taken close to I_c where the count rates are high.

To begin with, we chose to measure the dark count rate of the detector in dependence of the bias current. To quantify the effect of the light coming from the room-temperature window, we made two series of dark count measurements. During the first one, the optical window in the innermost shield of the cryostat was taken out and replaced by a metallic lid. This way we could be sure that everything surrounding the sample was at a temperature of $T \approx 70K$ or less. For a second measurement we reinstalled the window and blocked the outer window using black cardboard and black cloth. This way all visible light was blocked from entering the cryostat but there was still some radiation from the room-temperature window that reached the sample. The result can be seen in Fig. 4.6. Interesting to compare with the other experiments is that at bias currents

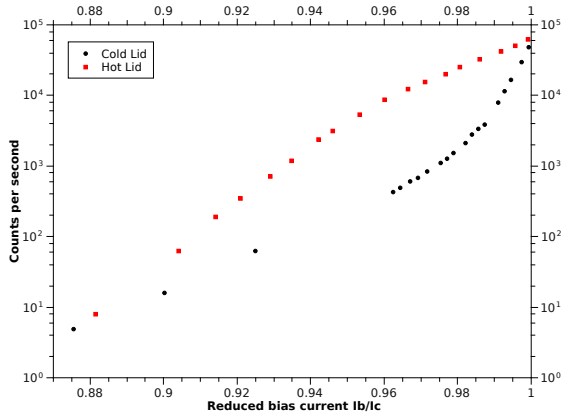

Figure 4.6.: Dark counts measured with and without a cold ($T \approx 70K$) lid.

lower than $I_b \approx 0.88 I_c$ the dark count rates remain unchanged if the cold lid is removed while at higher bias current the radiation coming from the (optically blocked) 300K parts seem to generate a considerable increase in count rates.

The next step was to combine laser-scanning and pulse-counting to create photon count maps in the single photon regime. For this reason we attenuated the laser down to a power of $P_l \approx 60pW$[2] which, given a wavelength of $\lambda_L = 635nm$, corresponds to an incoming photon rate of approximately

$$n_p = \frac{P_l}{E_p} = \frac{P_l \cdot \lambda_L}{h \cdot c} \approx 1.9 \cdot 10^8 s^{-1}$$

Considering the maximum count-rates are $n_{\mathrm{p,max}} > 10^7 s^{-1}$ the peak detection efficiency is always lower than 5%. Thus we can be sure that this laser power does not exceed the capabilities of the detector because $n_p \cdot DE < n_{\mathrm{p,max}}$.

The results of this laser scanning photon mapping can be seen in Fig. 4.7 and 4.8. We scanned the laser spot over the detector at different bias currents and with different resolutions. At first glance, one can immediately see a few characteristics, such as:

- The area and size of the response roughly depicts the square shape and dimensions of the detector. From this information we can conclude that:
  - The spot size is considerably smaller than the detector. If it were otherwise the shape of the response would be an image of the PSF and therefore round.
  - The response of the detector is not limited by constrictions. In that case there would only be a response from a small section of the detector similar to what has been observed in [9]

[2] The actual power can only be estimated since we could not measure it directly. Instead, we measured the unattenuated laser to have a power of 60nW and used a neutral density filter (nd=3) to reduce the transmitted power by three orders of magnitude.

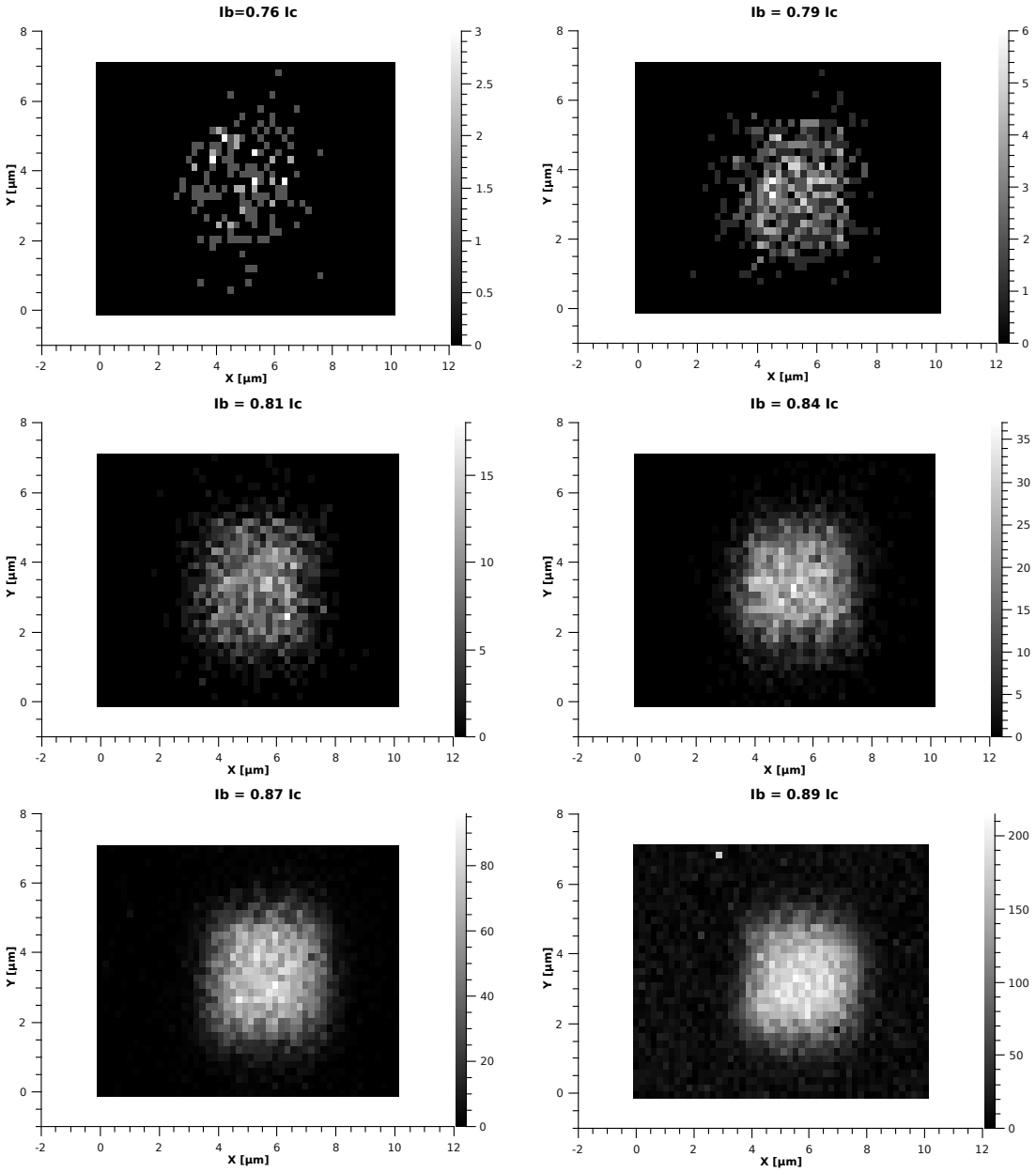

Figure 4.7.: Current-dependent series of photon count maps with a laser power of approximately $60pW$. An area of $10 \times 7\mu m^2$ was scanned using a step size of $200nm$. The color scale is in counts per 10ms. Each scan took approximately two minutes. One can see the increase in background noise (dark counts) between the two last images.

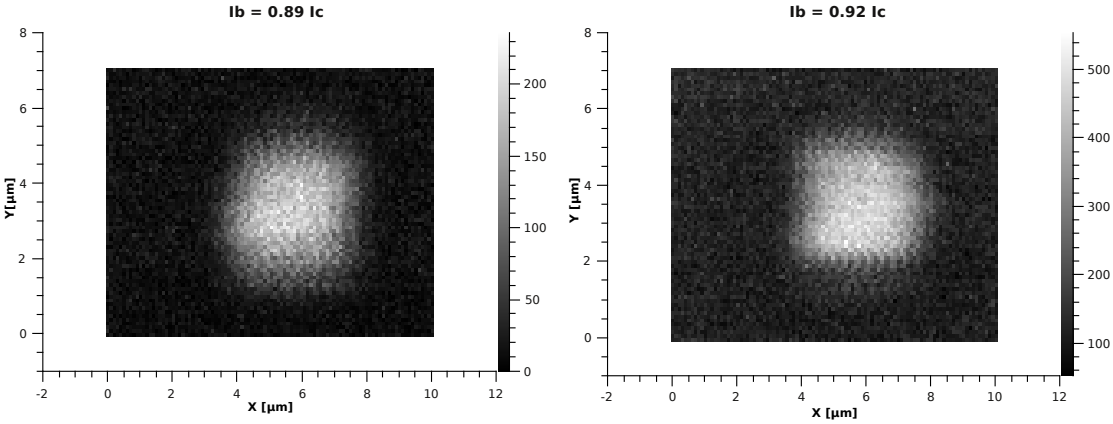

Figure 4.8.: Two higher-resolution photon count maps with a laser power of approximately 60pW. The color is in counts per 10ms. It took approximately 8 minutes to scan the area of $10 \times 7\mu m^2$ using a $100nm$ resolution.

- Qualitatively, dark counts (seen here as background noise) become visible only above a certain threshold current. This clearly shows that they stem from other sources than the laser. Since the numerical value of their appearance at $I_b \approx 0.89 I_c$ coincides with the value at which thermal radiation became visible in the dark count measurement of Fig. 4.6, it leads to the assumption that the background noise seen in images just above that threshold comes mainly from the source mentioned.

- In our setup, there is a "sweet-spot" in the bias current in which the signal is quite high and the signal-to-noise ratio low just below the threshold mentioned in the last bullet.

Applying the half amplitude criterion mentioned in Sec. 2.2.1 to one of these scans, one can see that the active area seems to be more like $3.6 \times 3.4\mu m^2$. Although one could argue that in this case the conditions for the criterion are not fulfilled (and given the numbers, they are not), it still provides a reasonable idea of the actual dimensions especially considering that we do not expect the whole area to be sensitive but only about $3.7 \times 3.6\mu m^2$. The remaining $0.1\mu m - 0.2\mu m$ are within the accuracy of our experimental setup.

As a last stage in this experiment, we had planned to make measurements in the bolometric regime. These were made with the same setup used for the single photon measurements and so the modulation frequency had to be chosen high enough to be above the lower cutoff frequency of the bias-tee. The main goal was to show that this kind of measurement produces comparable results and can be carried out without reconnecting the sample. In future experiments these two measurements can be used in conjunction and provide information about the critical current dependence of the detection efficiency.

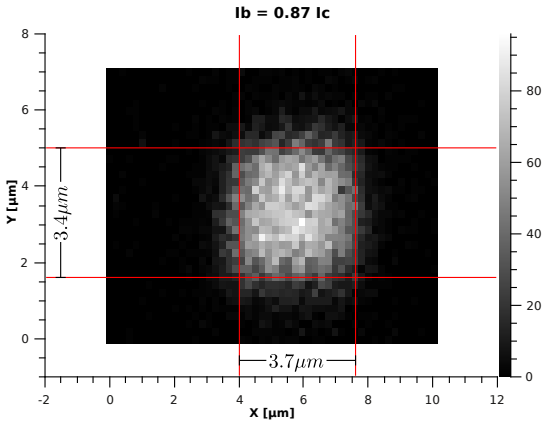

Figure 4.9.: Photon map with applied half amplitude criterion to show the assumed position of the detector edges.

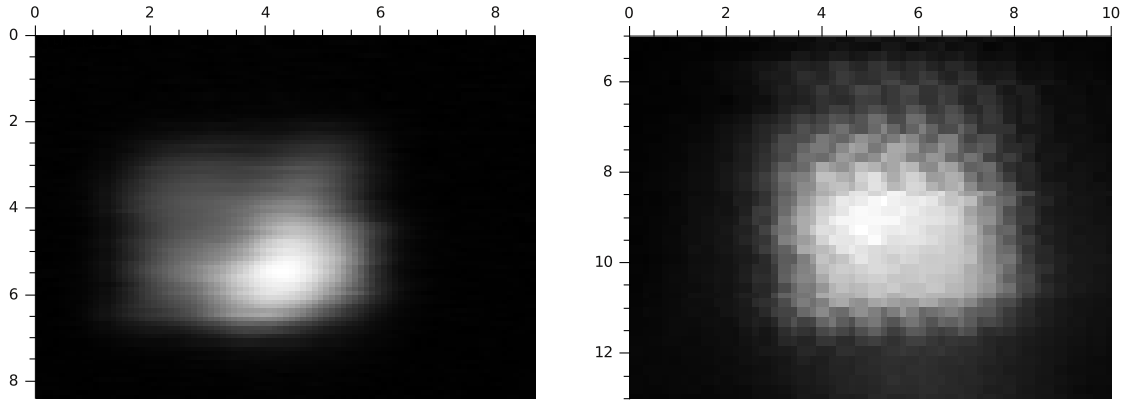

Figure 4.10.: Comparison of resistive measurement (left) and photon count map (right). The inhomogeneous signal probably results from dirt on the sample.

Using this sample, however, this is not possible because the correspondence between photo-response and critical current density can only be established for scans along the current flow direction and the meander is obviously a structure unsuited for this task. Fig. 4.10 shows that these two measurements are comparable and can be performed during the same cool-down cycle. During these measurements we also observed a region of higher sensitivity in one corner. This was most probably just some residue on the sample since it never appeared in any measurements before or afterwards. Interestingly, the area with the highest photo-response in the resistive picture seems to correspond to the area of the lowest detection efficiency in the photon count map.

In summary we have shown that our technique of single photon mapping works well and provides information beyond the measurements of past experiments.

4.2. Long bridge structures

Following the road-map outlined at the beginning of this chapter, the next step after completing the spatially resolved measurements of Sec. 4.1 was to design a sample for further measurements from the results gained so far. Since we did not find any obvious geometrical peculiarities or defects on the meander detectors, which would have justified a closer look at the geometry, we decided to focus instead on the correlation between the local superconducting critical current of the wire and the corresponding detection efficiency.

In our opinion a good way to realize this is to use an "unwound" version of the meander detector. This sample was designed as a single bridge structure with a width of $w = 100nm$ and a length of $l = 80\mu m$ patterned onto a $d = 5nm$ thick NbN film on sapphire. The idea behind this geometry is to make one-dimensional scans along the bridge using both resistive and single-photon measurements. That way, we can correlate the results and find out if the dependence of the local DE on the local critical current of a cross-section matches the predictions of the theory outlined in Sec. 2.1.

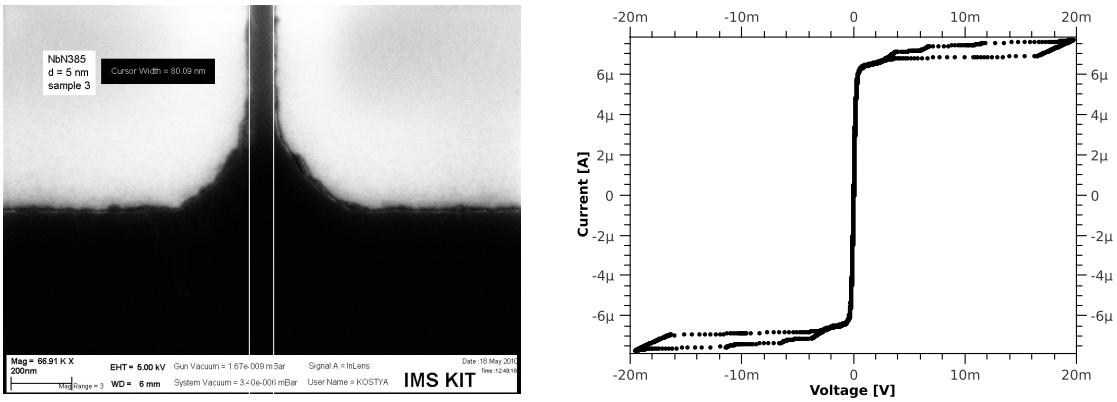

Figure 4.11.: Long bridge structures. Left: Electron microscope image of one of the bridges. Right: I-V characteristics at 4.2K measured in the our cryostat with the window blocked at room temperature.

At first glance, a single bridge may seem like a rather boring sample to study because variations in the critical current of the wire are needed to find any form of dependence. From experience, however, we know that even in nicely patterned strips the grainy structure of NbN thin-films on sapphire provides enough local variations and thus contrast. Another proof of this are the many steps in the I-V characteristics seen in Fig. 4.11.

Like the meander shaped detectors, the bridges were produced by the IMS and so far only their DC-characteristics have been measured. Future experiments on them will hopefully provide a closer insight into the mechanisms of photon detection.

4.3. Short constrictions

As I have pointed out before, using the meander as a geometry for an SNSPD is nothing more than the attempt to make a detector which covers a square area. The long bridges mentioned in Sec. 4.2 are just one example of a differently shaped detector. While these may be interesting to investigate the dependence of the DE on the critical current, many practical applications require square pixels and therefore square[3] detectors. Another approach to create a square detector would be to use just one approximately square-shaped short piece of the nanowire as a detector.

Although the physical processes undoubtedly remain the same, one would expect pulses to be much shorter due to the lower kinetic inductance. We measured the pulse response of a $0.3 \times 0.3\mu m^2$ bridge which is a short constriction in a NbN film similar to the one from which the meander was patterned. As a quick approximation we used the normal state resistance and known kinetic inductance of the meander[4] to estimate the kinetic inductance of the bridge:

$$L_K = \frac{R_{300,\text{bridge}}}{R_{300,\text{meander}}} L_{k,\text{meander}} \approx 0.7nH$$

This would not only mean that the inductance of the bridge is comparable to or even smaller than the inductance of other components like the bond wires but also that the rise- and fall-times of the pulses should be only a few picoseconds long. Looking at the oscilloscope, however, it quickly became apparent that they were indeed visible and that the slopes were much longer than expected. An example can be seen in Fig. 4.12. Whether this has to be attributed to parasitic inductances in the setup or simply bandwidth limitations of the hardware cannot finally be stated.

This fact allowed us to perform the count-rate measurements from the previous experiments on the short constrictions. As the pulses were too short to be detected by our commercial pulse-counter, we had to resort to taking oscilloscope traces instead. The high sampling rate, needed to reliably find all the pulses by software, limited the time of each trace to $3.2ms$. The current-dependence of the count rates seen in Fig. 4.13 shows a remarkable similarity to the measurements on the meander detectors and proves that they do, in principle, work as detectors although no definite numbers on their detection efficiency can be given at this point.

The small size of the constriction explains why we did not attempt to image them as we did with the other detectors.

[3] At least they should fit within a square without leaving too much of the square area uncovered (i.e. circular detectors).

[4] According to [11].

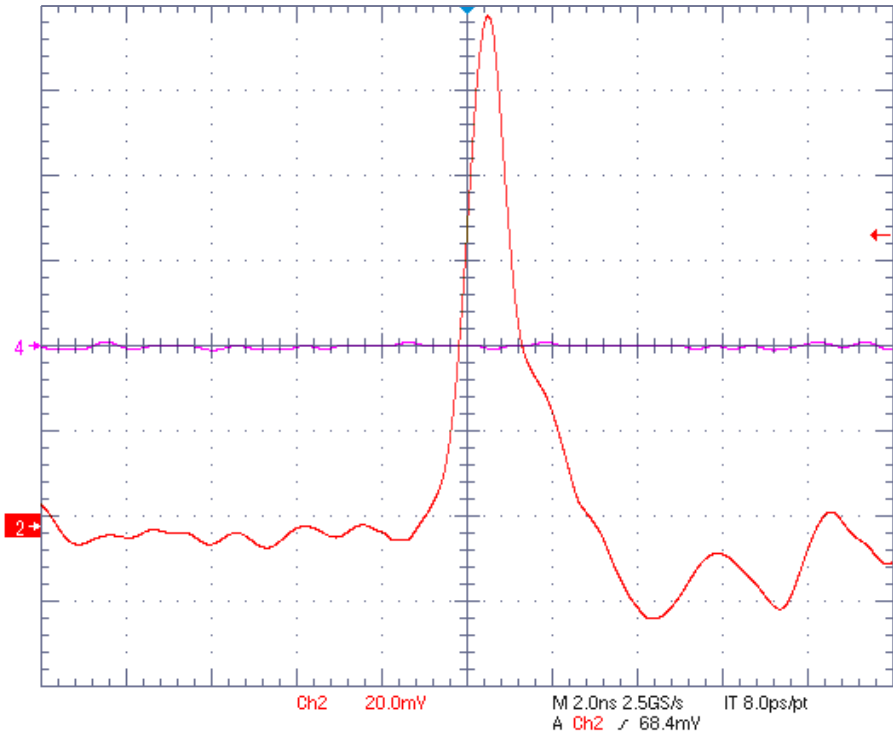

Figure 4.12.: Oscilloscope trace of a pulse from a short constriction after +40dB amplification at 6.35K.

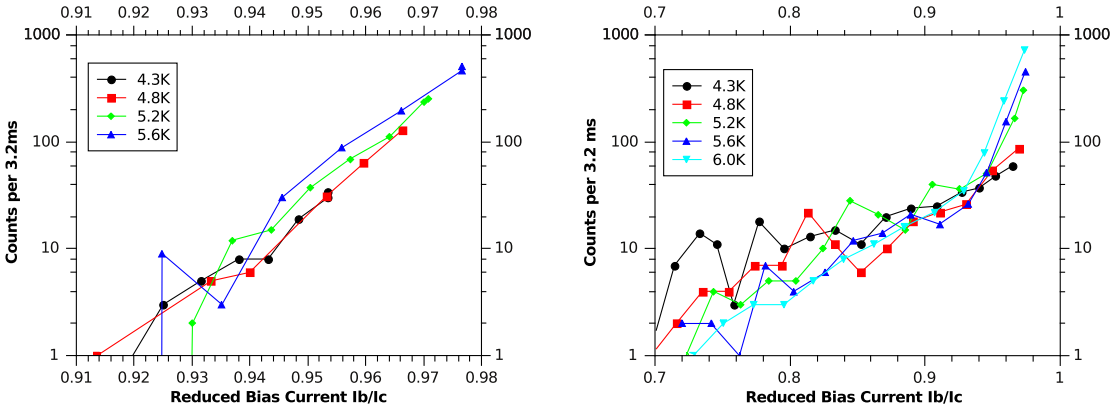

Figure 4.13.: Current-dependent count-rates of the short constrictions. Left: With the optical window blocked. Right: With defocused laser light.

4.4. The experiment at Technion

The experiment conducted at the *Nano-Electronics Research Center* at *Technion University, Haifa, Israel* mainly aimed at verifying the existing experiments using their very different experimental setup which was described in Sec. 3.6. As it was conducted inside a dilution refrigerator, all the preparations and the cooldown took significantly longer than in our system but it offered us the opportunity to acquire data in a temperature range down to 100mK.

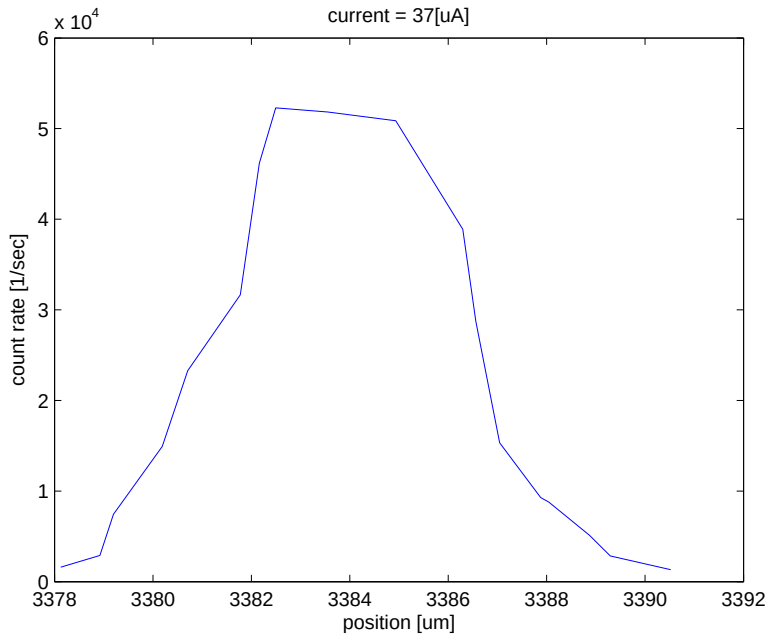

Figure 4.14.: 1-D Step scan along the x-axis of the system.

Our first steps were line-step-scans along the x- and y- axis of the system by leaving one axis alone and moving the other one by a fixed number of steps for every data point. Figure 4.14 shows such a scan. Since the sample is rotated 45°against the scanning direction, there is no way of knowing precisely how wide the scanned section of the detector really is. Assuming we managed to scan the central part as we intended, this length would be $l = \sqrt{2}4\mu m \approx 5.66\mu m$. Since in this experiment we have even less information about the precise shape of the PSF we can only assume that its waist is much smaller than the detector dimensions. In that case the line-scan results are at least reasonable.

From these measurements it quickly became apparent that imaging the way we do it in our system would not be easily possible here. The three methods of scanning available in this setup each had their own problems:

- The **step-scans** could not be extended to work as two-dimensional scans because the step-widths are usually different for the forward- and backward-motion. And although one could use the position read-out value to find the initial position again[5], the lines of the scan would still be shifted.

- Although the **absolute scan** would be the easiest method to implement since it uses the internal positioning algorithm of the piezo-controller, it is not usable for scanning since it is *very* slow.

- As mentioned earlier, the positioners also have a limited scanning range which, according to the manual, should be roughly $0.8\mu m \times 0.8\mu m$ at $4.2K$. In this range they should be able to move smoothly and therefore work nicely as scanners. One could then take several **smooth scans** and stitch them together to get a full picture. Unfortunately, however, according to the position read-out, the effective scanning range was much smaller than that which would mean a very high number of smooth-scans to cover the whole detector area..

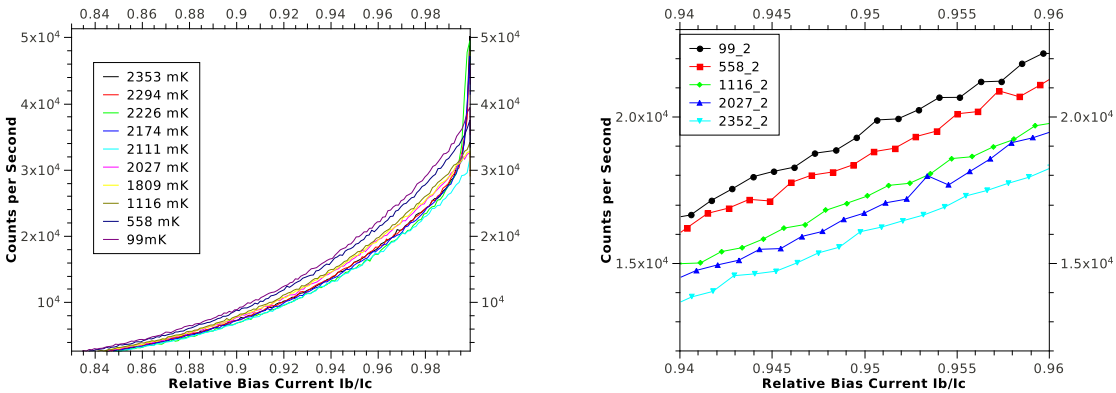

Figure 4.15.: Count rates in the illuminated sample. Left: Current dependence at different temperatures. Right: Close-up of the current region close to $I_b = 0.95 \cdot I_c$

Given these restrictions, we decided to focus on the low temperature behavior of the detectors instead since there is, to our knowledge, no published data below 2K. For this purpose, the sample was cooled down to a temperature of 100mK, the pumps were turned off and the system was left to warm up freely. At 33 points between 100mK and 2.3K measurements of the samples I-V characteristics as well as its current-dependent count rates - both with and without illumination - were taken. Since the fiber had to be moved away from the sample[6] to guarantee an equal illumination for all temperatures, we cannot provide absolute detection efficiencies. Figure 4.15 shows current dependent

[5] which would also make the scan significantly slower
[6] The fiber position shifts in relation to the sample position during temperature changes

count rates at different temperatures. At bias currents of $Ib = 0.95I_c$ one can observe a general trend of rising detection efficiencies towards lower temperatures. Figure 4.17 shows, however, that this is just a trend and fluctuations in the values are quite large.

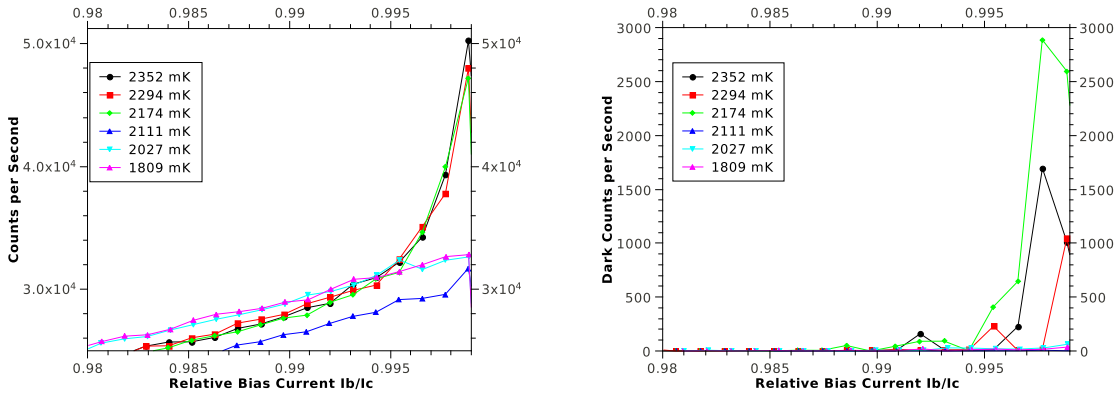

Figure 4.16.: Count rates for I_b close to I_c. Left: With illumination Right: Without illumination

From this data one can see an unexpected, temperature-dependent, qualitative change in the behavior for I_b close to I_c which is highlighted on the left side of Fig. 4.16. In the illuminated case, the current-dependent count rates usually show a sharp upturn close to I_c (see for example [10]). This is also the case in our experiment for curves taken with $T \leq 2.14K$. For lower temperatures, however, this upturn seemed to disappear. As this upturn is usually attributed to an increase in dark counts close to I_c, a look at their current dependence (Fig. 4.16 right) shows a similar behavior. While the maximum dark count rates measured just below a threshold temperature $T_t \approx 2.1K$ never rise above a few tens per second, they never drop below a few thousands above that temperature. These findings seem to contradict previous results [12] in which the authors found the dark count rates to decrease quasi-exponentially with the temperature down to $T = 1.5K$. We also observed that below T_t the critical current of the sample seems to depend on the power of the illumination even at power levels as low as the ones used in that experiment, which is not observable for higher temperatures.

Figure 4.17 summarizes our findings by showing relative changes in dark count rates and total count rates at fixed relative bias currents. At this point we have no definite explanation for the rather abrupt change in dark count rates at T_t. The small temperature interval and the magnitude of the change suggest that there is some sort of transition involved, or some mechanism freezes out. The fact that T_t is very close to the ^{4}He lambda point ($2.17K$) could be a hint at possible explanations.

Future experiments will have to show whether this effect could indeed be caused by a superfluid ^{4}He-film on the sample, thermal coupling to the substrate, some intrinsic effect responsible for the dark counts or just some other part of the setup. From the technological side, the result - unchanged detection efficiency with almost vanishing

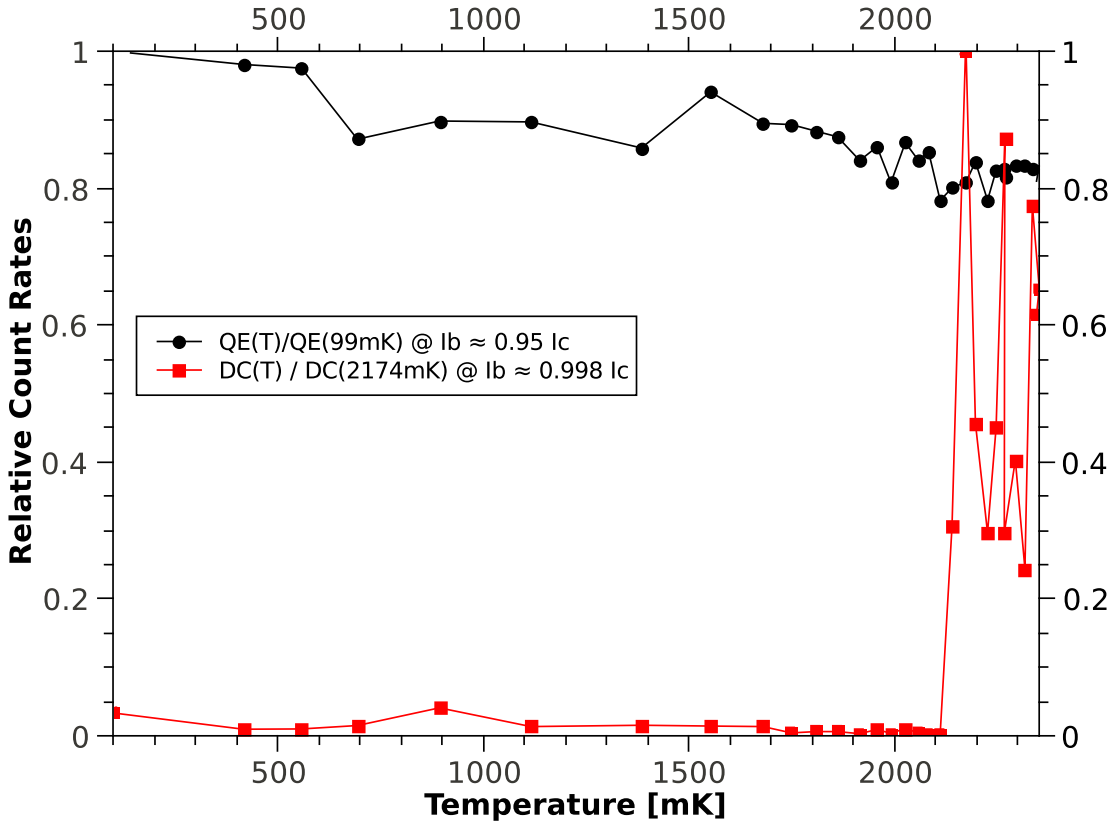

Figure 4.17.: Relative count rates. Black: Temperature dependence of relative detection efficiency at $I_b \approx 0.95 \cdot I_c$. Reference value is DE at 99mK. Red: Temperature dependence of relative dark count rate at $I_b \approx 0.998 \cdot I_c$. Reference is the dark count rate at 2174mK

dark count rates - is in any case a highly desirable state of operation for a single photon detector.

4.5. Outlook

The results presented in this chapter clearly show that there is still a wide margin for improvements to be made from the technological point of view as well as aspects to be understood from the physical side.

Continuing the research outlined throughout this thesis will definitely include resuming the measurements on the long bridge structures that were part of the original agenda and started in Sec. 4.2. Information gained from this may - in the future - provide a better understanding of the influence of material effects, like the granular structure of NbN on sapphire, on the local detection efficiency and serve as a data basis to verify the refined hot-spot model.

We also believe that the experiment on the short constrictions deserves a closer look. Although we do not expect to find anything new from the physical side, a better characterization of these devices including measurements of their absolute detection efficiency and dark count rates may provide interesting information when thinking about future detector geometries. In the future our home-made pulse counter will enable us to measure them with a much better statistic requiring very little time.

Finally, we think that the experiment at low temperatures conducted at Technion deserves to be continued. The data gathered so far seems to show that the detector can be operated in a mode, in which the ratio of photon-induced counts to dark counts is greatly improved. Although at this time we have no clear evidence from which to decide what causes this phenomenon, the detector itself or some external influence, we believe that future experiments will provide this information. At this point, theories explaining the measurements seem to raise more questions than they answer but this just underlines the need for more data and potentially a closer investigation of the matter.

A. Appendix

A.1. Development of a fast pulse counter

It has been mentioned earlier that we felt the need to develop a device capable of counting short pulses to avoid the purchase of expensive hardware. In this chapter I will describe the development process and the preliminary results as this is still work in progress. The work presented in this chapter has been performed in collaboration with Roland Jehle and his team from the electronics workshop of our institute.

A.1.1. Requirements and feasibility

To be of any use for the experiment, the counter has to meet some requirements. Although these were carefully chosen in the context of the current conditions, they were only the minimal requirements to potentially make the device usable in future experiments:

Timing: From the experimental side, these are probably the most obvious restriction. Our goal was to build a device capable of counting pulses as short as $1ns$. Additionally, propagation delays in the relevant parts were to be at most $5ns$. These numbers were chosen to allow experiments on the aforementioned "short constriction" type samples.

Sensitivity: Typically, pulses in our setup are a few tens of millivolts in amplitude. We wanted the counter to be able to count such signals without the need of any additional amplification.

Usability and connectivity: The device was to have front-end controls and a display as well as a computer interface. The latter condition had to be met to be able to use the device for computer-controlled imaging, while the first requirement was simply a question of usability.

Counter width: Considering the approximate maximum number of pulses during the measurement time we aimed at, we concluded that we would at least need a 24-bit wide counter and a mechanism to detect possible overflows.

Cost: Apart from all the technical aspects, the whole development only makes sense if the end-product is significantly cheaper than a commercial device fulfilling the same criteria. We aimed at an end product costing no more than a few hundred euros.

The question remained if such a device can be developed with the means and know-how available to us in a reasonable timespan. After some research and discussion we came to the conclusion that it is possible provided that one uses the correct hardware.

A.1.2. Choice of hardware

First of all we decided to split up the electronics into two parts: One dedicated to do the actual counting and one to do the rest. This meant reducing the speed requirements primarily to the first circuit. The choice of what kind of electronics to take for this task quickly fell on *Emitter Coupled Logic (ECL)* elements[1] as they are the fastest ones available. The reason for this is that in contrast to other logic families, the bipolar transistors are never driven into saturation which also reduces the base-collector capacitance responsible for the Miller-effect. This is in part achieved by the small difference of the logic levels. While classical LVTTL levels switch between 0V and 3.3V, LVPECL elements use 1.6V as a low- and 2.4V as a high level. Furthermore, the main part of the logic gates are similar to the classical differential amplifier shown as the highlighted part in Fig. A.1. The symmetric layout explains why the power consumption of the devices is independent of their state, in contrast to other logic families where the devices consume more power as they switch than in idle state. While this relatively high power consumption is a problem for close integration it does not have any negative impact on our application. In fact the constant power consumption also means less stress on the power supply and a constant heat development which will, after some stabilization, lead to constant operating conditions.

Having decided on the logic-family, we still had to think of an appropriate way to use the available ICs to count pulses. Lacking any experience, we chose the simplest approach: The signal input is connected to a voltage comparator[2] which emits an LVPECL high signal if the input exceeds a threshold voltage. With a minimum pulse width of $200ps$ and a propagation delay of $250ps$ it seemed to be an adequate choice. The switching voltage uncertainty of $\pm 5mV$ is also within the limits and it can be set to have a switching hysteresis. Although there are faster models, we chose this particular device because the faster devices require a very high slew-rate of the input signal while this one "only" needs $5\frac{V}{ms}$. The LVPECL output of the comparator is connected to the clock input of a synchronous 8-bit binary up counter[3]. With an minimum clock-pulse width of $300ps - 550ps$ and a propagation delay of $500ps$ it also meets the set timing requirements. In the final application two of these counters are cascaded.

The hardware for all the other components like the readout, computer connection and front-end does not have to be that fast. To implement these high-level functions, there were two options: Using a processor or using an FPGA. For a number of reasons we decided on using an FPGA development board[4]. This, however, created another

[1] In fact we use so-called *Low Voltage Positive Emitter Coupled Logic (PECL)* elements as these are a bit easier to interface with the other electronics.
[2] Analog Devices ADCMP567
[3] ON Semiconductor MC10EP016
[4] Terasic DE1 board with an Altera Cyclone II FPGA

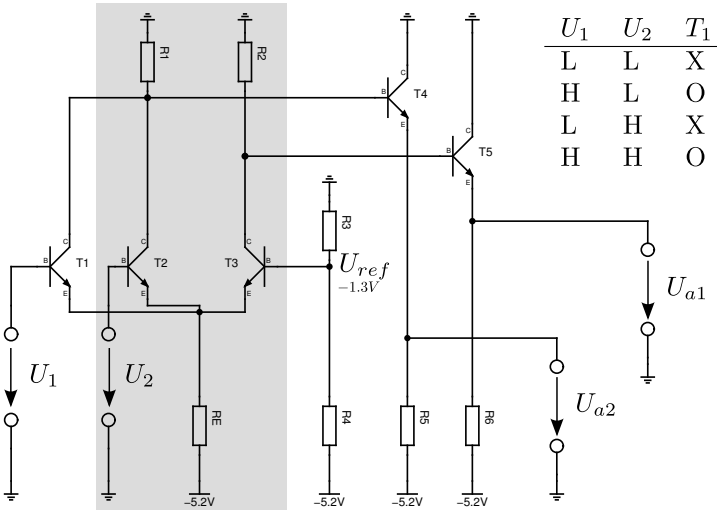

U_1	U_2	T_1	T_2	T_3	T_4	T_5	U_{a1}	U_{a2}
L	L	X	X	O	O	X	L	H
H	L	O	X	X	X	O	H	L
L	H	X	O	X	X	O	H	L
H	H	O	O	X	X	O	H	L

H: $U = -0.9V$
L: $U = -1.75V$
O: Transistor open
X: Transistor closed

Figure A.1.: An ECL OR/NOR gate with logic table. $U_{a1} = U_1 \vee U_2$. $U_{a2} = \overline{U_1 \vee U_2}$. The highlighted section can be seen as a long-tailed-pair differential amplifier where U_{R2} is the amplified output of U_2. Note that in any logical state at least one of the transistors $T1 \vee T2$ or $T3$ are open which effectively makes R_E work as a current source and explains the constant power consumption.

problem: As the logic levels of FPGAs and processors are typically LVTTL, we had to build an interface to translate between LVTTL and LVPECL.

A.1.3. Design and road map

Putting it all together we decided first to build a very crude "proof of concept" device only consisting of the counting electronics which would be read out by a scope. In case of success, the plan was to develop a fully functional prototype lacking only a housing and the connectivity and finally to combine all the elements mentioned above according to the schematic shown in Fig. A.2 into a complete application.

The work-flow of the device was planned to be:

- The user turns on the device and connects input coaxial cable and RS232 serial interface cable.
- The FPGA reads old settings like "measurement time" or "continuous operation" from the onboard flash memory into registers.
- The user can change settings either manually via the front-end LCD-display and buttons or via the RS232-connection. He can also adjust the threshold voltage using the potentiometer and voltage-display mounted on the front-panel.
- The user starts a measurement either by pushing a front-end button or by giving the appropriate command from the RS232-interface.

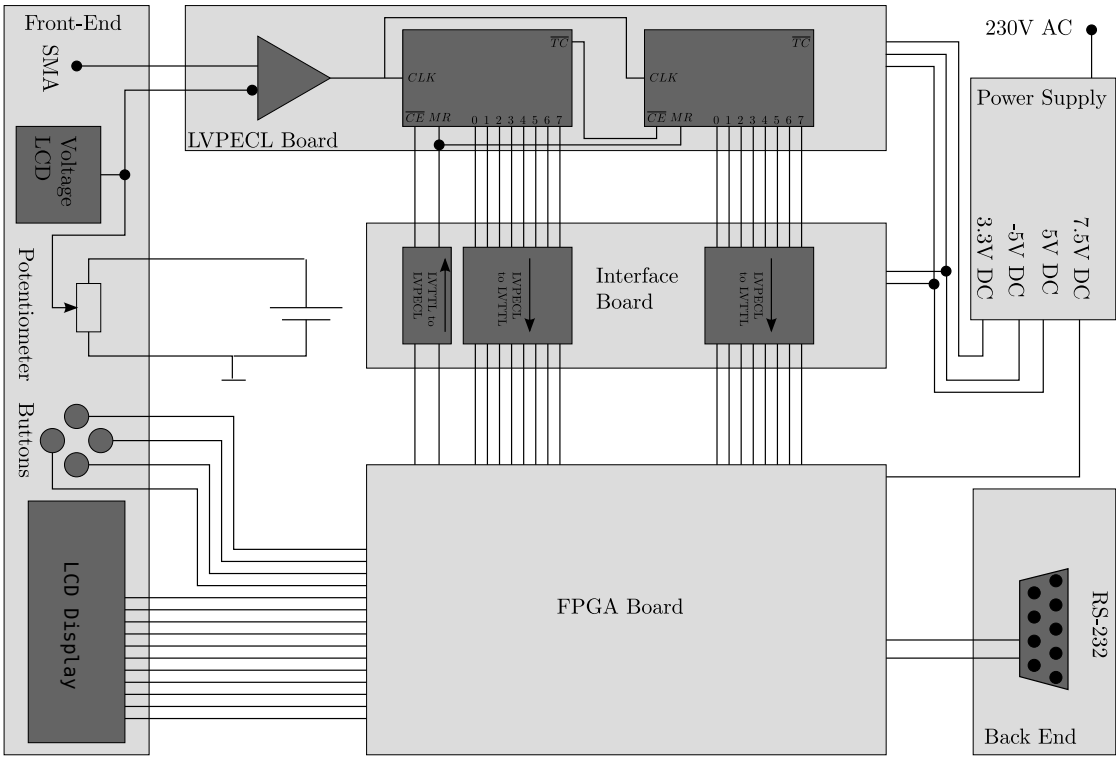

Figure A.2.: Schematic layout of the pulse counter.

- The FPGA clears the counter by sending an MR (master reset) signal.

- The FPGA sends a CE (chip enable) signal that has the length of the measurement time. During that time, the ECL board counts incoming pulses which exceed the threshold voltage. If the number of pulses during that period exceeds the 16 bit, the FPGA uses the *Most Significant Bit (MSB)* to clock another internal 8 bit which increases the total width of the counter to 24 bit.

- The result is displayed on the front-end LCD-display. If the measurement has been started via the RS232-connection, the result is also sent back that way.

- If the continuous mode has been chosen, another measurement is started directly. In any other case the user can now again change the settings or start a new measurement.

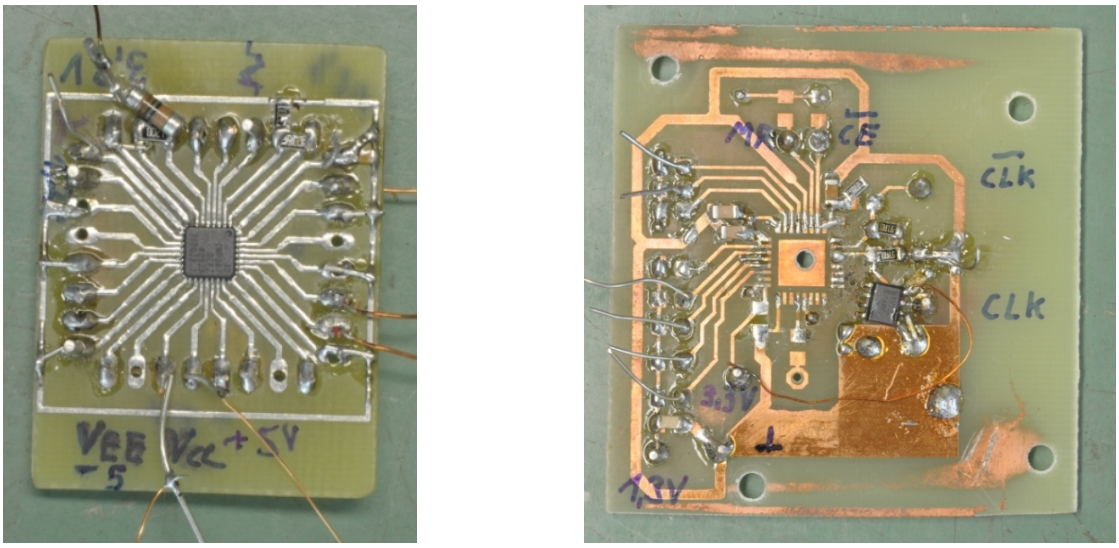

Figure A.3.: The "proof of concept" stage. Left: The comparator on its PCB. Right: The counter PCB from which the IC has already been removed.

A.1.4. Development stages

Proof of concept

In our first attempt we simply mounted the comparator and one counter on two different *printed circuit boards (PCB)* and connected them to each other and to the pulse source[5] via normal wires. The two boards can be seen in Fig. A.3. The output bits were connected to a scope and bursts of a few pulses were sent to the counter. This worked well for low frequencies but failed, predictably, for shorter pulses and high repetition rates since neither the input nor the internal connections were matched and the wires are not suitable to carry high frequency signals. Having realized this, we declared the test successful and decided to move on to the prototype stage.

Prototype

This time we made one PCB carrying both the comparator and the counter which was also fitted with an SMB connector for the signal input. A first interface board was made for the communication between FPGA and LVPECL electronics. We wrote a simple AHDL[6] application for the testing process which used the buttons and seven-segment display on the FPGA board to start measurements and display the results. This version also used 8 bit on the FPGA to extend the counter width to 16 bit and the measurement time was fixed to $1s$. The complete setup can be seen in Fig A.4.

[5] An Agilent 81110A pulse pattern generator
[6] Altera Hardware Description Language

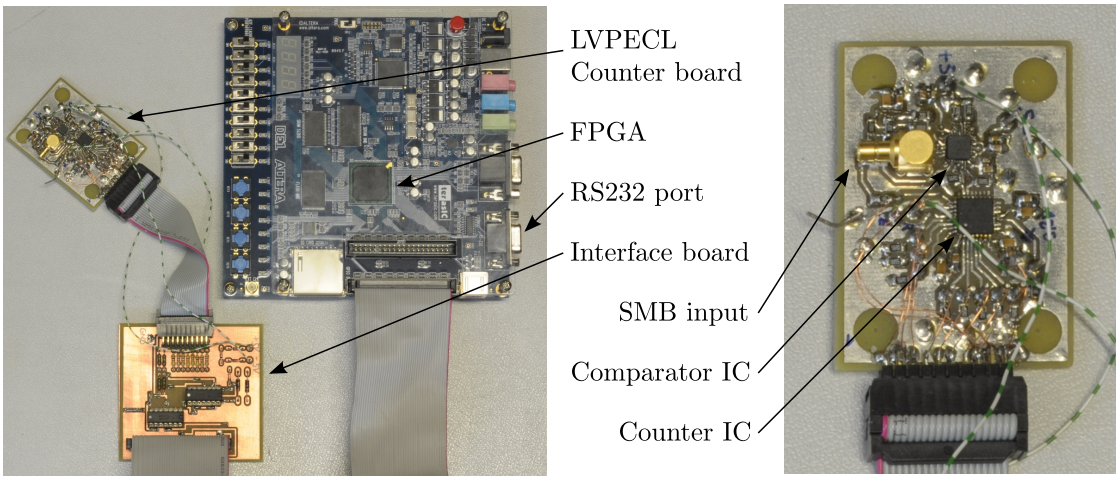

Figure A.4.: The prototype stage. Left: All three boards connected to each other. Notice the 7-segment displays and buttons on the FPGA-board which were used to start measurements and display results. Right: Close-up of the LVPECL counter board.

The tests conducted on this prototype were successful by all standards. The counter correctly counted bursts of 1 to $2^{16} - 1$ pulses. The minimal pulse-width however was limited by the pulse pattern generator to $1.5ns$.

Final device

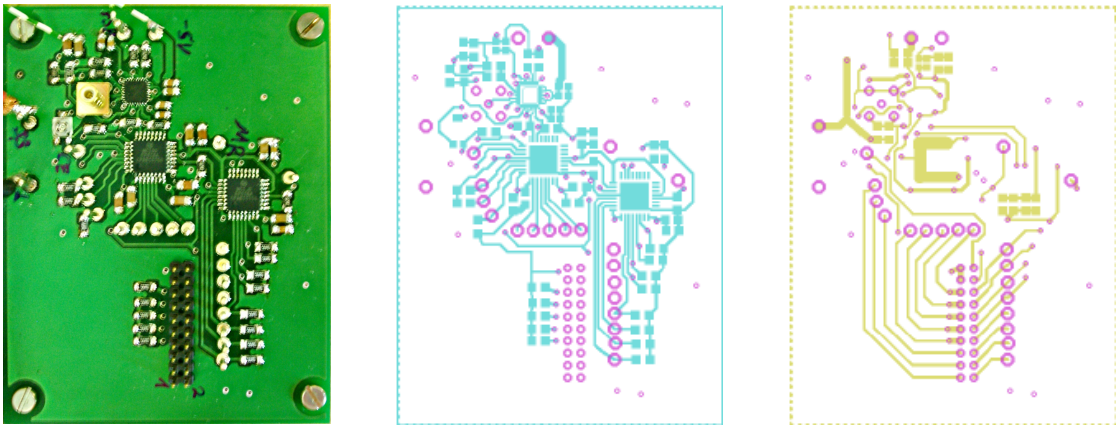

Figure A.5.: Final LVPECL board: Left: Image of the top side. Center: Board layout of the top side. Right: Board layout of the bottom side.

As the final version is still work in progress, I can only give preliminary results. The LVPECL-board with two cascaded counters (see Fig. A.5) and the interface-board with 16 channels have been tested with the prototype test-setup and work. The RS232 computer connection already works and allows the user to start a measurement and receive the result from the computer although right now it still lacks the possibility of changing settings this way. The front-end controls are being worked on as well as the housing and power supply.

A.1.5. Conclusion

In summary, we have shown that it is possible to build a sub-ns pulse counter fulfilling the criteria mentioned. From the datasheet values we can estimate the minimum countable pulse width to be approximately $550ps$ and the total propagation delay from the signal input to all outputs to be smaller than $3ns$. Thorough tests of the final version will have to show its actual performance. The total cost of the final device can only be estimated at this point but should not exceed 400€.

A.2. Development of a scanning microscopy application

When setting up new experiments, scientists are usually faced with the task of data acquisition. Nowadays most experiments use computer software to control and read out the instruments used in the experiment and writing small pieces of software has become a part of almost every scientist's job. This, however, creates a problem: Since, understandably, scientists are in general more focused on their research than on creating software to conduct it, they will, in most cases, choose the easiest and fastest way to create a working software. Today there are some applications like MATLAB or LabView that allow researchers to quickly create small applications capable of controlling complex scientific experiments. Their main advantage lies in the ease of use: They usually have a large set of libraries which allow the programmer to quickly connect to various kinds of instruments without having to concern himself with actual hardware communication. The problem I mentioned usually arises when those software projects become larger and more complex than initially intended. With increasing functionality, these software projects tend to become so complicated and mangled that nobody but the original author has any chance of updating or extending them.

At the beginning of this experiment I found myself in this exact situation. For the LSM, people were using a LabView software created and maintained by someone outside the institute which made it impossible to adapt the setup to its new needs in the given time. Consequently, we decided on creating a new software.

A.2.1. Requirements

To begin with, we defined a list of requirements to judge if the available resources[7] were sufficient to realize the project.

Generality. Without limiting the functionality, we wanted to keep the software as general as possible. In particular this means that it should not be limited to work with a certain kind of hard- and software. The limitation should be the work-flow of the application which explains why the result is rather a scanning microscopy software than a laser scanning microscopy software.

Functionality. As this is of course the most important requirement of all, it encompasses a great number of tasks which I do not want to state in detail. Instead I will just give the most important ones.

- Control the data-acquisition process by:
  - controlling the probe (laser spot) position.
  - reading out instruments to get the response signal
  - reading and storing additional information from other devices (i.e. temperature,...)

[7] In this case mainly: time

- Offer the user a *"Graphical User Interface" (GUI)* to control the scanning process and see the results as well as other necessary information.
- Store the images and allow the user to save them together with the meta-information[8].
- Allow the user to make series of scans with changing parameters.

Work-flow and intuitive handling. Many of the scientific applications one can find in a lab seem to be created following the approach of fitting the maximum number of "buttons and knobs" onto the screen. While this may indeed be useful for someone who uses that software on an everyday basis, experience shows that it is extremely irritating for everyone else. For this reason, a new scanning application should primarily display the basic controls and settings and hide the other ones so that the user only needs to see them when he actually wants to change something. Ideally, the user interface should also be designed after the typical work-flow of the user rather than the internal structure of the application.

Stability. One of the typical problems with software that has to access hardware is stability. Compared to pure software applications, the implementation of hardware often leads to undefined states or memory problems which can lead to slowdowns, crashes and in the worst case the loss of measurement data. There are techniques to prevent this and any good application should try to utilize them.

Performance. Another drawback inherent to high-level design solutions like LabView and indeed to most scripting languages as well is the comparatively poor performance. This is simply a consequence of the immense overhead they carry and abstraction layers they introduce. A scanning-process, however, should be fast and ideally not require high-end machinery.

Extensibility. The software should in principle be extensible by other people to implement new features and support new hardware. Although this is always problematic, one can at least try to work in that direction by defining a comprehensive structure before starting the actual programming and documenting the code.

A.2.2. Design and concept

When it comes to the actual software design, the first question is usually what programming language or framework should be used. As most of the programmers have a certain tendency to use what they personally like most and know best (I do not want to exclude myself), this is never a completely consequent decision. In my case, the choice fell on C++ using the QT framework. While this combination is certainly not the best choice if one aims at extensibility since it requires a relatively high programming skill level, it is certainly a good choice for all of the other points mentioned. Without going through

[8] This term is used for all the additional information linked to a scan like its dimensions and the conditions under which it was taken

all the pros and cons, I will now give a short summary of the concepts implemented in this application.

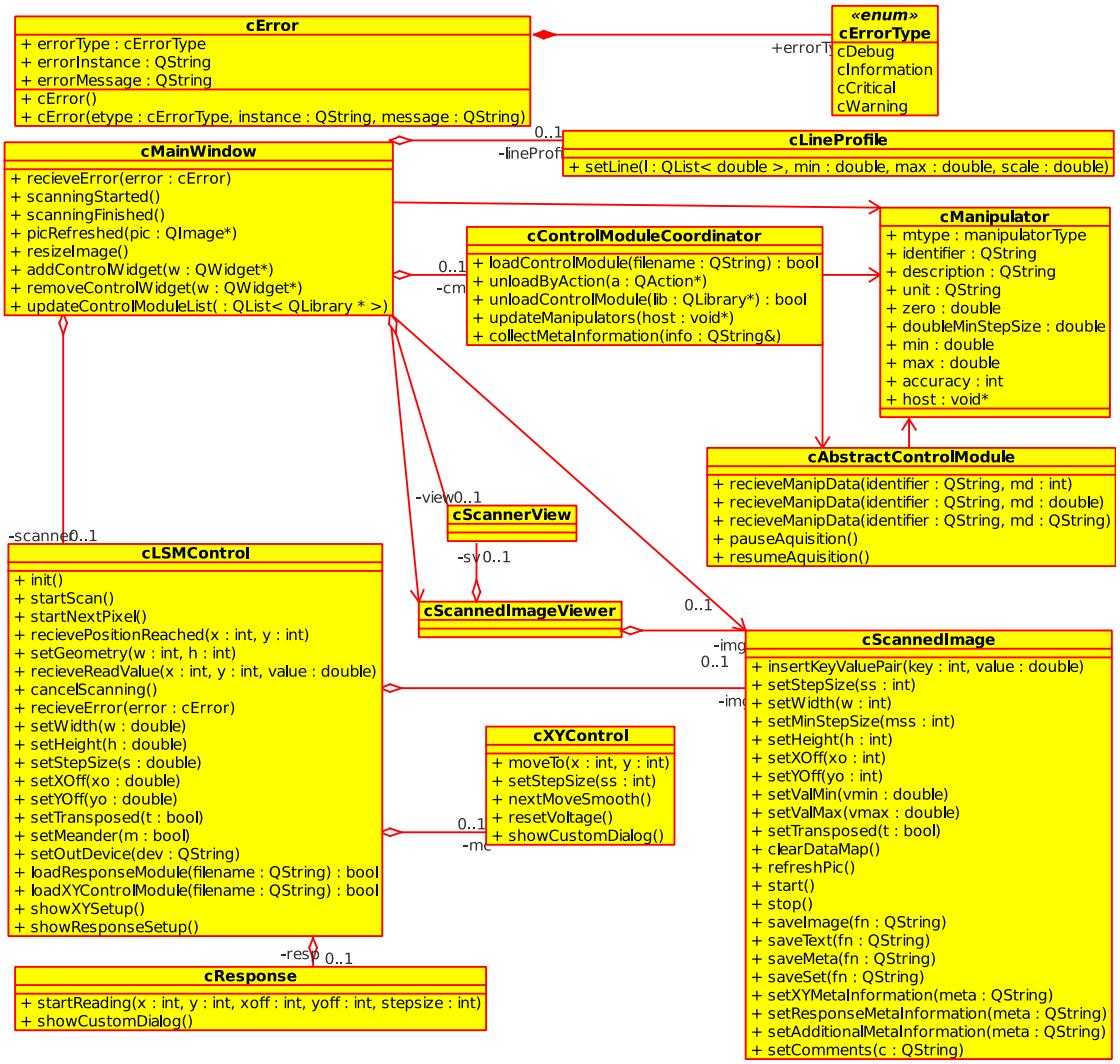

Figure A.6.: UML class diagram of the "Mr. Scanner" software.

Object Oriented Programming (OOP). This is a programming paradigm using so-called "objects" as the main elements of the program. Compared to procedural programming which is typically used in most older programming languages and script languages, it has some fundamental advantages especially in larger projects. The idea alone helps to structure large projects into smaller, much more manageable units. This helps the programmer to concentrate on single units inside the project and makes the structure more understandable for people not familiar with

this specific project. Class diagrams, like the one shown in Fig. A.6, provide an intuitive and quick way to understand the structure of the application without having to go through the actual code. OOP also offers features like inheritance or polymorphism, which, when used correctly, save a lot of time and avoid potential error sources.

Multithreading. This means that the programmer splits different segments of the application into threads which run parallel inside the main process. For modern multi-core computers this has the obvious advantage that these threads can run simultaneously on the different cores of the CPU. In conjunction with asynchronous communication between the threads this technique also helps to solve one of main problems of software communicating with hardware. When connecting to hardware wait times usually occur or the hardware does not respond at all. If the application does not use multithreading, it has to wait until the hardware responds or a timeout occurs. In extreme cases[9] this can lead to a freezing or even crashing application which can even cause a loss of measurement data. Putting all hardware-related processes into separate threads allows the user to operate the application normally even if one of the threads freezes or crashes and makes a complete crash of the application highly unlikely.

Modularity. Since this software was created to work with a variety of different hardware components, including all of the hardware related code into the application core would not have been a very practical solution. Instead we chose to source this code out into separate modules. In total there are three different kinds of modules:

- XY-control modules (inherited from cXYcontrol) control the position of the probe.
- Response modules (inherited from cResponse) read the response from the corresponding device.
- Extension modules (inherited from cAbstractControlModule) provide additional information and controls. They can also create cManipulator objects, which allow the user to make a series of scans.

Another positive aspect arising from this situation is that for new hardware the core of the application remains unchanged and does not have to be recompiled. It is only necessary to create a new module from a module template which is in itself a very simple task and does not require high programming skills.

A.2.3. Implementation

The creation of the application took about three weeks and the outcome meets all the requirements detailed in the first subsection. A screenshot of the GUI is shown in Fig. A.7. The GUI components seen in this figure can all be detached and moved around the screen freely to fit the personal taste of the user and the screen dimensions. The

[9] i.e. when the hardware stops responding during a transaction.

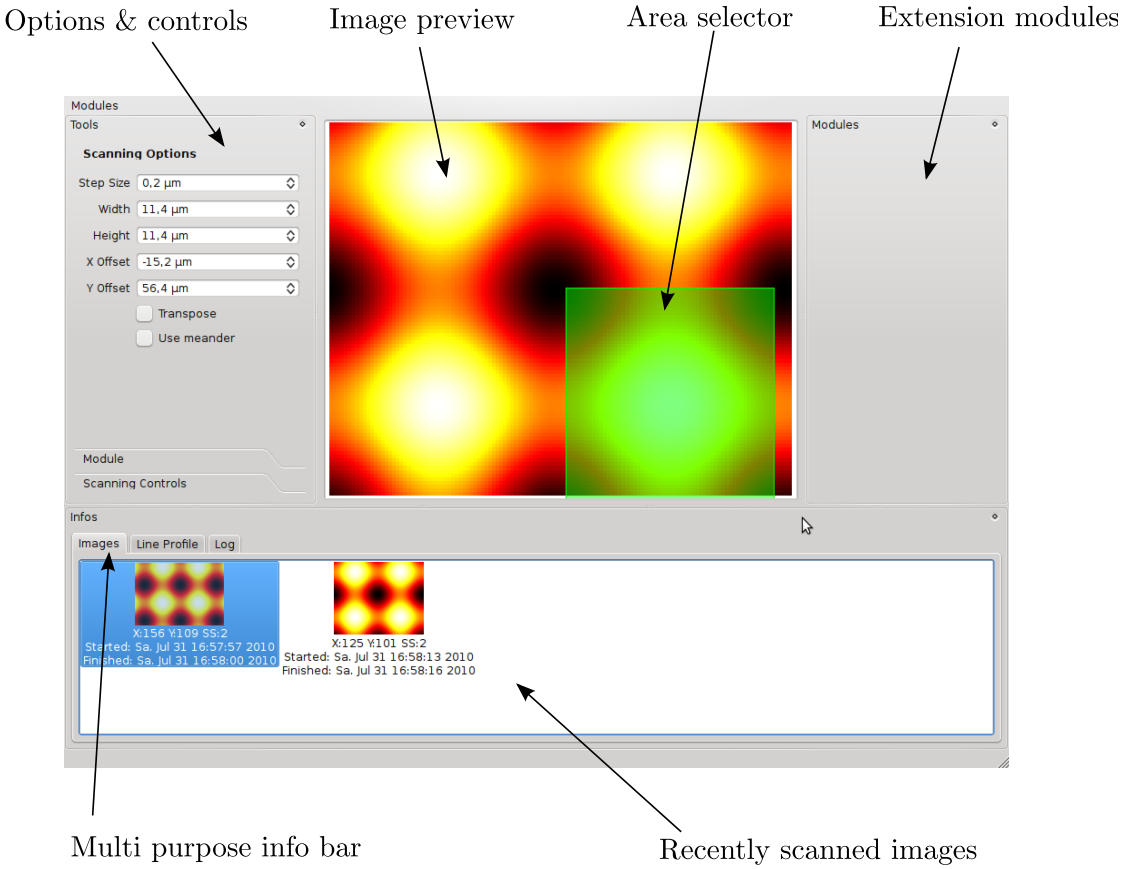

Figure A.7.: Graphical user interface of the “Mr. Scanner” Software.

application runs under various operating systems (Windows, Linux, Mac OS) and only the hardware-related modules have to be developed separately for each OS[10]. Modules can be loaded and unloaded during runtime, which makes it possible to use different kinds of hardware without restarting the application. Extension modules can be loaded to add scan-related meta information and control additional parameters manually or by automatic series of scans. The program supports a live preview of the current scan as well as a line-profile viewer and a library of recent scans. From this library the user can take a look at old scans, enlarge them and see the meta information which gets saved with each scan automatically. He can also save single scans or all scans from this library in different formats.

In summary we can say that we have created a working, full-featured scanning application that has been successfully tested and used in real experiments since most of the scans presented in this thesis were taken using this software.

[10]This is due to the fact that the hardware manufacturers usually only supply closed-source libraries for their devices.

Summary

In this thesis, I presented the work carried out during the one year as a diploma student. Throughout this time the main goal of my work was the spatial investigation of *Superconducting Nanowire Single Photon Detectors (SNSPD)*. The people I have worked with and myself were able to modify the existing laser scanning microscope to spatially map single photon detection events to the location of incoming photons. For this purpose, a special software and some improved hardware were designed and created. Most worthy of mentioning among these are a high frequency readout and a dedicated pulse counter.

Using this setup we were able to map the spatial detection efficiency of a meander-shaped SNSDP. This study proved that the detection efficiency of the detector was not limited by inhomogeneities of the sample. The active area we were able to extract from this data proved to be, within the accuracy of the measurement, what was expected from a priori considerations. As it was expected from the limited spatial resolution of this technique, we were not able to resolve any features of the meander itself.

To be able to spatially relate the detection efficiency to local critical currents, we devised a new sample layout. On the long bridge structures that were produced for this purpose, we are planning to conduct conventional resistive LSM measurements and photon count mapping experiments to find out more about the intrinsic inhomogeneities in the response.

Apart from the main line of experiments we were also able to extend the scope of this work by showing that results, qualitatively similar to the ones measured on the meander detector, can also be obtained from samples with a totally different geometry. For this purpose we used our setup to measure a single short constriction of an NbN film. These measurements show that even such structures work as single photon detectors.

Finally, we obtained data on the meander-shaped detector in a temperature range down to 200 mK, for which no published data exists so far. This experiment was conducted at the Technion University in Haifa, Israel. The data acquired this way suggests that there is an unexpectedly sharp decrease of dark count rates below a temperature of about $2.1K$. At this point, however, there is no hard evidence to decide whether this is in fact a property of the sample or some external influence, as e.g. he superfluid transition of helium in the sample environment.

With the modification of our setup and the results obtained during these studies we believe that the topic of this thesis still holds a lot of questions in store. We are confident that from the technological as well as from the physical side, this research still shows a lot of promise.

Zusammenfassung

Dies ist die Zusammenfassung der Ergebnisse meiner Diplomarbeit mit dem Titel *"Räumlich Aufgelöste Untersuchung Supraleitender NbN Einzelphotonendetektoren"* und den damit verbundenen Tätigkeiten.

Wie der Titel schon andeutet, befasst sich die vorliegende Arbeit vornehmlich mit einer verhältnismäßig jungen Klasse nanoelektronischer Geräte, sogenannten *"Supraleitenden Nanodraht Einzelphotonendetektoren"*. Die hierbei gebräuchliche Abkürzung SNSPD leitet sich aus dem englischen Namen *"Superconducting Nanowire Single Photon Detectors"* ab. Bei diesen Detektoren handelt es sich um aus Dünnfilmen hergestellte Drähte aus einem supraleitenden Material. Obwohl sie prinzipiell aus verschiedenen Supraleitern hergestellt werden können und werden, beschränken sich die Versuche dieser Arbeit auf Niob-Nitrid (NbN) Drähte auf Saphir (Al_2O_3) Substrat. Die Schichtdicken der erwähnten Dünnfilme sind im Normalfall wenige Nanometer und die Breite der Drähte in etwa $100nm$. Um eine möglichst große Fläche abzudecken, werden die Detektoren häufig nicht als einfache Linien, sondern als quadratische Mäander gefertigt, deren Ausmaße dann auch die Länge des Drahtes bestimmen.

Im Gegensatz zu den bereits existierenden Einzelphotonendetektoren, wie etwa Photomultiplier Röhren oder Avalanche Dioden, bieten SNSPs eine sehr hohe maximale Zählrate und können Photonen über einen sehr großen Wellenlängenbereich detektieren. Diese Eigenschaften machen die Weiterentwicklung trotz des verhältnismäßg hohen Betriebsaufwands interssant. Einer ihrer Hauptnachteile besteht in der realtiv geringen Detektionseffizienz von wenigen Prozent. Dies versucht man allerdings heutzutage durch das Aufbringen zusätzlicher, optischer Resonatoren auf den Detektoren in den Griff zu bekommen. Erste Ergebnisse auf diesem Gebiet zeigen, dass mit dieser Technik deutlich höhere Detektionseffizienzen erreicht werden können.

Zum Erreichen ihres Betriebszustandes werden diese Bauteile unter ihre supraleitende kritische Temperatur T_c abgekühlt um dann mittels eines Arbeitsstroms I_b [11] auf ihren Arbeitspunkt unterhalb ihres kritischen Stroms I_c [12] eingestellt zu werden. Typische Werte hierfür sind in etwa $I_b \approx 0.95 \cdot I_c$. In diesem Zustand, in dem der Arbeitsstrom vollständig durch die Cooper-Paare getragen wird und somit verlustfrei ist, kann ein auf den Detektor auftreffendes Photon eine Kettenreaktion in Gang setzten, die sich schlussendlich in einer lokalen Verringerung der Anzahl der Cooper-Paare niederschlägt. Werden kurzzeitig so viele Cooper-Paare getrennt, dass deren Anzahl lokal nicht mehr ausreicht, um den Arbeitsstrom in einem Querschnitt des Drahtes verlustfrei zu transportieren, so kann eine Sektion des Drahtes nicht mehr supraleitend bleiben. Durch die nun entstehenden Ohmschen Verluste und die äußere elektrische Beschaltung des Detektors wird ein elektrothermischer Prozess in Gang gesetzt, welcher nach außen als ein kurzer Spannungspuls sichtbar wird. Die Länge und Form der Pulse bestimmen sich dabei in erster Linie aus der kinetischen Induktivität L_K des Drahtes und seiner äußeren Beschaltung und sind in entscheidendem Maße für die Leistungsdaten, insbesondere die

[11] Aus dem Englischen *"bias current"*
[12] Aus dem Englischen *"ciritcal current"*

maximale Zählrate, des Detektors verantwortlich. Außer durch Photonen können diese Pulse auch durch andere, meist thermisch aktivierte, Ereignisse ausgelöst werden. Die konkreten Ursachen der dadurch auftretenden Dunkelzählraten [13] sind jedoch noch nicht vollständig verstanden und immer noch Thema vieler wissenschaftlicher Arbeiten. Die Pulse werden dann von den Gleichstromanteilen getrennt, verstärkt und können mittels eines Pulszählers gezählt werden.

Die überwiegende Mehrheit der Untersuchungen, die bislang an diesen Detektoren durchgeführt worden sind, haben sich mit deren Eigenschaften als ganzes Bauteil beschäftigt. Zwar wurden Versionen verschiedener Geometrien und Materialien charakterisiert, insbesondere in Hinblick auf ihre Detektionswahrscheinlichkeiten und Dunkelzählraten, jedoch zumeist ohne den Absorptionsort des auslösenden Photons dabei zu berücksichtigen. So konnten diese Untersuchungen zum Beispiel nie zeigen, ob der als aktiv[14] angenommene Teil der Detektorfläche dem tatsächlich aktiven Teil entspricht. Um diese und andere Fragen zu klären, entschlossen wir uns, das bei uns etablierte Laser-Raster-Mikroskop[15] zur räumlich ausgelösten Untersuchung dieser Bauteile zu verwenden. Dieses Instrument erlaubt es uns, mit einem fokussierten Laserstrahl die Oberfläche einer Probe abzurastern und zu jedem Punkt des Rasters einen Messwert aufzunehmen. Die Probe selbst, in unserem Fall einer der genannten Detektoren, kann sich dabei in einem Kryostat befinden.

Bei der Untersuchung der SNSPDs gibt es jedoch zwei wesentliche Unterschiede zu den meisten bisherigen Untersuchungen. Zum einen gibt es neben den klassischen LSM-Messungen[16] hier die Anforderung auch Zählraten als Eingangssignal zu verwenden. Dies umzusetzen erforderte die Entwicklung einer neuen Software, die auch Teil dieser Arbeit war. Zum zweiten ist aufgrund der kleinen Ausmaße[17] der untersuchten Detektoren und der in diesem Fall nicht vernachlässigbaren Größe des Brennflecks die Art der Signalentstehung zum Verständnis der Ergebnisse unumgänglich. Neben der quantisierten Natur der Messung werden die Ergebnisse auch durch die Faltung der Intensitätsverteilung des Brennflecks mit der tatsächlichen, räumlichen Detektionswahrscheinlichkeit verschleiert.

Der erste Teil der Umsetzung dieser Aufgabe befasste sich mit dem experimentellen Aufbau des Versuchs. Hier ist neben Detailveränderungen der optischen, elektrischen und kryogenischen Komponenten insbesondere die Entwicklung eines auf das Experiment angepassten Hochfrequenzauslesesystems und der schon erwähnten Software zu nennen. Des weiteren ergaben sich im Laufe des Experiments verschärfte Anforderungen an den von uns verwendeten Pulszähler, welche die Entwicklung eines eigens angepassten Geräts notwendig machten. Entwurf und Bau dieses neuen Pulszählers waren ebenfalls ein substantieller Bestandteil der vorliegenden Arbeit.

Im zweiten Schritt dieser Arbeit demonstrierten wir die Funktionalität des Aufbaus durch die Untersuchung von mäanderförmigen SNSPDs. Die Ergebnisse dieser Messreihe zeigen deutlich, dass der von uns untersuchte Detektor in der erwarteten Weise arbeitet.

[13] Aus dem Englischen *"dark counts"*

[14] Aktive Fläche des Detektors ist der Anteil der Gesamtfläche, der zur Detektion beiträgt.

[15] Oft auch nur LSM, aus dem Englischen *"Laser Scanning Microscope"*

[16] Bei denen ein analoges Signal proportional zur lokalen kiritschen Stromdichte aufgenommen wird.

[17] Die hier verwendeten: $4 \times 4\mu m^2$

Trotz der begrenzten räumlichen Auflösung unseres Messaufbaus konnten wir zeigen, dass die gemessene aktive Fläche - im Rahmen der Messgenauigkeit - der entspricht, die man a priori angenommen hatte.

Da diese Ergebnisse zwar aus Anwendungssicht positiv zu beurteilen waren, jedoch aufgrund der geringen Strukturgröße der Mäanderlinien nicht viele Rückschlüsse auf die Physik der Detektion zuließen, beschlossen wir hierfür einen speziell zugeschnittenen Detektor zu entwerfen, der geometrisch im Wesentlichen einer "aufgefalteten" Version des bereits untersuchten Mäanders entspricht. Indem wir Ergebnisse der traditionellen LSM Messungen und der neuen Einzelphotonenmessungen kombinieren, erhoffen wir uns mit diesen Proben in Zukunft weitere Erkenntnisse über die internen Mechanismen der Photonendetektion zu gewinnen.

Neben diesem Hauptstrang der Arbeit ergaben sich im Laufe der Versuche noch zwei weitere Möglichkeiten die gewonnen Erkenntnisse zu vertiefen: Im ersten Versuch konnten wir nachweisen, dass auch geometrisch auf den ersten Blick völlig ungeeignete Strukturen als Photonendetektoren arbeiten können. Zu diesem Zwecke schlossen wir eine eigentlich für eine andere Messung bestimmte kurze NbN Brücke an den Messaufbau an und konnten so die Arbeitsstromabhängigkeit der Dunkelzählraten und Zählraten bei Beleuchtung messen. Die hier auftretende kurze Pulsbreite war einer der Gründe für den Bau eines schnelleren Pulszählers, der unter Anderem auch einer weiteren Charakterisierung eben dieser Proben dienen wird.

In einem zweiten Nebenexperiment an der Technion Universität in Haifa, Israel wollten wir ursprünglich die von uns gewonnenen Erkenntnisse anhand eines anderen Versuchsaufbaus verifizieren. Technische Gegebenheiten bewogen uns jedoch dazu den Fokus der Arbeit auf das Verhalten der Detektoren bei tiefen Temperaturen zu legen, da uns zum damaligen Zeitpunkt keine Messdaten für Temperaturen kleiner 2K vorlagen. Die nun vorliegenden ersten Ergebnisse dieses Versuchs zeigen einen leichten Anstieg der Detektionseffizienz um etwa 25% bei 100mK gegenüber 2.3K. Des Weiteren haben wir einen qualitativen Unterschied im Verhalten der Detektoren nahe ihrem kritischen Strom festgestellt. Während bei Temperaturen über ca. 2.1K die Dunkelzählraten auf über 10^3 nahe I_c ansteigen, sind sie knapp unterhalb dieser Temperatur um durschnittlich fast zwei Größenordnungen kleiner. Dieses Verhalten widerspricht Ergebnissen bisheriger Messungen zwischen 1.5 und 2K und lässt sich auch nicht ohne Weiteres aus den in dieser Arbeit zitierten Modellen erklären. Mögliche Ursachen könnten etwa die thermische Kopplung zwischen der NbN Schicht und dem Saphir Substrat oder aber suprafluide Helium-Ablagerungen an der Oberfläche des Detektors sein. Weitere Messungen in diesem Temperaturbereich müssen hier noch Klarheit schaffen.

Zusammenfassend lässt sich sagen, dass wir einen Versuchsaufbau zur räumlich aufgelösten Untersuchung von Einzelphotonendetektoren geschaffen haben. Die damit gewonnenen Erkenntnisse an mäanderförmigen Detektoren zeigen, dass diese in der erhofften Art und Weise funktionieren. Zukünftige Messungen an speziell entwickelten Proben können in diesem Aufbau vertiefte Kenntnisse über die Prozesse der Detektion liefern. Weiterhin haben wir mit Experimenten an geometrisch ungewöhnlichen Detektoren und bei tiefen Temperaturen gezeigt, dass es anwendungsbezogen wie physikalisch noch viele offene Fragen in diesem Gebiet gibt, die weitere Forschung rechtfertigen.

Acknowledgements

First of all I would like to thank Prof. Alexey V. Ustinov for giving me the chance to work on such an exciting topic and in the environment of so many interesting and motivated scientists from all over the world. He has shown great confidence in my work and abilities, offered his guidance wherever he could while leaving me the freedom to pursue my way, even when it was not always the straightest one. He also gave me the opportunity to work abroad which I highly appreciate not only as a scientific chance, but also as an experience for life.

Secondly I would like to thank all of the "Fluxons" who have all helped me in one or the other way by answering many of my questions, taking part in discussions or simply by making my work day a little brighter. Among these people I owe especially great thanks to Dr. Sasha Lukashenko who introduced me to the field of laser scanning microscopy and helped me innumerable times along my way. His calm hands and his proficiency in mending pretty much everything make him an invaluable part of this group. Many thanks also to Roland Jehle, who worked with me on the pulse counter, for his commitment, motivation, and all the effort he has put into the project. Without his technical skills it would simply not have been possible.

From the *Institut für Mikro- und Nanoelektronische Systeme* I would like to thank Prof. Michael Siegel for the opportunity to work on their top-of-the-field samples and for taking the duty of being co-referent. I would also like to extend special thanks to Dr. Konstantin Ilin to whom I owe my first contact with nano-electronics during an internship which kindled my interest in this field. Among all the other people from the IMS, Dipl.-Ing. Matthias Hofherr and Dr. Stephan Wünsch deserve my gratitude for answering so many of my questions and assisting me in the preparations of my experiment.

Three of our guests from the *Institute of Low Temperature Physics* in Kharkov, Ukraine deserve my highest thanks: Dr. Alexander Zhuravel for his relentless endeavors to repair and improve the LSM and his continued support of my work as well as Dr. Alexander Sivakhov and Dr. Alexander Glukhov for their help.

From the *Nano-Electronics Research Center* at *Technion University, Haifa, Israel* I would like to express my gratitude to Prof. Eyal Buks. He has given me a great opportunity by inviting me to his institute and giving me the chance to work with him and his team. Of those people I especially want to thank Gil Bachar for all the time and effort he spent during my stay but also for the great hospitality and amity he has shown me.

I would also like to thank B.Sc. Daniel Hepp for assisting me in creating the scanning microscopy application and my mother for proofreading this thesis.

Last but not least I want to thank my family, friends and my girlfriend. Their love and support cannot be described by words. Thank you for everything that you are.

Bibliography

[1] D. Abraimov. *Scanning laser microscopy of superconducting structures.* PhD thesis, Friedrich-Alexander-Universität Erlangen-Nürnberg, 2001.

[2] D. Abraimov, DM Feldmann, AA Polyanskii, A.V. Gurevich, G. Daniels, DC Larbalestier, A.P. Zhuravel, and A.V. Ustinov. Scanning laser imaging of dissipation in YBaCuO-coated conductors. *Applied Physics Letters*, 85:2568, 2004.

[3] H. Bartolf, A. Engel, A. Schilling, K. Il'in, M. Siegel, H.W. Hübers, and A.D. Semenov. Current-assisted thermally activated flux liberation in ultrathin nanopatterned nbn superconducting meander structures. *Phys. Rev. B*, 81(2):024502, Jan 2010. doi: 10.1103/PhysRevB.81.024502.

[4] W. Emkey and C. Jack. Analysis and evaluation of graded-index fiber lenses. *Lightwave Technology, Journal of*, 5(9):1156–1164, 1987.

[5] A. Engel, A.D. Semenov, H.W. Hübers, et al. Fluctuations and dark count rates in superconducting NbN single-photon detectors. *physica status solidi (c)*, 2(5): 1668–1673, 2005.

[6] Allen M. [Hrsg.] Goldman. *Percolation, localization and superconductivity : [proc. of a NATO Advanced Study Inst. on Percolation, Localization, and Superconductivity, held June 19 - July 1, 1983, at Les Arcs, Savoie, France].* NATO ASI series : Series B, Physics ; 109. Plenum Press, New York [u.a.], 1984. ISBN 0-306-41713-8.

[7] R. Gross and D. Koelle. Low temperature scanning electron microscopy of superconducting thin films and Josephson junctions. *Reports on Progress in Physics*, 57: 651, 1994.

[8] A.V. Gurevich and RG Mints. Self-heating in normal metals and superconductors. *Reviews of Modern Physics*, 59(4):941–999, 1987.

[9] R.H. Hadfield, P.A. Dalgarno, J.A. O'Connor, E. Ramsay, R.J. Warburton, E.J. Gansen, B. Baek, M.J. Stevens, R.P. Mirin, and S.W. Nam. Submicrometer photoresponse mapping of nanowire superconducting single-photon detectors. *Applied Physics Letters*, 91:241108, 2007.

[10] M. Hofherr, D. Rall, K. Il'in, M. Siegel, A.D. Semenov, H.W. Hubers, and N.A. Gippius. Intrinsic detection efficiency of superconducting nanowire single-photon detectors with different thicknesses. *Journal of Applied Physics*, 108:014507, 2010.

[11] A.J. Kerman, E.A. Dauler, W.E. Keicher, J.K.W. Yang, K.K. Berggren, G. Gol'tsman, and B. Voronov. Kinetic-inductance-limited reset time of superconducting nanowire photon counters. *Applied Physics Letters*, 88:111116, 2006.

[12] J. Kitaygorsky, I. Komissarov, A. Jukna, D. Pan, O. Minaeva, N. Kaurova, A. Divochiy, A. Korneev, M. Tarkhov, B. Voronov, et al. Dark counts in nanostructured NbN superconducting single-photon detectors and bridges. *IEEE Transactions on Applied Superconductivity*, 17(2 Part 1):275–278, 2007.

[13] S. Kobayasi, M. Shinohara, et al. Thermometry using W carbon resistors in a temperature region around 10 mK. *Cryogenics*, 16(10):597–600, 1976.

[14] K. K. Likharev. Superconducting weak links. *Rev. Mod. Phys.*, 51(1):101–159, Jan 1979. doi: 10.1103/RevModPhys.51.101.

[15] Y. Liu, Y. Liang, G. Mu, and X. Zhu. Deconvolution methods for image deblurring in optical coherence tomography. *Journal of the Optical Society of America A*, 26 (1):72–77, 2009.

[16] L. Maingault, P. Cavalier, and J.-C. Villegier. Investigation of quantum efficiency and polarization effects in nbn superconducting single photon detectors. In *EC Sinphonia NMP4-CT-2005-16433*, 2008.

[17] Dieter Meschede. *Optik, Licht und Laser*. Vieweg+Teubner Verlag / GWV Fachverlage GmbH, Wiesbaden, Wiesbaden, 3., durchgesehene auflage edition, 2008. ISBN 978-3-8348-9288-1. URL `http://dx.doi.org/10.1007/978-3-8348-9288-1`. In: Springer-Online.

[18] S. Miki, M. Takeda, M. Fujiwara, M. Sasaki, and Z. Wang. Compactly packaged superconducting nanowire single-photon detector with an optical cavity for multichannel system. *Opt. Express*, 17:23557–23564, 2009.

[19] Newport. Gaussian beam optics tutorial. URL `http://www.newport.com/servicesupport/Tutorials/default.aspx?id=112`.

[20] J.A. O'Connor, P.A. Dalgarno, M.G. Tanner, R.J. Warburton, R.H. Hadfield, B. Baek, S.W. Nam, S. Miki, Z. Wang, and M. Sasaki. Nano-Optical Studies of Superconducting Nanowire Single Photon Detectors. In *Quantum Communication and Quantum Networking: First International Conference, QuantumComm 2009, Naples, Italy, October 26-30, 2009, Revised Selected Papers*, page 158. Springer, 2010.

[21] M. S. Pambianchi, S. M. Anlage, E. S. Hellman, E. H. Jr. Hartford, M. Bruns, and S. Y. Lee. Penetration depth, microwave surface resistance, and gap ratio in nbn and ba[sub 1 - x]k[sub x]bio[sub 3] thin films. *Applied Physics Letters*, 64(2):244–246, 1994. doi: 10.1063/1.111517. URL `http://link.aip.org/link/?APL/64/244/1`.

[22] A.D. Semenov, G. Gol'tsman, and A. Korneev. Quantum detection by current carrying superconducting film. *Physica C: Superconductivity*, 351(4): 349–356, 2001. ISSN 0921-4534. doi: DOI:10.1016/S0921-4534(00)01637-3. URL `http://www.sciencedirect.com/science/article/B6TVJ-42RDSRJ-4/2/8ca91105f9aa8b93fc35c82654e94ff0`.

[23] A.D. Semenov, A. Engel, H.W. Hübers, K. Il'in, and M. Siegel. Spectral cut-off in the efficiency of the resistive state formation caused by absorption of a single-photon in current-carrying superconducting nano-strips. *The European Physical Journal B-Condensed Matter and Complex Systems*, 47(4):495–501, 2005.

[24] A.D. Semenov, P. Haas, B. Günther, H.W. Hübers, K. Il'in, M. Siegel, A. Kirste, J. Beyer, D. Drung, T. Schurig, and A. Smirnov. An energy-resolving superconducting nanowire photon counter. *Superconductor Science and Technology*, 20(10): 919, 2007. URL `http://stacks.iop.org/0953-2048/20/i=10/a=005`.

[25] A.D. Semenov, P. Haas, B. Günther, H.W. Hübers, K. Il'in, and M. Siegel. Energy Resolution of a Superconducting Nanowire Single-Photon Detector. *Journal of Low Temperature Physics*, 151:564–569, April 2008. doi: 10.1007/s10909-007-9693-2.

[26] A.D. Semenov, P. Haas, H.W. Hübers, K. Il'in, M. Siegel, A. Kirste, T. Schurig, and A. Engel. Vortex-based single-photon response in nanostructured superconducting detectors. *Physica C: Superconductivity*, 468(7-10):627–630, 2008.

[27] A.D. Semenov, P. Haas, H.W. Hübers, K. Il'in, M. Siegel, A. Kirste, T. Schurig, and R. Herrmann. Improved energy resolution of a superconducting single-photon detector. In *Proceedings of SPIE*, volume 7021, page 70211E, 2008.

[28] A.D. Semenov, P. Haas, H.W. Hübers, K. Il'in, M. Siegel, A. Kirste, D. Drung, T. Schurig, and A. Engel. Intrinsic quantum efficiency and electro-thermal model of a superconducting nanowire single-photon detector. *Journal of Modern Optics*, 56(2):345–351, 2009.

[29] Colin J. ; Shotton David Sheppard. *Confocal laser scanning microscopy.* Microscopy handbooks ; 38. BIOS Scientific, London, 1997. ISBN 1-872748-72-4.

[30] Michael Tinkham. *Introduction to superconductivity.* Dover books on physics. Dover Publ., Mineola, NY, 2. ed. edition, 2004. ISBN 0-486-43503-2. This Dover ed., first publ. in 2004, is an unabridged republication of the 1996 2. ed. ... by McGraw-Hill Book, New York.

[31] A.P. Zhuravel, S.M. Anlage, and A.V. Ustinov. Measurement of local reactive and resistive photoresponse of a superconducting microwave device. *Applied Physics Letters*, 88:212503, 2006.

[32] A.P. Zhuravel, AG Sivakov, O.G. Turutanov, AN Omelyanchouk, S.M. Anlage, A. Lukashenko, A.V. Ustinov, and D. Abraimov. Laser scanning microscopy of HTS films and devices (Review Article). *Low Temperature Physics*, 32:592, 2006.

Erklärung:

Hiermit versichere ich, dass ich die vorliegende Arbeit selbständig angefertigt habe und keine anderen als die angegebenen Quellen und Hilfsmittel benutzt habe.

Karlsruhe, den